UTILIZATION OF NEUTRONS IN NUCLEAR DATA MEASUREMENTS AND BULK SAMPLE ANALYSIS

By

Sunday Adesunloye Jonah

A thesis submitted to the Postgraduate School of Ahmadu Bello University, Zaria, Nigeria in partial fulfillment of the requirements for the award of the degree of Doctor of Philosophy in Physics.

Department of Physics,
Faculty of Science,
Ahmadu Bello University,
Zaria, Nigeria.

March, 1995.

DECLARATION

I hereby declare that:

1) the report presented in this thesis is the result of my original research
2) this thesis has not been submitted to any other institution, organization or body for any award other than the Ahmadu Bello University; and
3) all inclusions from works other than this have been duly acknowledged.



..... 07-07-95

Sunday Adesunloye Jonah Date

CERTIFICATION

This thesis entitled "UTILIZATION OF NEUTRONS IN NUCLEAR DATA MEASUREMENTS AND BULK SAMPLE ANALYSIS" by Sunday Adesunloye Jonah meets the regulations governing the award of the degree of Doctor of Philosophy of Physics of Ahmadu Bello University, Zaria, Nigeria and is approved for its contribution to knowledge and literary presentation.

.....
Professor S.B. Elegba
(Chairman, Supervisory Committee)

10-07-95
.....
Date

.....
Dr. N. Hariharan
(Member, Supervisory Committee)

13-07-95
.....
Date

.....
Professor S.B. Ojo
Head, Department of Physics.

04/03/96
.....
Date

.....
Dean, Postgraduate School.

26/8/96
.....
Date

ACKNOWLEDGEMENT

The work hereby described was carried out at the Institute of Experimental Physics, Kossuth Lajos University, Debrecen, Hungary under a bilateral agreement with the Centre for Energy Research and Training, Ahmadu Bello University, Zaria. The financial support was provided by fellowship awards from the International Atomic Energy Agency, Vienna, Austria and the National Universities Commission/World Bank assisted development project for staff of Nigerian Universities. To these bodies, I remain ever grateful.

I am greatly indebted to my supervisors, Professors S.B. Elegba and J. Adetunji for the positive criticisms and their resourcefulness in the development of the project. I am deeply touched by the welfare and support provided by Professor J. Csikai an IAEA expert who supervised the work in Debrecen. He arranged for all the facilities cost-free and supplied me with the most recent information throughout the work and indeed since my career in Nuclear Physics. To me, Professor J. Csikai is not only a teacher but also an academic mentor. Additionally, my sincere appreciations are due to Dr. (Mrs.) Cs Buczko and staff members of the Institute of Experimental Physics as well as my friends in Debrecen. To all of you, I say "*koszonjuk*" for all the assistance rendered.

Let me also express my gratitude to the head of Physics department, Professor S.B. Ojo and the deparmental coordinator of postgraduate programmes, Dr. I.B. Osazuwa for their immense contributions throughout the duration of the work. I am equally grateful to Dr. N. Hariharan and Dr. B.W. Jimba whose positive criticisms as internal examiners have greatly enhanced the quality of this work. I wish to express my deep gratitude to my family and friends especially Ms. O. Anazia for their encouragement during the trips abroad to carry out the work. I hereby acknowledge the assistance of others whose names have not been mentioned due to space constraint.

Finally and most importantly, I thank the Almighty God for providing me with good health, wisdom and the perseverance that saw me to the successful completion of the work.

ABSTRACT

Experimental investigations were carried out with neutrons in the fields of neutron data measurements and bulk sample analysis based on the interactions of neutrons. The principles and techniques of neutron interactions required in the investigations together with some salient features of the sources employed are enumerated. Excitation cross section curves and isomeric cross section ratio of Ni(n,p) Co reaction over the neutron energy range of between 5 and 15 MeV were determined using the activation analysis technique in combination with high-resolution gamma spectroscopy. Characteristics of the incident neutrons produced via the D-T reaction of a neutron generator and D-D reaction of a cyclotron were determined experimentally to account for the contributing effects of background neutrons especially in the 5-13 MeV neutron energy range where existing data are scanty and rather discrepant. The measured data agree well with calculated data using nuclear models but deviate significantly from the recommended data based on existing literature data. The measured ° $_{act}$ and $_{\circ}^{m}$ $_{\circ}^{g}$ data made it possible to determine the cross section curve for Ni(n,p.)^{58} Co^{m} reaction. Furthermore the flux density distributions of thermal and primary fast neutrons in different configurations of bulk samples consisting of water, graphite and coal together with the attenuation characteristics were determined by the activation analysis and pulse height response spectrometry

techniques. From the results obtained, an experimental geometry has been proposed for on-line elemental analysis of coal and other minerals. Similarly the total hydrogen content and O+C/H atomic ratio in household and motor oils as well as crude oil samples of different origins were measured by an improved experimental arrangement based on the thermal neutron reflection technique. A detection limit of 0.12 w %. was obtained for hydrogen indicating the possible adaptation of this technique for quality control of petroleum products.

TABLE OF CONTENTS

Chapter		Page
	Title Page	i
	Declaration	ii
	Certification	iii
	Acknowledgement	iv
	Abstract	vi
	Table of Contents	viii
	List of Tables	xii
	List of Figures	xvi
	List of Appendices	xxii
	Abbreviations	xxiii
1.0	INTRODUCTION	1
1.1	General Introduction	1
1.2	Review of Previous Works	4
1.3	Present Work	7
1.4	Outline of Thesis	8
2.0	PRINCIPLES AND TECHNIQUES OF NEUTRON INTERACTION	10
2.1	Properties and Classifications of Neutrons	11
2.1.1	Basic properties of the neutron	11
2.1.2	Classifications of neutrons	11
2.2	Interactions of Neutrons with Matter	13
2.2.1	Interactions of neutrons with nuclei	13

2.2.2 Interactions of neutrons with bulk matter ..19
2.3 Neutron Sources 25
2.3.1 Radioisotope neutron sources 25
2.3.2 Fission neutron sources 29
2.3.3 Accelerator-based neutron sources 30
2.4 Experimental Techniques 37
2.4.1 The neutron activation analysis technique ..38
2.4.2 The thermal neutron reflection technique ...53
2.4.3 The pulse height response spectrometry technique 57

3.0 CHARACTERIZATION OF NEUTRON FIELDS 63
3.1 Energy Calibration of Low-voltage Accelerator by $^{11}B(p,\gamma)^{12}C$ reaction 64
3.1.1 Introduction 64
3.1.2 Experimental procedures 65
3.1.3 Results and discussion 66
3.2 Angular Energy Distribution of D-T Neutrons Produced by a Neutron Generator 68
3.2.1 Introduction 68
3.2.2 Experimental procedures 71
3.2.3 Results and discussion 74
3.3 Spectral Distribution of D-D Neutrons Produced by a Cyclotron 76
3.3.1 Introduction 76
3.3.2 Experimental procedures 77
3.3.3 Results and discussion 84

4.0 EXCITATION FUNCTIONS AND ISOMERIC CROSS SECTION RATIOS.....89

4.1 Introduction 89

4.2 Principles of Cross section Measurements ...90

4.3 Experimental Procedures 92

4.3.1 Irradiation 92

4.3.2 Activity measurements 93

4.4 Data Evaluation and Corrections 96

4.5 Results and Discussion 98

5.0 CHARACTERISTIC DATA OF NEUTRON INTERACTIONS USED IN THE ANALYSIS OF BULK SAMPLES 107

5.1 Introduction 107

5.2 Thermal and Fast Neutron Flux Distributions in Bulk Samples 109

5.2.1 Experimental procedures 109

5.2.2 Data measurements and evaluation 111

5.2.3 Results and discussion 117

5.3 Attenuation Characteristics of ^{252}Cf, Pu-Be and 14 MeV Neutrons Transversing Different Thicknesses of Bulk Samples 131

5.3.1 Experimental procedures 131

5.3.2 Results and discussion 133

6.0 TOTAL HYDROGEN CONTENT AND CARBON/HYDROGEN RATIO IN OIL SAMPLES BY THERMAL NEUTRON REFLECTION TECHNIQUE.....146

6.1 Introduction 146

6.2 Experimental Procedures 147

6.3 Results and Discussion 151

7.0 SUMMARY, CONCLUSION AND RECOMMENDATION 153

7.1 Summary and Conclusion 153

7.1.1 Excitation functions and cross section ratios of $^{58}Ni(n,p)^{58}Co^{m,g}$ reaction from 5 to 15 MeV 154

7.1.2 Characteristics data of neutron interaction 154

7.2 Recommendation 155

REFERENCES 156

APPENDIX 163

LIST OF TABLES

2.1	Some basic properties of the neutron	11
2.2	Characteristics of some Be(α,n) neutron sources	27
2.3	Neutron producing reactions used in accelerator-based neutron sources	33
3.1	Intensity of proton-induced gamma-ray yield as a function of terminal voltage	68
3.2	Values of the parameters in equation 3.1 for the calculation of angular dependence of neutron energy	71
3.3	Nuclear data of the energy and flux monitor reactions	73
3.4	Measured cross sections of $^{90}Zr(n,2n)^{89}Zr$ reaction at different angles of emission	75
3.5	Deduced and calculated mean energy of neutrons as a function of emission angle	75

3.6	Energy data of deuteron beam used for the production of neutrons at the cyclotron	79
3.7	Nuclear data of threshold energy monitor reactions	80
3.8	Measured specific activities of the threshold energy monitors	84
3.9	Ratios of reaction rates integrated over the group of breakup and monoenergetic neutrons to the total at the different incident neutron energies for $^{58}Ni(n,p)$ and $^{27}Al(n,\alpha)$ reactions	85
4.1	Nuclear data accepted for the determination of the cross section curves	94
4.2	A summary of measured total cross section, metastable state cross section and isomeric cross section data for $^{58}Ni(n,p)$ reaction	99
5.1	Nuclear data of the flux monitor reactions	111
5.2	Measured thermal neutron flux density at moderator-reflector interface using the setup shown in Figure 5.1a	112

5.3	Measured thermal neutron flux density in bare samples using the setup shown in Figure 5.1b	113
5.4	Measured thermal neutron flux density in samples sandwiched between 8 cm thick water moderator and reflector (setup geometry Figure 5.1b)	114
5.5	Measured thermal neutron flux density in coal sample with and without reflector (setup geometry Figure 5.1b)	114
5.6	Measured thermal neutron flux density at different positions in samples using the setup shown in Figure 5.1c	115
5.7	Measured fast neutron flux density at different positions in samples using the setup shown in Figure 5.1c	115
5.8	Specific activity induced in indium of different thickness	117
5.9	Deduced parameters for the characterization of neutron fields in bulk samples	124

5.10	Measured relative peak areas of 14 MeV neutrons traversing different samples and deduced macroscopic removal cross sections for the samples	138
5.11	Flux fraction of ^{252}Cf neutrons traversing different thicknesses of Polish coal	140
5.12	Flux fraction of Pu-Be neutrons traversing different thicknesses of Polish coal	141
5.13	Attenuation parameters $[\Sigma_R(E_{ti})$ values deduced from spectrum averaged flux densities for different $(n,n'\gamma)$ threshold reactions as a function of coal thickness for ^{252}Cf and Pu-Be neutrons	144
6.1	Measured data of standard samples used for the detemination of the calibration lines	149
6.2	The measured data and deduced H and O+C/H ratio for the oil samples	152

LIST OF FIGURES

2.1 A schematic diagram of neutron-nucleus interaction processes 15

2.2 Dynamics of neutron collisions in (a) laboratory system (b) centre of mass system and (c) the relationships between the velocities in both systems 21

2.3 Energy spectra of the Pu-Be neutron source used in this work 28

2.4 Energy spectra of the ^{252}Cf neutron source used in this work 31

2.5 Typical total yield of D-D and D-T neutrons versus deuteron energy 35

2.6 Geometrical setups of (a) the NaI(Tl) detector and (b) the Ge-Li detector systems used in this work 45

2.7 Photo peak efficiency curves of the Ge-Li detector as a function of sample-source distance 46

2.8	Photo peak and total efficiency curves of the NaI(Tl) detector	47
2.9	Diagram for the self-absorption of gamma-ray in a sample	52
2.10	An improved experimental setup for the determination of H and O+C/H in oil samples based on neutron reflection technique	56
2.11	A block diagram of the PHRS system	61
2.12	Rise-time-spectra of (a) neutron and gamma events and (b) after the elimination of gamma events	62
3.1	Schematic diagram of the experimental arrangement used for the energy calibration of low-voltage accelerator	67
3.2	Intensity of proton-induced gamma-ray versus terminal voltage	69
3.3	Scattering-free geometry for cross section measurements	73

3.4	Beam energy loss in the entrance window of a D_2 gas cell as a function of the incident beam energy	78
3.5	Scheme of the experimental arrangement at the cyclotron	81
3.6	Measured spectra of neutrons produced with deuteron beam of 3.87 and 9.39 MeV energies	83
3.7	A comparison of neutron spectra measured by PHRS and activation unfolding techniques	87
3.8	A comparison of spectra distributions of neutrons produced with fresh and used W beam stop in the gas cell	88
4.1	The decay scheme of ^{58}Co radionuclide	95
4.2	Typical intensity vs. cooling time decay-curve of $^{58}Co^{m,g}$ radionuclide	100
4.3	Measured, calculated and evaluated excitation functions of $^{58}Ni(n,p)^{58}Co^{m,g}$ reaction	102

4.4 A comparison of measured, calculated and evaluated excitation functions of $^{58}Ni(n,p)^{58}Co^{m,g}$ reaction 103

4.5 Isomeric cross section ratio of $^{58}Ni(n,p)^{58}Co^{m,g}$ reaction as a function of neutron energy 105

4.6 A comparison of measured, calculated and evaluated excitation functions of $^{58}Ni(n,p)^{58}Co^{m}$ reaction 106

5.1 Setup geometries used for the determination of fast and thermal neutron flux densities distributions in bulk samples 110

5.2 Variation of activity with thickness of indium foil exposed to the same flux of thermal neutrons 118

5.3 Dependence of absolute thermal neutron flux density at moderator-reflector interface versus moderator thickness 119

5.4 Flux density distributions of thermal neutrons in the bare samples 121

5.5 Flux density distributions of thermal neutrons in samples sandwiched between water moderator and reflector 122

5.6 Flux density distributions of thermal neutrons in coal samples with and without reflector 123

5.7 Flux density distributions of thermal neutrons in the samples at different positions in the presence of 8 cm thick water moderator 128

5.8 Flux density distributions of fast neutrons in the samples at different positions in the presence of 8 cm thick water moderator 129

5.9 The scheme of geometrical setup proposed for the on-line analysis of bulk samples 130

5.10 The setup geometry for investigating the attenuation characteristics of ^{252}Cf, Pu-Be and D-T neutrons in different samples 132

5.11 A semi-log plot of relative peak areas of transmitted neutrons versus thickness for different bulk samples 134

5.12 Transmission spectra of ^{252}Cf neutrons for Polish coal 135

5.13 Transmission spectra of Pu-Be neutrons for Polish coal 136

5.14 Transmission spectra of D-T neutrons for Polish coal 137

5.15 Spectrum averaged flux densities of ^{252}Cf neutrons as a function thickness for coal 142

5.16 Spectrum averaged flux densities of Pu-Be neutrons as a function thickness for coal 143

6.1 Calibration line used for the determination of total hydrogen content in oil samples 149

6.2 Calibration line used for the determination of O+C/H atomic ratio in oil samples 150

LIST OF APPENDICES

Appendix 163

ABBREVIATIONS

APM	Associated Particle Monitor
BI	Bipolar Output
BF_3	Boron Tri-fluoride gas filled counter
CINDA	The Index to Literature and Computer files on Microscopic Neutron Data
CM	Centre of Mass coordinate system
D-D	Deuteron-Deuterium reaction
D-T	Deuteron-Tritium reaction
EC	Electron Capture process
ENDF	Evaluated Nuclear Data Files
ENDL	Evaluated Nuclear Data Libraries
FRT	Fusion Reactor Technology
FWHM	Full Width at Half Maximum
Ge-Li	Lithium drifted Germanium semi conductor detector
IAEA	International Atomic Energy Agency
IRDF	International Reactor Dosimetry File
IT	Internal Transition process
LN_2	Liquid Nitrogen supply
MCA	Multichannel Analyzer
MGC-20	A variable-energy cyclotron facility
NaI(Tl)	Thallium activated Sodium Iodide scintillator detector

NE 213	Liquid scintillator from Nuclear Enterprises Inc.
PHRS	Pulse Height Response Spetrometry system
Pu-Be	Plutonium Beryllium neutron source
RF	Radio Frequency ion source
S/B	Signal-to-Background ratio
Si-Li	Lithium drifted Silicon semi conductor detector
TOF	Time-of-Flight spectrometer
UNI	UNiploar output
WRENDA	the World Request List for Nuclear Data

CHAPTER ONE

1.0 INTRODUCTION

1.1 General Introduction

The discovery of neutrons by Chadwick in 1932 has helped in solving many problems hitherto encountered in the study of atomic and nuclear structure (Marion and Fowler, 1960). Neutron is an uncharged particle and does not experience the Coulomb repulsion force. It has a wide energy range from the "cold" region (*i.e.*< 0.025 eV) to the "spallation" region (*i.e.*> 100 MeV) and does not ionize the material through which it is traversing. These unique properties of the neutron qualifies it as a very valuable tool for exploring the structure of the nucleus. Following its discovery, the results of research with neutrons which led to the discovery of nuclear fission and the subsequent realization of nuclear chain reaction together with the capability of harnessing nuclear energy from fission process for the generation of electricity has greatly enhanced the importance of neutrons. The fusion reactor technology (FRT) is an area of interest currently attracting the attention of nuclear scientists globally because it is deemed as an alternative to the existing nuclear fission technology (Cierjacks, 1983). All design

concepts of the proposed device of fusion reactor are based on neutrons. Furthermore the use of neutrons for analytical purposes has led to the development of very powerful methods for quantitative determination of elements and isotopes in various fields (Rakovic, 1970). Typical fields of applications of nuclear analytical methods based on neutrons include medicine, biology, material science, agriculture, industry, mineral exploration and the environment. Consequently, as it is today, the subject of nuclear physics and indeed nuclear technology can be deemed to have begun with the discovery of neutrons.

Neutron exists in nature with a short life time (Curtiss, 1959), hence it must be produced artificially through the means of nuclear reactions. The artificial method of neutron production which dates back to its discovery involves its separation from the nucleus in which it is closely bound (Beckurts and Wirtz, 1964). Modest equipment such as small accelerators, research reactors, radioactive and fission fragment sources which can be installed in laboratories and industries are available for analysis and research with neutrons. However in the last three decades, there has been consistent improvement in the quality of accelerator-based neutronsources so as to meet the requirements of developing new techniques and improving the accuracy of microscopic and macroscopic neutron data (Csikai, 1989). Neutron data investigation is an area of great importance pursued for better understanding of

nuclear structure properties, checking reaction models and developing new techniques for applications in various fields of endeavour. The adaptation of analytical techniques based on neutrons for nuclear data studies and bulk sample analysis can be used to initiate new ideas in basic research and applications in different fields. Consequently this work is aimed at meeting two objectives: a global objective and a local objective. To meet the global objective, an on-line method for the analysis and non-destructive testing of bulk samples based on the investigations of neutron fields in bulk samples consisting of coal, water and graphite has been developed. Similarly, excitation functions and isomeric cross section ratios of $^{58}Ni(n,p)^{58m+g}Co$ reaction from 5 to 15 MeV neutron energy were determined. The published results in the region between 5-13 MeV are very discrepant and there are no data for the isomeric cross section ratios. The adaptation of some of the principles and techniques developed elsewhere at the local level forms the second aim of this work. This is sequel to the opportunity at my disposal abroad where all the experiments were conducted. Therefore, the principles and techniques utilized in this work are described in details to make the adaptation of each method as easy as possible. In this regard, the experimental set-up developed for the determination of bitumen content in asphalt concrete based on the thermal neutron reflection technique has been modified to improve the sensitivity for

hydrogen in oil samples. Based on the improved set-up, the total hydrogen content and the (O+C)/H atomic ratio in different samples consisting of motor and household oils as well as crude-oil samples from Nigeria and Hungary were measured.

1.2 A Review of Previous Works

After its discovery and even before its properties were fully understood, the neutron has been used to probe the structure of the nucleus via the neutron-nuclei interactions. Since then neutron physics has provided a better understanding of the characteristics of nuclei. The parameters which are used for describing the characteristics of nuclei and their interactions are referred to as nuclear data. In general, the term "nuclear data" is broad and it includes; nuclear structure data, nuclear decay data and nuclear reaction data. The interactions of netrons clearly fall into the category of nuclear reaction data where parameters such as the cross sections, the excitation functions, the energy and the angular distributions of emitted particles are important. The matter of cross section is the very heart of neutron physics and as such cross section measurements are of fundamental importance in nuclear research and applications. A survey of the literature including the

bi-annual IAEA publication "WRENDA" (The World Request List for Nuclear Data) indicate the need for new cross section data and improvement in the accuracy of measured, calculated and recommended data (Muir, 1979; Day, 1981; Piksaikin, 1983). In this regard, the cross section curves of some dosimetry reactions which are frequently used as energy and fluence monitors as well as structural material in the fusion reactors are of high priority (Csikai, 1989). The $^{58}Ni(n,p)^{58m+g}Co$ reaction belongs to this category of priority reactions. Since all design concepts of the fusion reactor are based on the D-T reaction in which 14 MeV neutrons are produced, emphasis has now shifted to cross section measurements in the sub-14 MeV and 14 MeV regions. In recent past a number of investigations were conducted to measure the activation cross sections and the isomeric cross section ratios of this reaction from the threshold to 20 MeV. A survey of "The Index to Literature and Computer Files on Microscopic Neutron Data" CINDA-94 (1994) reveals that the data in the region between 5 and 12 MeV are discrepant. Similarly, so far there are no published data for the isomeric ratios in the same region, hence the measurement of these data were conducted.

The utilization of neutrons for the analysis of different samples has kept its leading positions among the nuclear techniques. In addition to the activation analysis technique, neutrons are also widely used in prompt radiation analysis for the determination of concentration

and spatial distributions of elements in different bulk samples and matrices. Recent advances on the use of on-line methods for the elemental analysis of bulk material have been comprehensively reviewed by Gozani, (1988). The possible combination of portable sealed-tube neutron generator with associated alpha particle head (Gordon and Peters, 1988) shows that an on-line method for the elemental analysis of bulk samples can be developed. Similarly, a pulsed fast/thermal neutron technique for the on-line characterization of coal have been suggested (Vourvopolous and Womble, 1989; Vourvopolous, 1993; Vourvopolous and Shultz, 1993; Vourvopolous and Humphrey, 1994;). The development of such a method depends on careful investigations of fast and thermal neutron flux distributions in bulk samples. These investigations together with the use of the thermal neutron reflection technique are the other objectives of this work. The thermal neutron reflection technique is a neutron physical method developed for the determination of bitumen content in asphalt concrete by Buczko *et al.*, (1975). Since then the method has been used for the investigations of different materials (Al-Jobori *et al.*, 1978; Szegedi *et al.*, 1982; Szegedi *et al.*, 1990 and Chimoye, 1991).

1.3 Present Work

The present work is devoted to the utilization of neutrons produced by isotopic and accelerator-based sources for neutron data research and bulk sample analysis. In the first part, accelerator-based neutron sources were employed to measure the activation cross sections and isomeric cross section ratios of $^{58}Ni(n,p)^{58m+g}Co$ reaction from 5 to 15 MeV. In the region between 13 and 15 MeV, neutrons were produced by the D-T reaction of a low-current neutron generator. In order to achieve a high level of precision, magnetic current of the accelerator analyzing magnet was calibrated for energy by nuclear reaction and the average energies of emitted neutrons at the sample positions were determined experimentally. In the 5-13 MeV region neutrons were produced by a variable-energy cyclotron via D-D reaction using deuterium gas cell. The discrepancy in the activation cross section data and the lack of isomeric cross section ratio data in this region may be attributed to the difficulties in determining the spectral distribution of source neutrons. Consequently, characteristics of the source spectra were determined by pulse height response spectrometry and the activation unfolding techniques.

The second part of this work covers the use of characteristic data of neutron interactions with bulk matter for in-situ or on-line quantitative analysis of

minerals. As a preliminary step at developing an on-line method for the elemental analysis of bulk samples, flux density distributions of fast and thermal neutrons in different configurations of samples consisting of coal, water and graphite were determined. The possible use of isotopic neutron sources was considered by measuring the attenuation characteristics of ^{252}Cf and Pu-Be neutrons traversing different thicknesses of coal sample. An experimental set-up (the *"BITATRON"*) developed for the determination of total hydrogen content in hydrocarbons samples was modified to improve the sensitivity for hydrogen. As a result of which the total hydrogen content and the (O+C)/H atomic ratio in motor and house oils as well as crude-oil samples were measured.

1.4 Outline of Thesis

The basic principles of neutron production and interactions together with the experimental techniques used in this work are enumerated in chapter two. The characteristics of neutron fields used in measuring the activation cross sections and the isomeric cross section ratios are described in chapter three. In chapter four, results of the excitation functions and the isomeric cross section ratios of $^{58}Ni(n,p)^{58m+g}Co$ reaction from 5 to 15 MeV are presented. Furthermore, in this chapter a

comparison between experimental and recommended data together with data obtained recently by using model calculations is given. Chapter five contains results of the neutron flux density distributions at different positions in bulk samples as well as the attenuation characteristics of neutrons traversing different thicknesses of coal. The total hydrogen content and the O+C/H atomic ratio in crude oil samples of different origins and some commonly used oil samples are stated in chapter 6. Summary, conclusion and recommendations are presented in chapter 7.

CHAPTER TWO

2.0 PRINCIPLES AND TECHNIQUES OF NEUTRON INTERACTIONS

The utilization of neutrons for research and analysis involves a thorough understanding of the principles of neutron production and interaction together with a knowledge of the techniques involved in conducting the investigations. In this respect, the fundamental properties of neutrons as well as a classification of neutrons based on their kinetic energies are outlined. Similarly, the interactions of neutrons with nuclei and bulk matter as well as the techniques of measuring these interactions are discussed. The characteristics of neutron sources other than fission reactors used in this work are described. The advantages, disadvantages and the the fields of application of each of the sources are discussed. The neutron activation analysis, the thermal neutron reflection and the pulse height response spectrometry technique adopted in the investigations are enumerated.

2.1 Properties and Classifications of Neutrons

2.1.1 Basic properties of the neutron

Very soon after its discovery, a number of experiments were performed to study the properties of the neutron. Results of such measurements reveal that neutrons are

unstable and decay with a half-life of a few hundred of seconds. They obey the Fermi-Dirac statistics and like electrons exhibit wave properties. Some of the well-known properties which are of fundamental importance in understanding the characteristics of neutrons and their interactions are summarized in Table 2.1.

Table 2.1 Some basic properties of the neutron.

mass (Kg)	charge (e)	spin (ħ)	half-life (s)
1.675×10^{-27}	0	1/2	641±8

(taken from Curtiss, 1959)

2.1.1 Classification of neutrons

To study the interactions of neutrons with matter, it is desirable to classify neutrons according to their kinetic energies. However, the classification of neutrons in general do not have clearly defined boundaries but it is often necessary for an understanding of the different types of interactions. A common classification is given below:

Slow neutrons: These are neutrons having energies in the range between 0 keV and 1000 eV. However in this range a number of sub-classifications occur. These are the cold neutrons, the thermal neutrons, the epithermal neutrons and the resonance neutrons. Cold neutrons are those with an average kinetic energy below the average thermal energy of the surrounding medium. Thermal neutrons are neutrons which

have average energy approximately equal to the energy of atoms of the surrounding medium (*i.e.* E_n= 0.025 eV) at room temperature. Epithermal neutrons are those thermal neutrons whose energies are not completely in thermal equilibrium with the atoms of the surrounding medium (*i.e.*0.02 eV < E_n < 0.5 eV). Neutrons with average energy between 1 and 1000 eV are regarded as resonance neutrons.

Intermediate neutrons: Neutrons having kinetic energy in the range between 1000 eV and 0.6 MeV are classified as intermediate neutrons. Very little information is available about the intermediate neutrons because of the difficulties involved in finding efficient detectors for their detection. Furthermore, sources of these types of neutrons are very few and there has been little or no progress in the study of their interactions with matter.

Fast neutrons: The region of energy between 1000 keV and 50 MeV is often considered as the fast range of neutron energies. Neutrons with energy in the spallation region (*i.e.*$E_n \geq$ 100 MeV) are regarded as ultra-fast or high energy neutrons. Majority of the neutron sources that are widely used in teaching and basic nuclear research are fast neutron sources. Consequently, characteristics of radioisotope and accelerator-based neutron sources used in this work together with the principles of neutron interactions are discussed.

2.2 Interaction of Neutrons with Matter

The interactions of neutrons with matter can lead to a variety of phenomena depending on the energy of incident neutron and on whether the interaction is with a nucleus or with a bulk matter. The interactions with nuclei are used for probing the structure of the nucleus whereby important parameters such as cross sections are determined. However, the interactions with bulk media are used for quantitative and qualitative assay of such media. The experimental investigations conducted here are based on both types of interactions which are enumerated below.

2.2.1 Interactions of neutrons with nuclei

In general, the interactions of neutrons with nuclei give rise to nuclear reactions depending on the type of process involved. The process may be a compound nucleus process or a direct reaction process or both depending on the open channel. In direct reaction process, an incident neutron is scattered from the nuclear potential without actually entering the nucleus. This process is also known as potential scattering process and may be elastic or in-elastic. The direct elastic process is essentially a billiard-ball type of interaction in which the energies of both incident and emitted neutron are equal. However, in direct in-elastic scattering process, incident neutrons of energies greater than that of the first excited state of a

target nucleus may excite the target nucleus. De-excitation of the excited nucleus takes place without the formation of a compound nucleus via the following processes: direct in-elastic process, charge exchange process, pick-up or knock-out process. Interaction of neutrons leading to the formation of a compound nucleus occurs when a target nucleus absorbs an incident neutron for a relatively long time compared with the time it would have taken the neutron to move through a nuclear diameter. The target nucleus having gained certain excitation energy may decay via a variety of processes independent of the way in which it was formed. Like the direct reaction process, de-excitation of the compound nucleus may be via the processes stated above but in addition, radiative capture and fission processes are equally likely. A schematic diagram of the processes resulting from interaction of neutrons with a nucleus is shown in Figure 2.1.

In certain cases a radioactive isomer may be formed depending on the spins of the levels of gamma transition. If the spin value belonging to one of the discrete levels is substantially different from that of the ground level, the mean-life of the level would be long and as such measurable. In such a case, the product radionuclide is said to be in metastable or isomeric state and may decay via gamma-ray emission or internal transition. Neutron induced nuclear reaction processes which are related to the experiments in this work are outlined below:

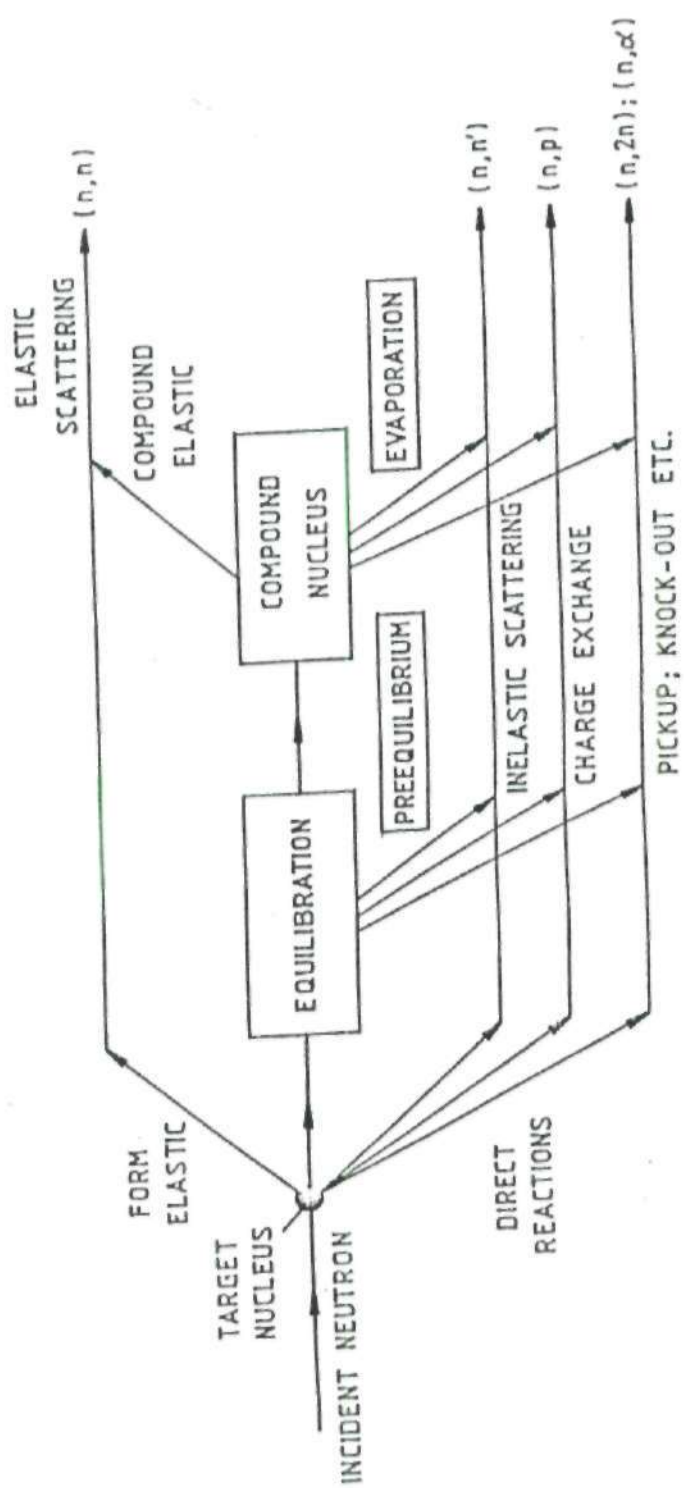


Fig. 2.1 A schematic diagram of neutron-nucleus interaction processes

The (n,γ) reaction: This reaction is also known as the neutron capture reaction and it is the most common reaction in the activation of nuclei by thermal neutrons. The incident neutron is completely absorbed by a target nucleus with the emission of a prompt γ-ray. The process is generally represented by the equation below.

$$ {}^{A}_{Z}X + {}^{1}_{0}n = {}^{A+1}_{Z}Y + \gamma \qquad 2.1 $$

The cross sections of this reaction for majority of elements decreases with increasing neutron energy and it is predominant in the thermal neutron energy region. However, for some nuclei this reaction has high resonances above the thermal neutron energies but the cross sections for fast neutrons can be neglected when compared to those obtained for thermal neutrons. A typical example is the $^{115}In(n,\gamma)^{116}In$ reaction which is recommended as a thermal neutron flux monitor reaction because of its high thermal neutron cross section.

The (n,n') reaction: This reaction is an inelastic scattering process in which the kinetic energy of emitted neutron is less than the kinetic energy of incident neutron thereby leading to the formation of residual radionuclide in the excited state. The reaction is written as shown below.

$$ {}^{A}_{Z}X + {}^{1}_{0}n = {}^{A}_{Z}X^{*} + {}^{1}_{0}n' \qquad 2.2 $$

The residual nucleus in the excited state decays to the ground state of a stable nucleus via electron capture (EC), internal conversion (IT) or beta-decay (β-decay) accompanied by the emission of gamma-ray. The excited nucleus is said to be in the isomeric or metastable state, a typical example is the $^{115}In(n,n')^{115m}In$ reaction. The prime denotes that the neutron is degraded in energy with respect to the incident neutron and the m of ^{115m}In denotes that the product is a metastable state of the ^{115}In isotope. This reaction with a threshold of 0.8 MeV is a useful dosimetry reaction for unfolding neutron fields and it is also used as a fluence monitor for 3 MeV neutrons because of its relatively high reaction cross section in this region.

The (n,p) reaction: The (n,p) reaction is endoergic which proceeds by the exchange of a proton by a neutron in the nucleus of the target atom. The process is written in the form below.

$$ {}^{A}_{Z}X + {}^{1}_{0}n = {}^{A}_{Z-1}X + {}^{1}_{1}p \qquad 2.3 $$

The probability of occurrence of this reaction depends on the height of the Coulomb barrier which increases from about 1 MeV at Z = 3 to about 12 MeV at Z = 90, where Z is the atomic number of the product nucleus. In most cases, the residual radionuclides are beta emitters and they often decay to the original target nuclei. A typical example is

the (n,p) reaction on ^{27}Al described by the expression below.

$$^{27}Al(n,p)^{27}Mg \xrightarrow{\beta^-} {}^{27}Al \qquad 2.4$$

The (n,α) reaction: This reaction is not as prominent as the (n,p) reaction at low neutron energy because of the high Coulomb barrier for the emission of an α-particle. The barrier increases from about 1 MeV at Z = 2 to about 22 MeV at Z = 90, but like (n,p) reactions, the probability decreases with increasing atomic number. This explains why the reaction is more prominent among lighter elements. A typical example is the $^{6}Li(n,\alpha)^{3}H$ reaction and the $^{10}B(n,\alpha)^{7}Li$ reaction which are used for the detection of thermal neutrons. Similarly, the $^{27}Al(n,\alpha)^{24}Na$ reaction is a very useful dosimetry reaction in the region between 0 and 20 MeV for flux measurements and unfolding of neutron fields. The form of this reaction is given below.

$$^{A}_{Z}X + {}^{1}_{0}n = {}^{A-3}_{Z-2}X + {}^{4}_{2}He \qquad 2.5$$

The (n,2n) reaction: This reaction is endoergic and it occurs when the scattered neutron gives enough energy exceeding the binding energy of the last bound neutron in the nucleus of the target atom. The average binding energy of neutron is between 6 MeV and 8 MeV therefore, only high energy neutrons can be used to produce such reactions. The cross section curve of the (n,2n) reaction can be well

described by the formula (Weisskopf and Erwing, 1940).

$$\sigma_{n,2n} = \sigma_{nM}.[\ 1-(1+\frac{\varepsilon}{T}).e^{-\varepsilon/\ T}] \qquad 2.6$$

where, $\varepsilon = E_n - B_n.\frac{A+1}{A}$ is the excess energy, T is the nuclear temperature and σ_{nM} is the neutron emission cross section which is equal to the non-elastic cross section (σ_{NE}) for the medium and heavy nuclei. The (n,2n) reaction can be written as:

$$^{A}_{Z}X + ^{1}_{0}n = ^{A-1}_{Z}X + 2^{1}_{0}n \qquad 2.7$$

Typical examples of this reaction are the $^{93}Nb(n,2n)^{92m}Nb$ which is used as a flux monitoring reaction around 14 MeV neutron energy. Similarly the $^{90}Zr(n,2n)^{89}Zr$ reaction in combination with the $^{93}Nb(n,2n)^{92m}Nb$ reaction have been recommended as energy monitors for 14 MeV neutrons (Csikai *et al.*, 1986).

2.2.2 Interactions of neutrons with bulk matter

Interactions of neutrons with the masses of a material in which encounters are made with many nuclei by the neutrons can lead to a number of physical effects that are used in nuclear analytical techniques. Process like slowing-down or moderation of fast neutrons which is very useful in the fission reactor technology are predominant. The slowing-down of neutrons is brought about by repeated collisions with large masses of nuclei of the material.

Elastic scattering process is the predominant way by which the collisions proceed. To understand some of the principles and techniques in this work, the theory of slowing-down process is summarized below.

Theory of slowing-down of fast neutrons: Consider a neutron of mass M_1 and of initial energy E_1 which collides with a free atomic nucleus of mass A initially at rest. The dynamics of the collision in both in laboratory system and centre of mass system is presented by the diagrams of Figures 2.2a and 2.2b. respectively. The relationship between the velocities in both frames of reference (*i.e.* V_a, V_m, and V_1) is illustrated in Figure 2.2c.

From the diagrams and using the cosine formula, the following equations are obtained .

$$V_2^2 = V_a^2 + V_m^2 + 2V_a.V_m.\cos\theta \qquad 2.8$$

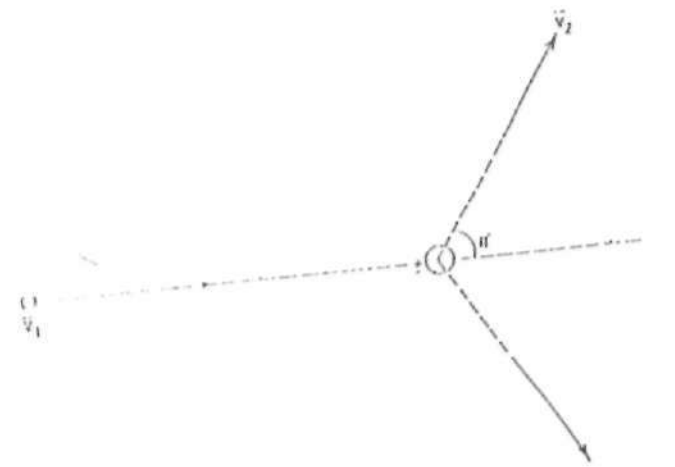
and

$$V_2.\cos\phi = V_a.\cos\theta + V_m \qquad 2.9$$

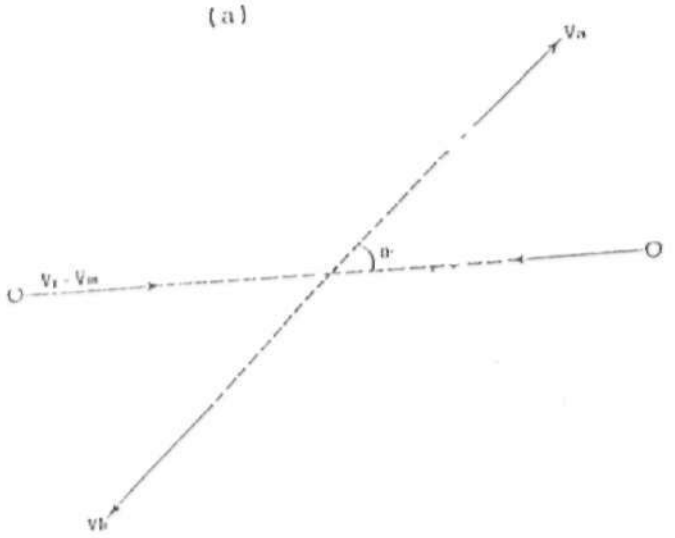
Since momentum is conserved , then the velocity of the centre of mass is obtained from the fact that the total momentum in the centre of mass system is equal to that of the laboratory system. Thus equation 2.10 is obtained.

$$(A + M_1)\, V_m = M_1\, V_1 \qquad 2.10$$

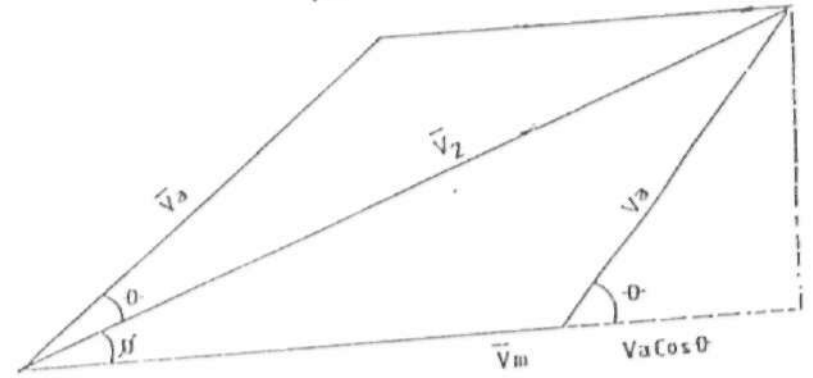
Given that $M_1 = 1$ (*i.e.* mass of a neutron)



(a)



(b)



(c)

Fig. 2.2 Dynamics of neutron collisions in (a) laboratory system (b) centre of mass system and (c) the relationships between the velocities in both systems

thus,

$$V_m = \frac{V_1}{A+1} \qquad 2.11$$

However the velocity of neutron in the centre of mass system before collision is given below as:

$$V_1 - V_m = \frac{A}{A+1} V_1 \qquad 2.12$$

In addition to this, the momentum of the neutron and that of the atomic nucleus in the centre of mass system are equal and are oppositely directed before collision. Consequently, after collision they must still be and oppositely directed. Furthermore, in elastic collision energy is conserved hence the velocity of the neutron and that of the atomic nucleus must be the same as the pre-collision velocities, thus the expression below is obtained.

$$V_a = \frac{A}{A+1} V_1 \qquad 2.13$$

The kinetic energy of the neutron after collision is given below as:

$$E_2 = \frac{1}{2} M_1 V_2^2 \qquad 2.14$$

From equations 2.8, 2.11 and 2.13 the following expressions are obtained.

$$V_2^2 = \frac{A^2}{(A+1)^2} V_1^2 + V_1^2 \frac{1}{(A+1)^2} + 2 \frac{A V_1^2}{(A+1)^2} \cos\theta \qquad 2.15$$

$$V_2^2 = V_1^2 \frac{(A^2 + 2A\cos\theta + 1)}{(A+1)^2} \qquad 2.16$$

multiplying equation 2.16 by $M_1/2$ results in;

$$\frac{M_1}{2} V^2 = \frac{M_1}{2} V^2 \frac{(A^2 + 2A\,Cos\theta + 1)}{(A+1)^2} \qquad 2.17$$

$$E_2 = E_1 \frac{(A^2 + 2A\,Cos\theta + 1)}{(A+1)^2} \qquad 2.18$$

where, E_1 = neutron energy before collision

E_2 = neutron energy after collision and

θ = Scattering angle in the centre of mass system

The scattering angle in the laboratory system ϕ is given by

$$Cos\phi = \frac{A\,Cos\theta + 1}{(A^2 + 2A\,Cos\theta + 1)^{1/2}} \qquad 2.19$$

Introducing an auxiliary quantity

$$\alpha = \frac{(A-1)^2}{(A+1)^2} \qquad 2.20$$

equation 2.2.18 becomes

$$\frac{E_1}{E_2} = \frac{1}{2}[(1+\alpha) + (1-\alpha)Cos\theta] \qquad 2.21$$

The maximum energy loss occurs in a head-on-collision *i.e.* collision for which $\theta = 180^{\circ}$ ===> $Cos\theta = -1$

$$\Longrightarrow \quad E_2 = \alpha E_1 \qquad 2.22$$

This means that the energy cannot fall below αE_1 as a result of a single elastic collision.

The energy loss per collision *i.e.* $\Delta E = E_1 - E_2$ becomes:

$$i.e. \qquad \Delta E = \frac{2A(1 - Cos\theta)}{(A + 1)^2} . E_1 \qquad 2.23$$

For a head-on-collision;

$$E_2 = \frac{4A}{(A + 1)^2} E_1 \qquad 2.24$$

For hydrogen, A=1, therefore α=0 and ΔE=0

However, for large value of A, equation 2.20 reduces to;

$$\alpha = 1 - \frac{4}{A + 2} \qquad 2.25$$

The geometrical average of the ratio E_1/E_2 which is in fact equal to $\ln \frac{E_1}{E}$ defines a constant ξ and is given as:

$$\xi = \ln E_1 - \ln E_2 \qquad 2.26$$

The last term of equation 2.26 leads to a physical interpretation on the average logarithmic energy decrement per collision. The maximum loss of energy is given below as

$$E_2 = \frac{(A - 1)^2}{(A + 1)^2} E_1 \qquad 2.27$$

The scattering is isotropic in the centre of mass system,

$$\therefore \xi = 1 + \frac{(A + 1)^2}{2A} \ln\frac{(A - 1)}{(A + 1)} \qquad 2.28$$

ξ = 1 for hydrogen and for large A it can be approximated as follows:

$$\xi = \frac{2}{A + 2/3} \qquad 2.29$$

The quantity ξ makes it possible to estimate the average number of collisions (η) necessary to moderate a neutron with incident energy E_1 to E_2 and it is given as:

$$\eta = \frac{\ln(E_1/E_2)}{\xi} \qquad 2.30$$

2.3 Neutron Sources

Because of the very short life time of occurrence of neutrons in nature, they must be produced artificially through nuclear reactions. The reactions may be induced by the α and γ radiations from radioactive nuclei, or by charged particles from accelerating devices, or by the nuclear fission of heavy elements. Consequently, neutron sources are classified based on the type of reaction leading to the production of neutrons. The general classifications described below are as follows;

radioisotope neutron sources; fission neutron sources; and accelerator-based neutron sources.

2.3.1 Radioisotope neutron sources

Radioisotope neutron sources are the simplest sources of producing neutrons. The source consists of a target material mixed with a naturally decaying radioactive component which supplies the bombarding radiation used in the release of neutrons. This method of production of neutrons dates back to the discovery of neutrons when the first observed neutrons were produced by bombarding targets of boron and beryllium by α-particles from the decay of polonium. There are several types of radioactive neutron sources differentiated by the nature of the target material and by the radioactive nuclei producing the bombarding radiation. Major draw backs of isotopic neutron sources neutron source include the low yield of neutrons, broad neutron spectra and the inability to be turned-off at will. Widely known radioisotope neutron sources are:

Radioisotope (α,n) neutron sources: The most common reaction used for the production of neutrons via the (α,n) reaction is the reaction that led to the discovery of the neutron.

i.e. $$^{9}_{4}Be + ^{4}_{2}He = ^{12}_{6}C + ^{1}_{0}n + 5.71\ MeV \qquad 2.31$$

A beryllium target was bombarded by α-particles produced by naturally occurring radioactive elements such as polonium, radium, plutonium, and americium. Characteristics of these types of sources are summarized in Table 2.2.

Table 2.2 Characteristics of some Be(α,n) neutron sources.

Source	Half-life	E_{α} (MeV)	Neutron yield per 10^6 α's	
			calculated	experiment
^{239}Pu-Be	24,000 y	5.14	65	57
^{238}Pu-Be	87.4 y	5.48	79	-
^{241}Am-Be	433 y	5.48	82	70
^{241}Cm-Be	18 y	5.79	100	-

(Taken from Cierjacks, 1983).

Figure 2.3 shows the neutron spectra of the Pu-Be source used in this work which is typical of radioisotope (α,n) sources.

Radioisotope(γ,n) sources: Gamma-ray radioisotope emitters are used to produce neutrons whenever they are mixed with appropriate target nuclei. There are only two nuclei which have thresholds for (γ,n) reaction within the range of energies of γ-rays emitted by radioisotopes in their decay processes. These photo neutron sources are deuterium and beryllium and they produce neutrons based on the following reactions.

$$^{9}Be + \gamma = {}^{8}Be + {}^{1}n - 1.666MeV \qquad 2.32$$

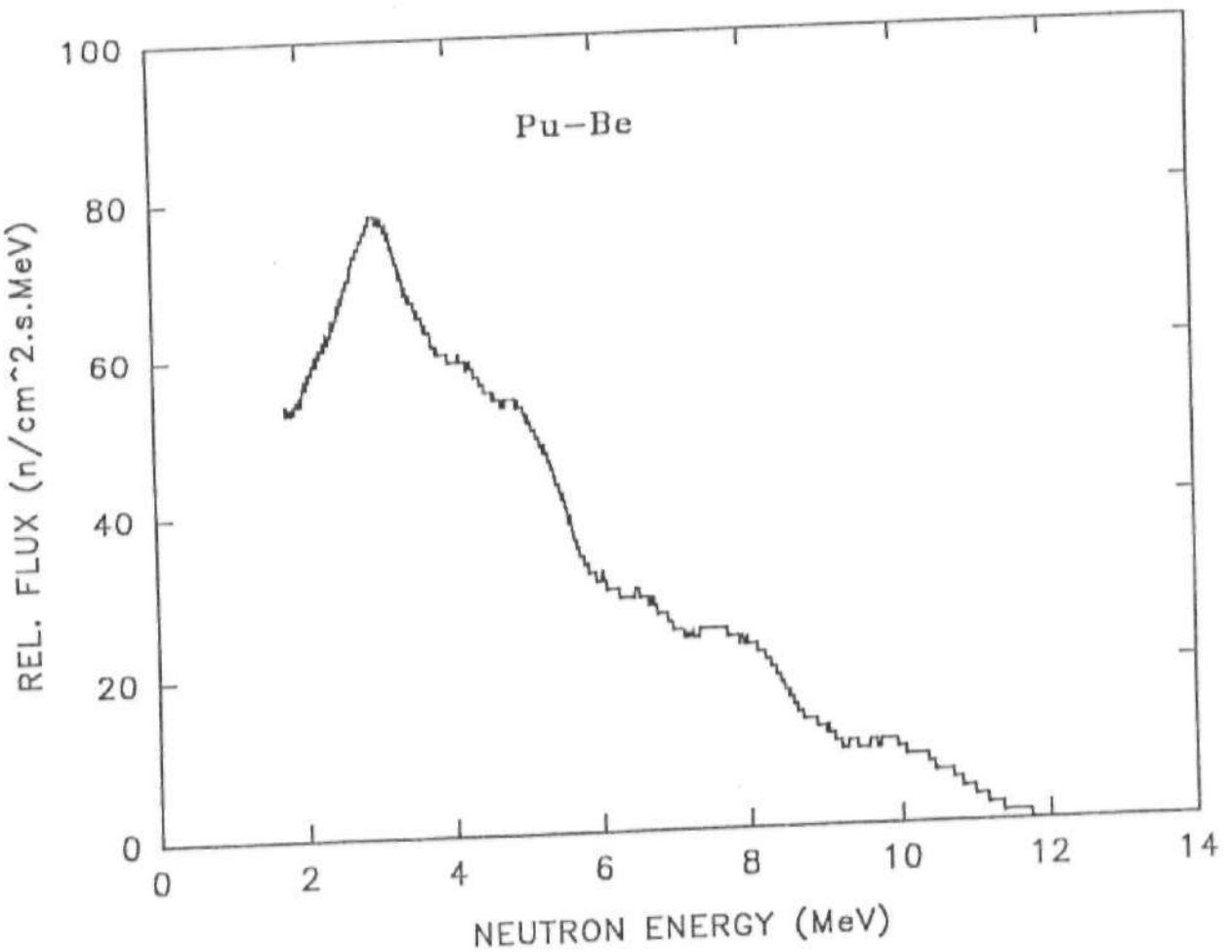


Fig. 2.3 Energy spectra of the Pu-Be neutron source used in this work

$$^{2}H + \gamma = {}^{1}H + {}^{1}n - 2.226MeV \qquad 2.33$$

In the nuclei of these sources, the binding energy of the last neutron is low therefore it is possible to liberate a neutron through the absorption of a γ-ray with low energy such as those produced by a common γ-ray emitter. One advantage of the photo neutron is that it is possible to produce monoenergetic neutrons provided that the incident γ-rays are monoenergetic. However,the disadvantage is that for the production of neutrons of useful intensities, incident γ-rays of comparatively high activity are required, necessitating the use of large shielding and remote handling techniques.

2.3.2 Fission neutron sources

Heavy atomic nuclei decaying by spontaneous fission may emit high intensity neutrons, hence some of these heavy nuclei can serve as neutron sources. The low rates of heat emission, and gamma radiation allow the fabrication of simple, small ^{252}Cf sources that require no external power supply nor maintenance but that can provide moderately high neutron flux. Like (α,n) neutron sources, the energy spectrum is broad but the shape can be well represented by the Maxwellian expression given below

$$N(E) = k\, E^{1/2} \exp(-E/T) \qquad 2.34$$

where, $K = 2/\pi^{1/2}\ (1/T)^{3/2}$ is a constant,

E is the energy of neutrons,

and T is the Maxwellian temperature (T = 1.42 MeV) taken from Mannhart, (1987).

The neutron energy spectra of a ^{252}Cf source used in this work (Figure 2.4) was measured by the pulse height response spectrometer and was found to follow the Maxwellian distribution. The ^{252}Cf source can be used for the calibration of neutron detectors because the Maxwellian temperature is a characteristic parameter of its spectrum. Consequently, for the pulse height response spectrometer described in section 2.4, a value of Maxwellian temperature (T = 1.412±0.016 MeV) was deduced from ^{252}Cf neutron spectrum which validates the use of the PHRS system to measure the spectra of neutrons above 2 MeV neutron energy.

2.3.3 Accelerator-based neutron sources

The requirement of neutrons having higher energies and intensities led to the production of neutrons by the method of artificially accelerated particles. Generally, monoenergetic neutrons can be produced via nuclear reactions in linear accelerator and cyclotron. In linear accelerators, charged particles are accelerated in straight paths while in cyclotrons, they are accelerated in spiral or circular paths. In both types of accelerators, charged particles mainly deuterons are accelerated at high energies to overcome the potential barrier and penetrate the nucleus of appropriate target element. The neutrons hereby produced have relatively high yield at a given energy, good energy

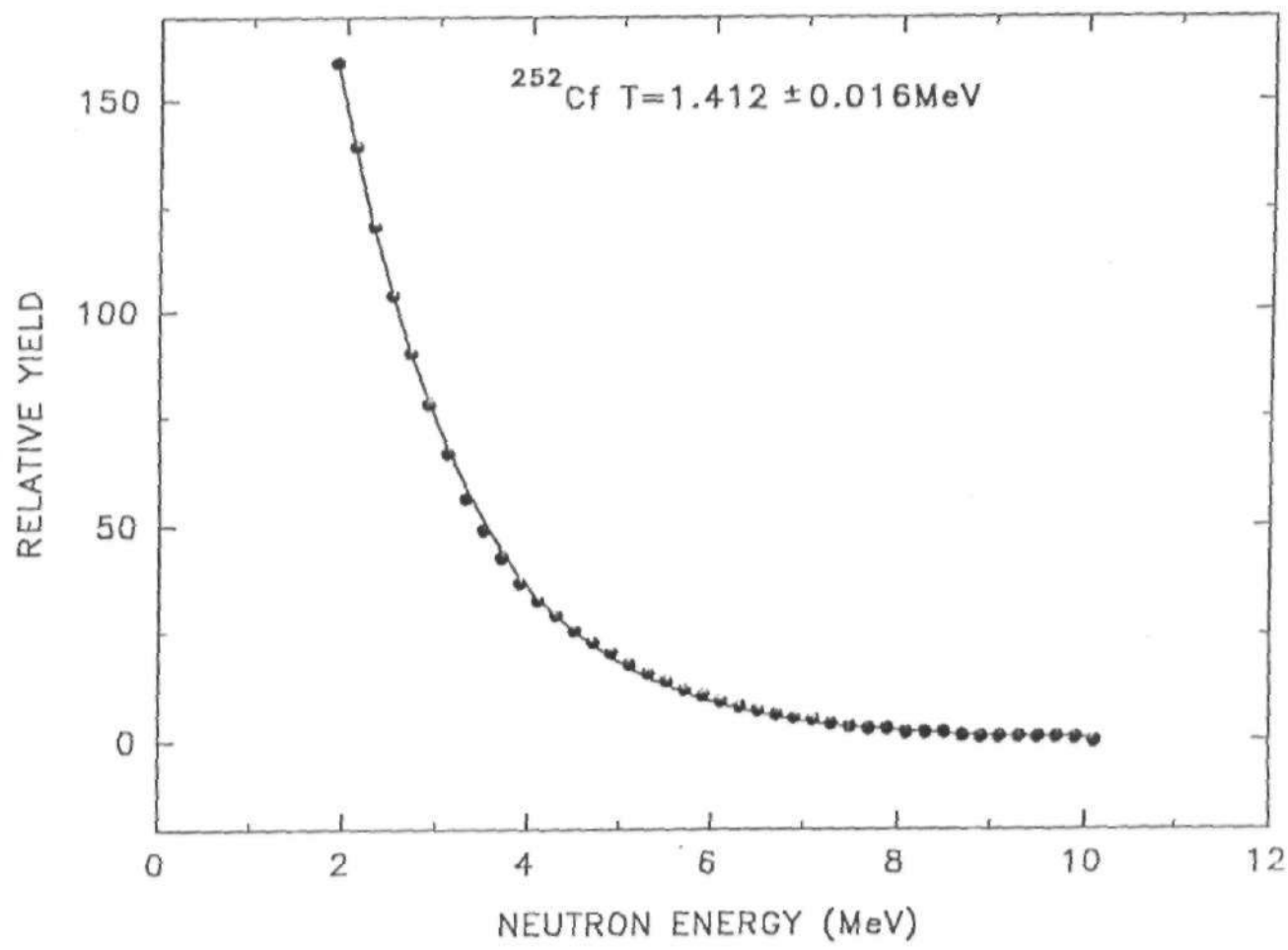


Fig. 2.4 Energy spectra of the ^{252}Cf neutron source used in this work

resolution and low degree of contamination from background neutrons. These properties of emitted neutrons are important in the determination of excitation functions and other nuclear data studies. Compared with radioisotope neutron sources, accelerator-based neutron sources are larger in size and are more expensive thereby requiring correspondingly higher investments and operational costs.

In most accelerator-based neutron sources, the neutron producing reaction usually consists of light particles interacting with light elements. This is because light nuclei provide low potential barriers to bombarding particles and light particles can be accelerated to sufficiently high energies. Some of these reactions and their most important parameters are summarized in Table 2.3

Table 2.3 Neutron producing reactions in accelerator-based neutron sources.

Nuclear reaction	Q-value (MeV)	Break-up threshold (MeV)	Neutron energy* range (MeV)	Target
$^{7}Li(p,n)^{7}Be$	-1.64		0.2-1.0	Li
$^{3}H(p,n)^{3}He$	-0.76	8.35	0.7-3.0	Ti-T
$^{2}H(d,n)^{3}He$	+3.27	4.50	2.0-5.0 5.0-13.0	Ti-D D_2 gas
$^{3}H(d,n)^{4}He$	+17.59	3.71	13.0-20.0	Ti-T
$^{2}H(t,n)^{4}He$	+17.59	24.99	14.0-26.0	D_2 gas

* depends on angle of emission.
(Data taken from Barschall, 1983).

Among the reactions in Table 2.3 those based on hydrogen are prominent for producing neutrons over an energy range of between 1 and 20 MeV. As can be seen, reactions involving deuterons and tritons are non-threshold reactions having low Q-values and low atomic numbers. Because tritium beams are difficult to handle and the fact that tritium is an active material which is seldom available , neutron producing reactions based on deuterium beams are preferred. Neutron sources operating based on $^{2}H(d,n)^{3}He$ and $^{3}H(d,n)^{4}He$ are known as D-D and D-T sources respectively. The letters D-D and D-T are written in the context of capital letters describing the particle which reacts with a corresponding target. In this respect, the neutron generator and the variable-energy cyclotron are widely used as sources of neutrons in the range between 2 and 15 MeV to determine excitation functions.

The neutron generator: The design characteristics of a neutron generator are such that high current beams of deuterons are accelerated to penetrate tritium or deuterium nuclei for the production of neutrons. The neutron producing reactions are given below.

$$^{2}H + ^{2}H = ^{3}He + ^{1}n + 3.268\ MeV \qquad 2.35$$

$$^{2}H + ^{3}H = ^{4}H + ^{1}n + 17.6\ MeV \qquad 2.36$$

From the kinematics of the above equations it is

evident that the mean energies of emitted neutrons are 2.6 and 14.6 respectively. As earlier on stated the energies of neutrons can vary as a function of emission angle. Consequently the energy of D-D neutrons vary between 2 and 3 MeV while that of D-T neutrons vary between 13 and 15 MeV. It has been shown that the yield of D-T neutrons is about 100 times greater than that of D-D neutrons at typical bombarding energy of 100 keV (Barschall, 1983), therefore the D-T reaction in which 14 MeV neutrons are produced are most widely used. Typical yields of neutrons as a function of deuteron energy produced via the D-D and D-T reactions of a neutron generator are displayed in Figure 2.5.

The major components of a neutron generator include: a high voltage power supply, an ion source, an acceleration system, a target assembly and a vacuum system. For convenience neutron generators having source strength below 10^{12} n/s are classified as standard sources while those with higher source strength are referred to as intense sources. Both types can be constructed based on the traditional deuteron accelerator or the sealed-tube generator. In this work, a low-current neutron generator and a high-current neutron generator were used to produce neutrons via the D-T reaction. The characteristics of the beam and bombarding neutron energies for the low-current neutron generator were determined experimentally. Results of the measurements and the operating parameters of this source used in the

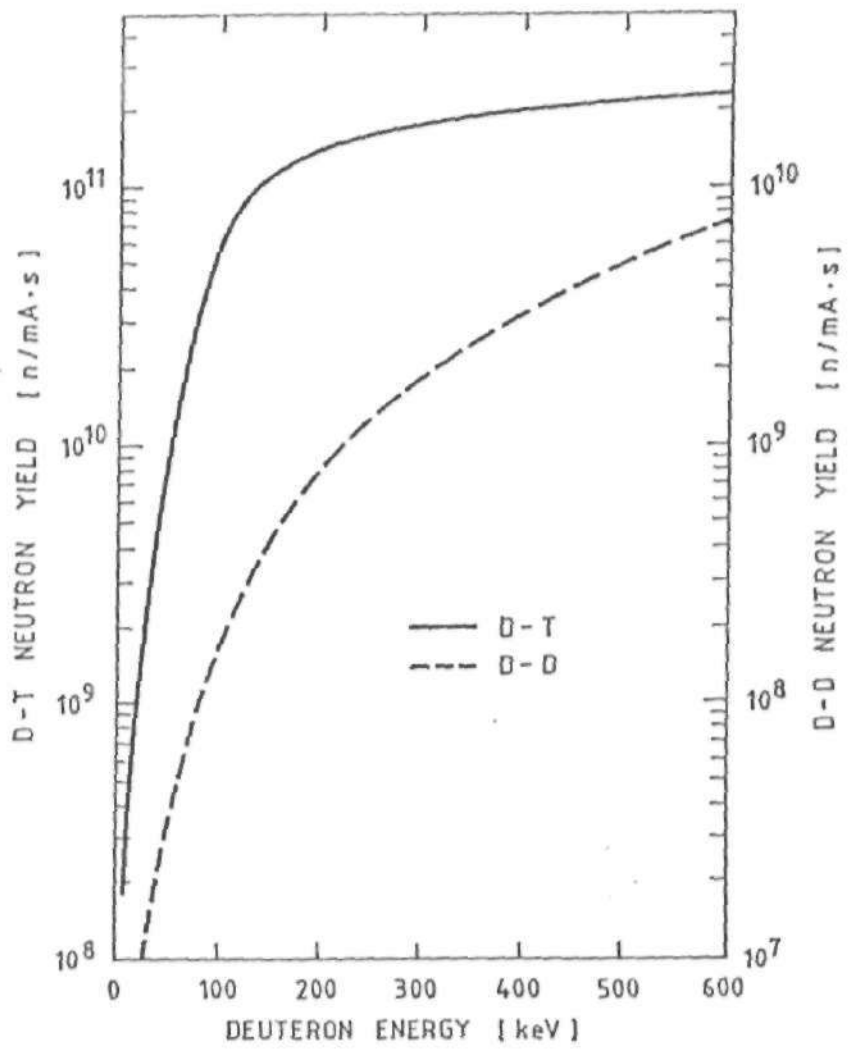


Fig. 2.5 Typical total yield of D-D and D-T neutrons versus deuteron energy

determination of excitation functions from 13 to 15 MeV are given in chapter 3.

The cyclotron: The cyclotron is the first accelerator to produce proton beams of high energy without the use of correspondingly high voltage (Burcham, 1963). It is based on the principle of magnetic resonance in which an electromagnet is used to accelerate charged particles in circular orbits. At a given frequency, the energy of accelerated particles is proportional to the maximum permissible radius therefore, the energy of accelerated particles can be varied according to the cyclotron frequency. Usually, beam extraction and transport take place in a region of rapidly falling magnetic field thereby rendering possible beam focusing onto a distant target. The cyclotron used in part of this work is a compact, isochronous and variable-energy MGC-20 cyclotron situated at the premises of the Hungarian Institute of Nuclear Research, Debrecen. It is designed for multi disciplinary research programmes and consists of a high voltage power supply, a radio frequency ion source, an electrostatic deflector with passive magnetic channel and an oil-diffusion vacuum system. The beam transport system is designed to transport accelerated particles to five target rooms for different research purposes (Kormany *et al.*, 1989). In one the target rooms, fast neutrons can be produced by protons of energy between 2 and 20 MeV or by deuterons of energy between 1 and 10 MeV. In this work,

deuterons of appropriate energies were used to bombard a deuterium gas for the production of neutrons having energies from 5 to 13 MeV. Characteristics of the neutron fields produced were determined by experimental techniques and are discussed in chapter 3.

2.4 Experimental Techniques

Several experimental techniques used for investigating neutron interactions have been in existence since the discovery of neutrons. The choice of a particular type of technique depends on a number of factors but principally on the parameter of neutron interaction under investigation. Generally, the techniques are classified as either an on-line technique or an off-line technique. Majority of the on-line techniques are suitable for spectrum measurement while the off-line techniques are suited for the measurement of reaction products. Neutron spectrum are often measured by the time-of-flight (TOF) system or by the detection of recoil-protons resulting from neutron interaction with hydrogen atoms (*i.e.* the pulse height response system). Similarly the thermal neutron reflection technique using BF_3 counter in a special geometry for the detection of thermal neutrons belongs to this group. Other on-line techniques such as the counter telescope and the quadrupole spectrometer are suitable for charged particles. The off-line techniques include the mass spectrometry, the

accelerated mass spectrometry and the activation analysis techniques. While the mass and the accelerated mass spectrometries are used mainly for long-lived radioactive and non-active products, the activation analysis technique in combination with gamma-ray spectrometry is suitable for radioactive products. The activation analysis, the pulse height response spectrometry and the thermal neutron reflection techniques were adapted for the investigations. Detail description of the set-ups and the principles are outlined below.

2.4.1 The activation analysis technique

This non-destructive analytical method dates back to 1936 when it was first reported (Hevesy and Levi, 1936). Some samples containing the mixtures of rare earths were bombarded by neutrons to determine the contents of dysprosium and europium on the basis of the induced activity. Activation analysis has since become one of the most important methods of elemental analysis. The method has been well adapted in biology, medicine, criminology and other fields because of the accuracy and the reproducibility of results.

Principle of fast neutron activation analysis: When a sample is irradiated by a beam of particles different nuclear reactions take place producing some radionuclides. The radionuclides produced can be identified through their half-lives and the energy of the emitted radiations (β-rays

or γ-rays). If the intensity of such a radiation is also measured, then the concentration of the elements in the sample *from* which the *respective radio nuclei* was produced can also be determined. Both charged particles (protons or alphas) and uncharged particles (gammas or neutrons) can be used for irradiation. The neutrons are the most advantageous because of the large interaction cross sections and the relative cheapness of production.

Basic equation of activation analysis: Consider a certain activation process having a reaction cross section $\sigma(cm^2)$. Let N be the number of radioactive nuclei formed in time t, n the number of the target nuclei, ϕ the neutron flux, and λ the decay constant of the radio nuclide formed. Then the increase in the number of radio nuclide as a function of time t from the beginning of the activation can be described by the differential equation

$$\frac{dN}{dt} = \phi \sigma n - \lambda N \qquad 2.37$$

where the first term on the right-hand side expresses the rate of increase in the number of radio nuclide formed by the activation while the second term expresses their rate of loss by decay.

The solution of the first-order linear differential equation after integration and substitution of the conditions (t = 0 and N = 0) can be written as thus:

$$N = \frac{\phi \sigma n}{\lambda} (1 - e^{-\lambda t}) \qquad 2.38$$

The activity A(t) at time t (*i.e.* the number of decays per unit time) is given as;

$$A(t) = \lambda N(t) = \phi \sigma n (1 - e^{-\lambda t}) \qquad 2.39$$

The product $\phi\sigma n$ is the activity obtained after activation lasting for infinite time and is known as the saturated activity, A_{sat}, (assuming $t = \infty$). The activity of the given radio nuclide grows at a rate which diminishes with time and in practice it is not reasonable to prolong activation for more than 2 or 3 times the half-life of the radio nuclide under investigation because further prolongation only results in a rather small improvement in approaching the saturation activity value. However, at a time t_c after the end of the irradiation, the value of the activity decreases exponentially and is given by the equation below.

$$A(t_c) = A(t)\ e^{-\lambda t_c} \qquad 2.40$$

where t_c is the cooling time. If the activity measurement is performed during a time t_m after the cooling time t_c, then the the expected number of decay events D_N is

$$D_N = \frac{\phi \sigma n}{\lambda} (1 - e^{-\lambda t})\ e^{-\lambda t_c} (1 - e^{-\lambda t_m}) \qquad 2.41$$

The average number of counted decay events (C_N) is less than D_N as a result of different effects such as the limited efficiency of the detector (η), the self-absorption correction (ε_a), the dead time correction (ε_d), cascade coincidence correction (ε_c), correction due to time variation in neutron flux (ε_f) and the emission probability of the measured γ-line (I_γ).

$$i.e.\quad C_N = \eta.\varepsilon_a.\varepsilon_c.\varepsilon_d.\varepsilon_f.I_\gamma.D_N \qquad 2.42$$

Therefore from the equations above we have the basic equation of the activation analysis as:

$$C_N = \frac{\varepsilon_a.\varepsilon_c.\varepsilon_d.\varepsilon_f.\eta.I_\gamma.\sigma.m.f.N_a}{\lambda.M}.(1-e^{-\lambda t}).e^{-\lambda t_c}.(1-e^{-\lambda t_m}) \qquad 2.43$$

where m is the mass of the element in the sample,

M is the atomic number of the element,

f is the isotopic abundance of the target isotope,

σ is the cross section (in cm^2) and

N_a is the Avogadro's number

Activity measurement by the use of gamma spectrometers:

Most radionuclides formed in neutron activation analysis are gamma or beta-gamma emitters. Further decay by the emission of positrons, IT or EC is also accompanied by gamma ray emission. The gamma-rays are emitted in groups possessing specific line energy and as such a decaying

radionuclides may have one or more monoenergetic group of gamma-rays. Thus the gamma ray energy is used as an analytical property thereby making it possible to differentiate individual radio nuclides by a gamma spectrometer.

Multichannel gamma spectrometers are the most useful for neutron activation analysis because they make possible the simultaneous measurements in many channels (Derbertin and Helmer, 1988). The modern detectors are the scintillation detector [e.g. the NaI(Tl) detector] and the semiconductor detectors [e.g. Ge-Li, Si-Li and high purity germanium detectors]. For these detectors the interaction of gamma radiation with matter is used to differentiate individual radio nuclide. A gamma ray spectra emitted by a radionuclide is usually made up of photons, each group being monoenergetic. A detector can convert a given monoenergetic gamma-ray group into a well-defined photo peak with continuous components via the following processes: photoelectric effect; pair-production and compton effect. The ability of a detector to produce gamma-ray peaks from incident monoenergetic photons is characterized by the peak width and the peak efficiency. The width is commonly specified as the full width at half maximum [FWHM] or sometimes refer to as the resolution. The peak efficiency of the detector is the ratio of the number of counts in the peak corresponding to the absorption of all the photon energy (*i.e.*, in the full-energy peak) to

the number of photons of that energy emitted by the source. The choice of detectors in gamma spectrometry revolves around a balance between the peak efficiency and the energy resolution. The NaI(Tl) detectors have the advantage of high photo peak efficiency, but have poor resolution, while the Ge-Li detectors have an excellent resolution but poor efficiency (Knoll, 1979). The excellent resolution of the germanium detectors allows the separation of many closely spaced gamma lines, therefore germanium detectors are used when several radio nuclides are produced. An important factor that is fundamental in gamma-ray spectrometry is the efficiency curve of the detector. The set-ups of a 3"x 3" NaI(Tl) detector and that of a Ge-Li detector (45 cm^3 in volume) systems used for all gamma-ray spectrometry in this work are shown in Figures 2.6a and 2.6b respectively. Efficiency curves for the Ge-Li detector as a function of sample-detector distance are displayed in Figure 2.7.

The data for the total and peak efficiency curves of the flat surface NaI(Tl) detector shown in Figure 2.8 were measured by gamma-ray standard sources and fitted by the expressions given in equations 2.44 and 2.45 respectively.

$$\eta_T(E) = \exp[a_0 + a_1 \ln(E) + a_2 \ln(E)^2 + a_3 \ln(E)^3] \quad 2.44$$

$$\eta_P(E) = \exp[b_0 + b_1 \ln(E) + b_2 \ln(E)^2 + b_3 \ln(E)^3] \quad 2.45$$

where, $\eta_T(E)$ is the total efficiency as a function gamma-ray energy. The fitting coefficients for the total efficiency curve are:

$a_0 = -29.840$, $a_1 = 18.8962$, $a_2 = -3.869$ and $a_3 = 0.343$

and $\eta_p(E)$ is the photo-peak efficiency as a function of gamma-ray energy. The fitting coefficients for the photo-peak efficiency curve are:

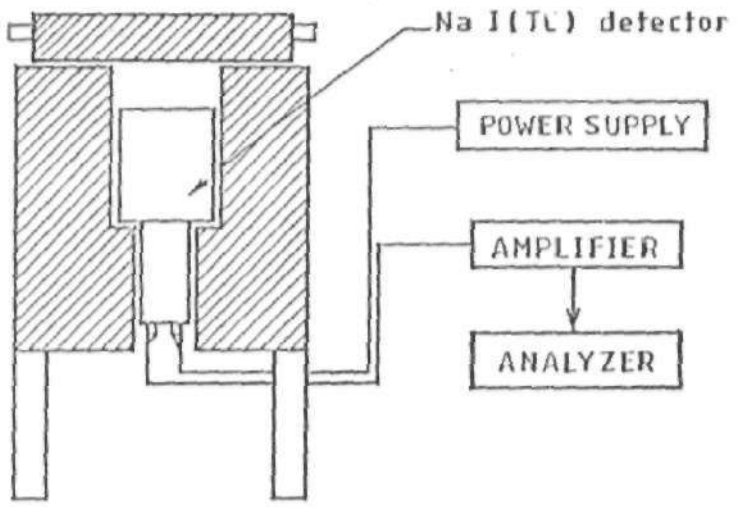
$b_0 = -84.643$, $b_1 = 56.947$, $b_2 = -13.426$, $b_3 = 1.380$

A survey of the main sources of corrections:

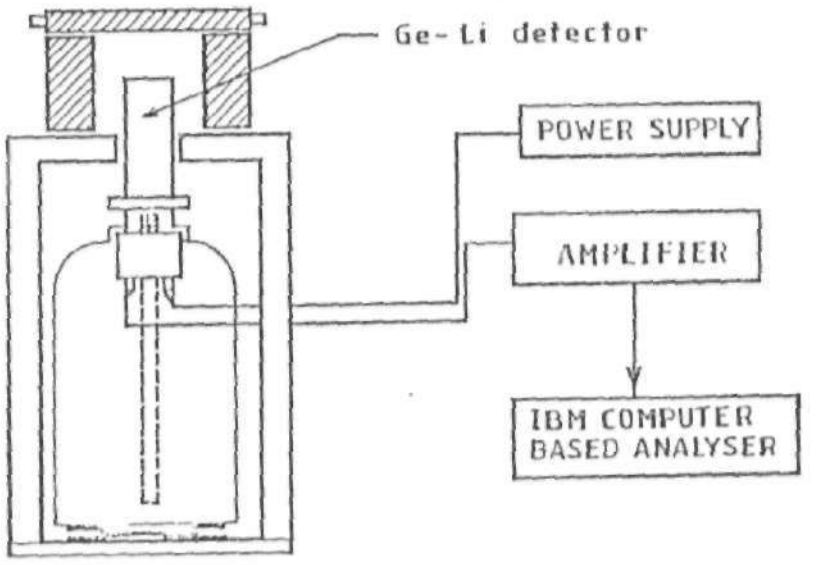
1) True coincidence losses: The true or cascade coincidence losses may occur when one or more gamma-rays are in cascade with the investigated gamma-ray within an interval of 10^{-7} s. In such cases, the detector is unable to differentiate the individual events hence the counts registered under the peak will be reduced. Correction to the measured peak area is determined from the expression below provided the decay scheme and the total efficiency of the gamma-ray are well known, (Daroczy and Raics, 1982).

$$\varepsilon_c = \frac{\sum_{i=1}^{n} \beta_i S_i \prod_{j=1}^{n_i} (1-\varepsilon_{i,j}) \gamma_{i,j}}{\sum_{i=1}^{n} \beta_i \prod_{j=1}^{n_i} \gamma_{i,j}} \qquad 2.46$$

where ε_c is the true coincidence correction and it is defined as the probability of detecting a given gamma-ray



(a)



(b)

Fig. 2.6 Geometrical setups of (a) the NaI(Tl) detector and (b) the Ge-Li detector systems used in this work

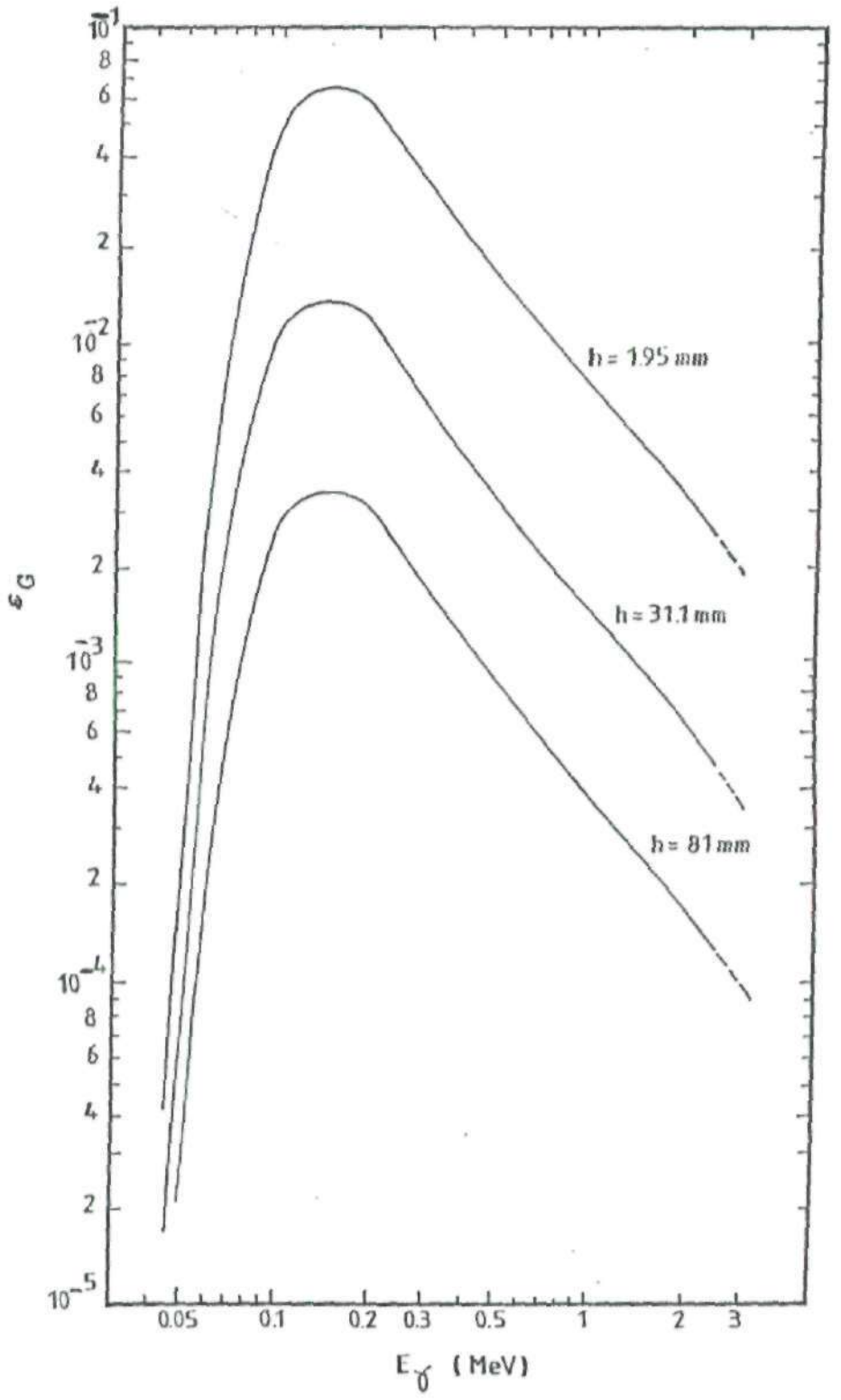


Fig. 2.7 Photo peak efficiency curves of the Ge-Li detector as a function of sample-source distance

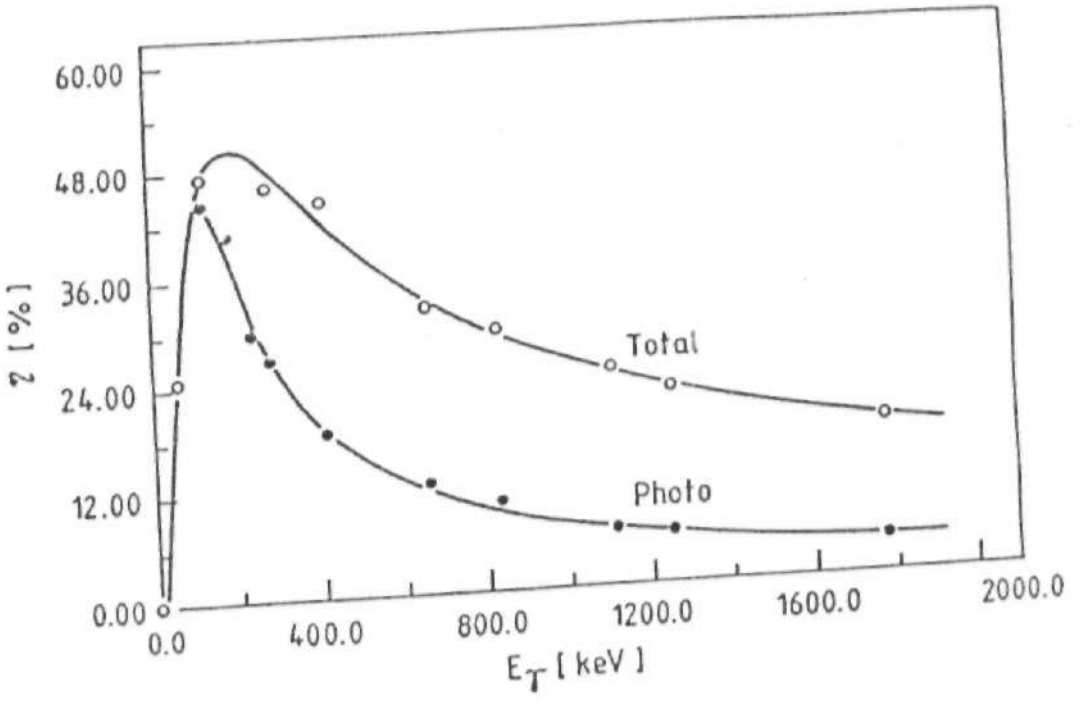


Fig. 2.8 Photo peak and total efficiency curves of the NaI(Tl) detector

quantum (γ_o) without the detection of any other from its cascade.

n_o is the number of cascade chains containing the measured γ_o n_i is the number of cascade gamma transitions in the i^{th} cascade chain excluding γ_o.

β_i is the branching ratio of the β^- (or β^+ , EC, α) transition populating the i^{th} energy level.

γ_{ij} is the branching ratio of the j^{th} gamma-transition in the i^{th} cascade chain.

$\varepsilon_{ij} = (\varepsilon_t \cdot \varepsilon_s)_{ij}$ is the product of the total detection efficiency and the self-absorption for the energy of the j^{th} gamma line and the i^{th} cascade chain.

$S_i = 1$ if the i^{th} chain is initiated by β^-, EC or α-decay.

$S_i = 1-2\varepsilon_{511}$ if the i^{th} chain is initiated by β^+ decay.

2) Dead time correction: The dead-time correction is defined as the ratio of the live time (T_l) to the real time (T_r). It is caused when the activity of the sample is high such that more than one gamma event arrives within the resolving time of the detector. In such a case, only one of the events will be processed and the others will be lost. Correction due to this factor can be effected by the following formula.

$$\varepsilon_d = T_l/T_r \qquad 2.47$$

3) If the activity is significantly high (*i.e.* $\varepsilon_d > 10\%$), then in addition to the dead-time correction the random

pile-up correction measurement may be needed. Random pile-up occurs when the two or more gamma-ray groups emitted from independent decay are detected simultaneously within the resolving time of the detector. Correction arising from this factor is effected by feeding a pulse of fixed frequency from a pulse generator into the pre-amplifier of the detector. The count rate of the all pulses in the spectrum including the pulse from the pulse generator will be affected by the pile-up of the investigated gamma-ray pulse. Consequently the random pile-up correction can be calculated by the formula below;

$$\varepsilon_p = \frac{P_s}{P_\circ} \qquad 2.48$$

where P_s and $P_\circ$ are the peak areas of pulser with and without sample respectively measured by the analyzer.

4) Correction due to time-variation in neutron flux: In activation analysis the number of radioactive nuclei denoted by N depends on a number of parameters as shown in the equation below

$$N = \frac{\sigma.n.\phi}{\lambda}[[1-\exp(-\lambda t_{irr})] \qquad 2.49$$

where, σ is the reaction cross section,

n is the number of nuclei in the sample,

λ is the decay constant,

t_{irr} is the irradiation time and

ϕ is the neutron flux which is taken to be constant during the irradiation.

Among the parameters above, time-variation of the neutron flux caused by instability in the operating parameters of the source can grossly affect the measured activity especially if the reaction under investigation has a half-life shorter than the irradiation time. The correction factor ε_f due to this effect can be determined by monitoring the neutron flux continuously with a BF_3 long-counter system. In practice, the neutron flux is proportional to the count rate, M/t_{irr}, where M is the total count recorded by the BF_3 counter during irradiation. In terms of the BF_3 counter where the flux is constant with time, equation 2.49 can be written as:

$$N = \frac{\sigma\, n\, \eta\, M}{\lambda\, t_{irr}} [1-\exp(-\lambda t_{irr})] \qquad 2.50$$

where, η is the efficiency of the BF_3 counter.

If for a fixed time interval Δt much shorter than the irradiation time during which the monitor count M_i can be assumed to be constant, then equation 2.50 becomes;

$$N = \frac{\sigma\, n\, \eta}{\lambda} \frac{[1-\exp(-\lambda\Delta t)]}{\Delta t} \sum_{i=1}^{n} M_i \exp-[\lambda(t_{irr} - i\Delta t)] \qquad 2.51$$

where the factor $\exp[-\lambda(t_{irr} - i\Delta t)$ gives the decrease in the number of nuclei produced in the i^{th} interval.

The correction factor ε_f is obtained by dividing equation 2.50 by equation 2.51. Thus, the expression below is obtained.

$$\varepsilon_f = \frac{\frac{M}{t_{irr}}[1-\exp(-\lambda\, t_{irr})]}{\frac{[1-\exp(-\lambda\Delta t)]}{\Delta t}\sum_{i=1}^{n} M_i \exp-[\lambda(t_{irr} - i\Delta t)]} \qquad 2.52$$

5) Self-absorption correction: This correction is caused by the absorption of the detected gamma-ray in the sample itself. Consider a sample of thickness d, with activity A_o and a cross sectional area of X shown in Figure 2.9.

If the density of the material of the sample is ρ then the activity dA in a thin layer dx will be given as follows.

$$dA = \rho\, X\, A\, dx_o \qquad 2.53$$

Due to the self absorption of gamma-ray, the measured activity dA_m will be less than the expected activity given in the equation below.

$$i.e. \qquad dA_m = dA \exp(-\mu x) \qquad 2.54$$

where μ is the linear absorption coefficient of the gamma-ray which depends on the gamma energy and sample material. From equations 2.53 and 2.54, the measured total

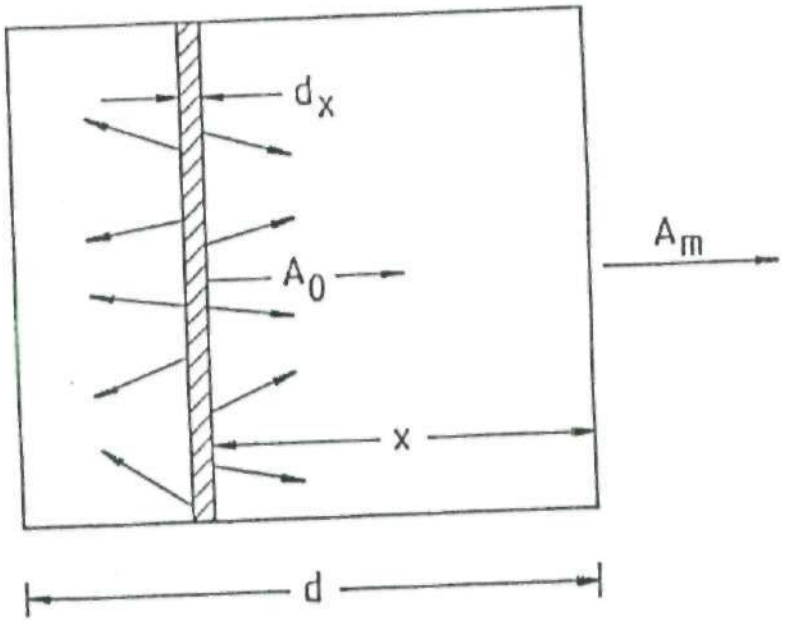


Fig. 2.9 Diagram for the self-absorption of gamma-ray in a sample

activity will be given as follows:

$$A_m = \int_0^d dA_m = \int_0^d \rho.X.A_\circ \exp(-\mu x)\, dx$$
$$= \rho\, X\, A_\circ \frac{[1-\exp(-\mu d)]}{\mu d} \qquad 2.55$$

Similarly from equation 2.53, the initial total activity A will be given as;

$$A = \rho\, X\, A_\circ\, d \qquad 2.56$$

The self-absorption correction ε_a which is defined as the ratio of measured activity to the emitted activity (*i.e.* A_m/A) is given by the expression below.

$$\varepsilon_a = \frac{[1 - \exp(-\mu d)]}{\mu d} \qquad 2.57$$

where d is the thickness in gcm^{-2} and μ is the absorption coefficient in cm^2g^{-1}.

2.4.2 The thermal neutron reflection technique

General principles: In general, neutrons produce by a laboratory neutron source have energies far above the thermal region. When fast neutrons collide with the nuclei of a medium, the neutrons begin to lose their kinetic energy through elastic and inelastic processes until they have velocities in equilibrium with the velocities of the atoms in the medium (Curtiss, 1959). Under practical

conditions, some neutrons will be lost through the capture process while others may escape through the boundaries of the finite medium thereby giving rise to thermal neutrons. The escape of thermalized neutrons can be as result of transmission through the boundary of the medium or via reflection from the nuclei of the medium. However the intensity of thermal neutrons leaving the medium depends on the slowing-down process which in turn depends on the nuclei of the medium. As discussed earlier on in this chapter, in the moderation of fast neutrons, the elastic process is by far the most dominant mode of interaction in which the kinetic energy of the colliding neutron is practically transferred to the target nuclei.

The average energy loss per collision is given as;

$$\overline{\Delta E} = E_1 \frac{1-\alpha}{2} \qquad 2.58$$

where, $\overline{\Delta E}$ is the mean energy loss per collision.

E_1 is the energy of the incident neutron.

$$\alpha^2 = \frac{A-1}{A+1} \qquad 2.59$$

where, A is the mass number of the nuclei.

As can be seen from equations 2.58 and 2.59 the intensity of thermal neutrons strongly depends on the mass number of the medium. Therefore in this regard hydrogen which has a mass number of 1 has a significant role to play in the slowing-down of fast neutrons. Consequently, nuclear

techniques based on physical parameters of neutrons such as moderation and reflections are widely used in the analysis of bulk media mainly for the determination of hydrogen or moisture content. The thermal neutron reflection technique which was developed for the determination of bitumen content in asphalt concrete (Buczko *et al.*, 1975) is based on the same principle. Subsequently, the experimental arrangement the "*BITATRON*" designed for this purpose has been used for related investigations.

The experimental arrangement: The scheme of the experimental set-up which was manufactured for a road construction company but was modified for this work is shown in Figure 2.10.

It consists of a 18.5 GBq. Pu-Be isotopic neutron source embedded in a polyethylene block 30 cm in diameter. The advantages of the Pu-Be source include the fact it does not emit penetrating gamma radiations and its long half-life. The extended polyethylene serves as the slowing-down medium and provides the necessary shielding against fast neutrons. In order to minimize the effect of background neutrons from the shield, the sample is covered with cadmium sheet except the side facing the sample. A proportional counter filled with $^{10}BF_3$ gas and having a sensitive length of 80 mm and a diameter of 20 mm is placed at the semi-infinite surface between the source and sample.

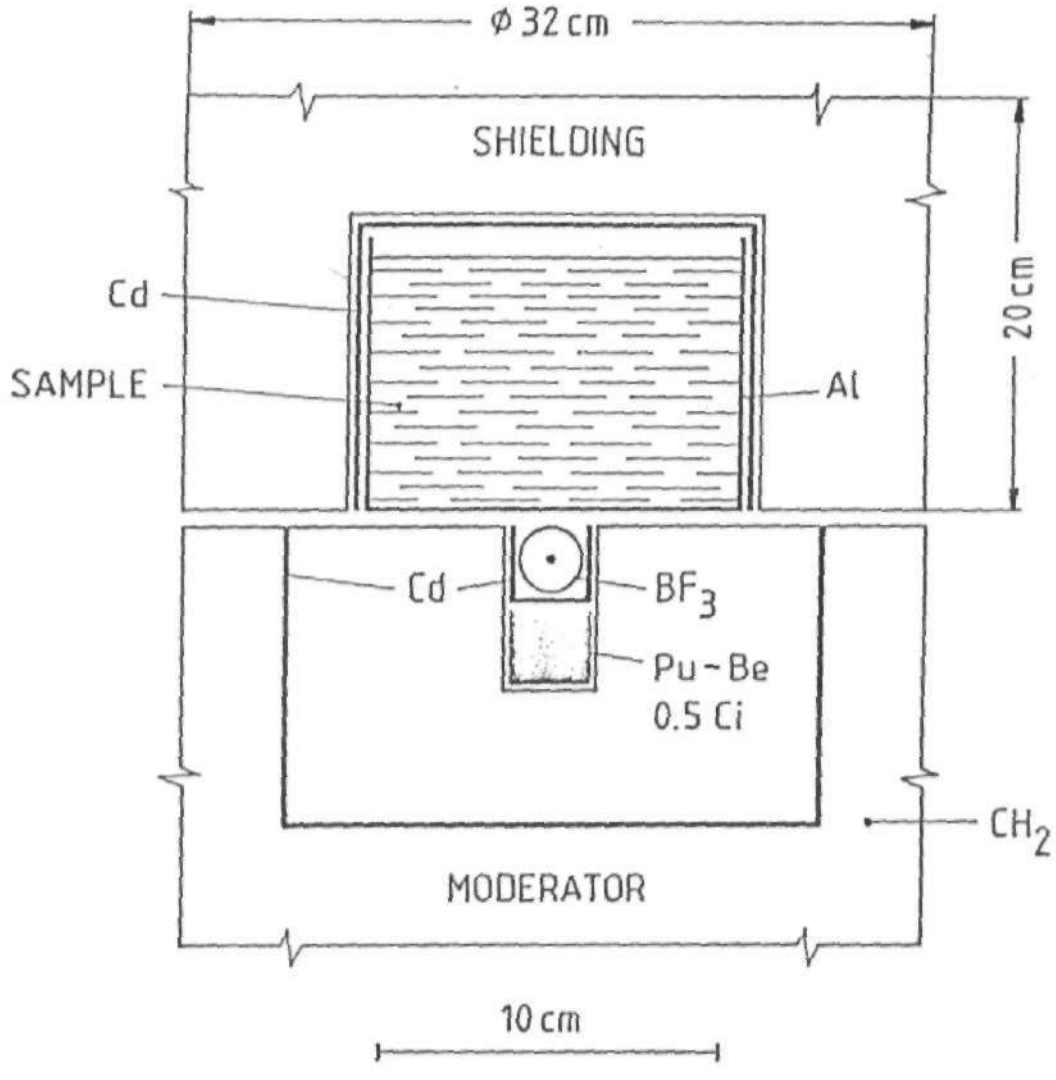


Fig. 2.10 An improved experimental setup for the determination of H and O+C/H in oil samples based on neutron reflection technique

The counter which is connected to a pre-amplifier and an amplifier is fed from a high voltage power. The output of the amplifier is connected to a single channel analyzer having a timing and a scaling stages. A printer is interphased with the timing and scaling stage so as to enable the detected number of counts to be recorded and printed for a fixed time interval. The relative excess count η, normalized to the physical density ρ, can be determined using the expression below.

$$\eta = (I - I_{\circ})/\rho\, I_{\circ} \qquad 2.60$$

where, I and $I_{\circ}$ are the count rate measured with and without the sample respectively.

Organic materials having well-known hydrogen content are used to plot a calibration curve since the excess count rate η for a given sample depends linearly on its hydrogen content. From the calibration curve, total hydrogen content in the investigated sample can be determined.

2.4.3 The pulse height response spectrometry technique

The pulse height response spectrometry system (PHRS) is an arrangement for the measurement of neutron spectra based on the elastic scattering process of neutrons with hydrogen. It consists of an organic scintillator detector coupled to a photo multiplier tube and appropriate electronic modules. The system first came into use as a

neutron spectrometer as far back as 1960 (Knoll, 1979). In comparison with the time-of-flight spectrometer, it is compact and represents a good compromise between counting efficiency and energy resolution. Consequently, the system can be used for on-line checking of the source spectrum and for the measurement of leakage spectra behind samples of thickness of up to 2 m.

Properties and principles of the system: The neutron detector, usually an organic scintillator uses the principle of elastic scattering on light nuclei to generate a pulse height spectrum. This is achieved through the detection of recoil-protons produced when fast neutrons collide with hydrogen nuclei. Since the gamma-rays produced are also detected through compton-electron recoil process, a detector consisting of an NE-213 stilbene scintillator is preferred because it can discriminate gammas from neutrons. The scintillation response produced by a gamma-ray due to the ionization of electrons is faster than that due to proton ionization because electrons are lighter. A pulse-shape discriminator can be employed to distinguish scintillation pulses according to neutron events or gamma events. The main components of the organic scintillator are hydrogen, carbon and little amount of oxygen. When an incoming neutron of energy E_n is incident on the organic scintillator, a recoil-proton of average energy E_p is produced from the elastic scattering of neutron with hydrogen. From the kinematics of neutron elastic scattering

(section 2.2.2), the relationship between the average energy of recoil-protons and that of the incoming neutron in the centre-of-mass (CM) system given as:

$$E_p = 1/2\ (1-\cos\theta)\ E_n \qquad 2.61$$

where, θ is the scattering in the CM system.

It is well-known that hydrogen is by far the most dominant element in neutron elastic scattering and since all scattering angles in the centre-of-mass system are possible, the energy spectrum of the recoil-proton should be rectangular. However, due to edge effect, multiple scattering from hydrogen and carbon as well as non-linear behaviour of organic scintillator, the response spectrum is distorted. Energy calibration of the detector is performed by the compton distribution from ^{22}Na gamma-ray standard. The channel number corresponding to half-height of the compton peak is associated with the maximum energy of compton distribution. Then, the neutron spectrum is obtained by de-convolution of the pulse height response spectrum using an unfolding code containing the parameters of the detector and the channel number corresponding to half-height of the compton peak.

The pulse height response spectrometer: A block diagram of the system used in this work is shown in Figure 2.11. It consists of an NE-213 stilbene liquid scintillator detector of volume 98 cm^3 connected to a photo multiplier tube and

fed from a high voltage power supply of 1.16 kV. The output of a preamplifier connected to the photo multiplier tube is fed into the input of a delay-line amplifier. The delay-line amplifier accepts input of either polarity from the preamplifier and amplifies the pulses by an adjusted gain factor. As a result of amplification, two output pulses are produced from each input pulse. One is positive UNI-polar (UNI) and the other is BI-polar (BI). For energy measurements, the UNI-polar output is preferred because it has low signal-to-noise ratio. The pulse-shape analyzer is used to discriminate the UNI-polar output pulses by the "rise-time discrimination" method as a result of which the pulse height response spectrum can be fed into the an MCA via a linear gate stretcher.

When the gate is opened linear pulses which are stretched in duration pass through without distortion but while closed, all pulses are blocked. The time-to-amplitude converter is desirable to obtain rise-time spectra for both neutron events and gamma events. The rise-time spectrum for both neutrons and gammas and the rise-time spectrum after the elimination of gamma events obtained with this system are displayed in Figures 2.12a and 2.12b respectively.

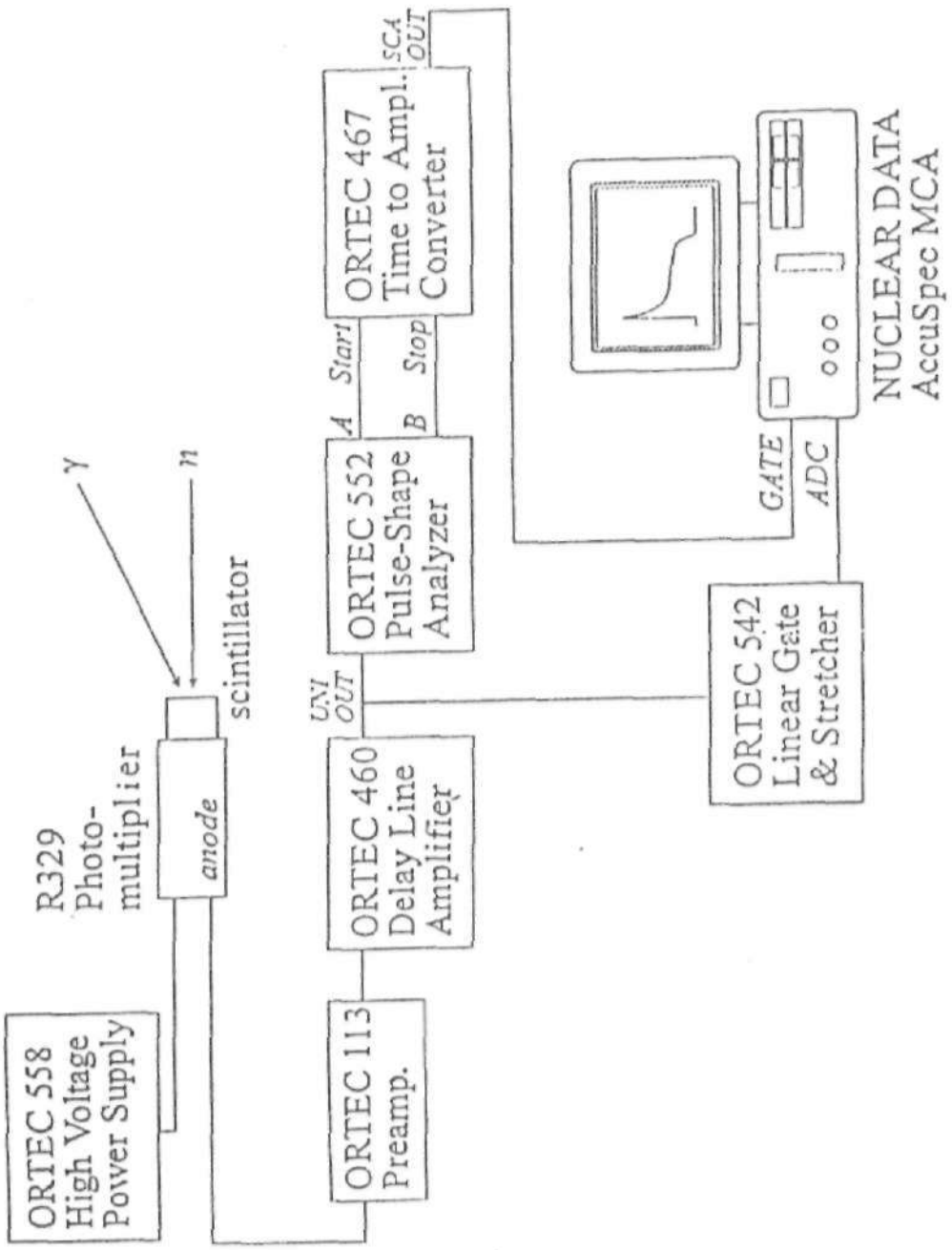
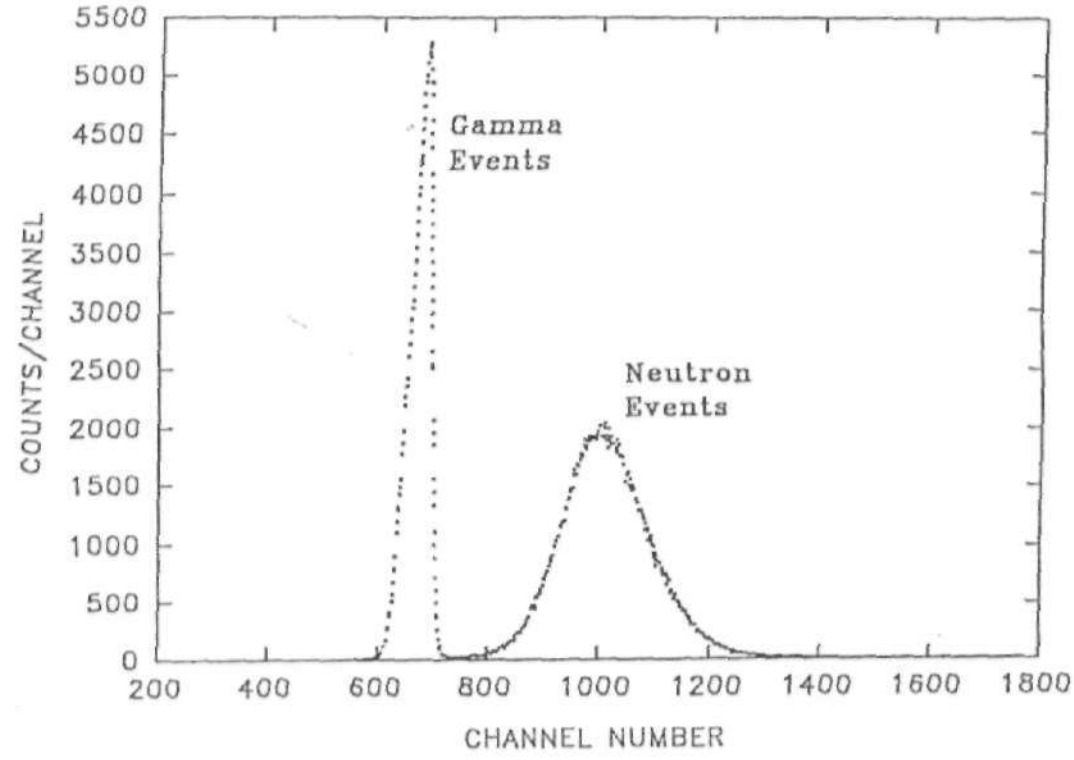
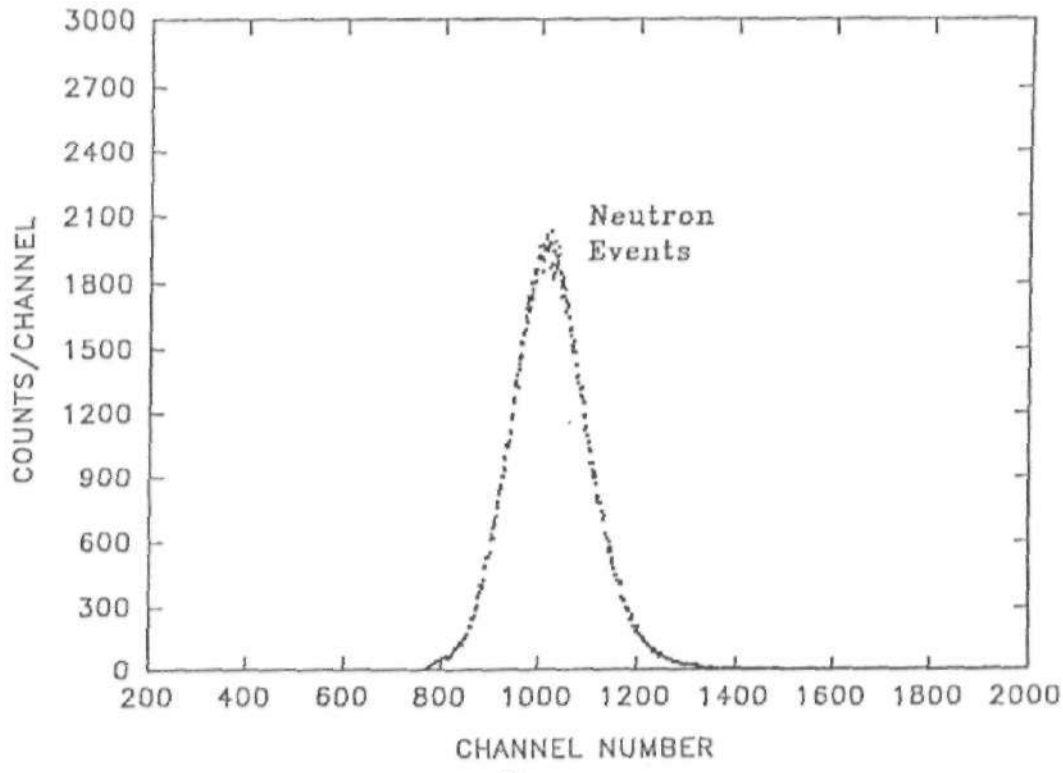


Fig. 2.11 A block diagram of the PHRS system



(a)



(b)

Fig. 2.12 Rise-time-spectra of (a) neutron and gamma events and (b) after the elimination of gamma events

CHAPTER THREE

3.0 CHARACTERIZATION OF NEUTRON FIELDS

In general neutron fields are characterized by the following parameters; the mean energy, angular yield and energy distributions of neutrons as well as the neutron flux density distributions. An accurate knowledge of these parameters is required for precise measurements of differential and integral neutron data. Measurements of neutron cross section curves from threshold to 20 MeV are carried out with accelerator-based neutron sources. In most accelerators, the beam components are separated according to their masses by a magnetic analyzer which must be calibrated using nuclear reactions having well known resonance and threshold energies. A review of the main characteristics of recommended resonance reactions indicates that there is only one calibration point at $E_p \leq$ 200 KeV (Marion, 1966). In the case of neutron generators for which the energy of bombarding deuteron beam is usually less than 500 keV, empirical formulae for calculating angular distributions of the yield and energy of neutrons have been given (Csikai *et al.*, 1986). Nevertheless, due to instability in neutron generator operating parameters and target conditions, the flux and the energy of neutrons must be determined during irradiations.

Similarly, it is well known that the spectral distribution of neutrons produced via the $^{2}H(d,n)^{3}He$ reaction at $E_d \geq 4.5$ MeV is quasi-monoenergetic and it is caused mainly by the contamination from breakup neutrons. The degree of contamination depends on the incident deuteron energy and the material of the gas target (Cabral *et al.*, 1990; Gallert *et al.*, 1993: Gallert *et al.*, 1994). Consequently, the characteristics of neutrons produced by the 14 MeV neutron generator and the variable-energy cyclotron used were determined. The experimental techniques employed as well as the results obtained are described below.

3.1 Energy Calibration of Low-voltage Accelerator by $^{11}B(p,\gamma)^{12}C$ Reaction

3.1.1 Introduction

The determination of nuclear reaction rates at low beam energies requires a knowledge of the beam energy to a high precision (Freye *et al.*, 1977). The energy and the yield of neutrons produced in the $^{2}H(d,n)^{3}He$ and $^{3}H(d,n)^{4}He$ reactions depend on the bombarding beam energy and the angle of emission. The absolute energy of the accelerated beam can be measured by direct and indirect methods. The direct method has a limitation because static voltmeters are available up to 100 kV with an accuracy of ±1 kV. Among the indirect methods the use of resonant and non resonant

nuclear reactions for calibrations of low-energy accelerators are the most reliable (Csikai, 1987). Furthermore, the current of the magnetic analyzer used as a relative tool must also be calibrated for beam energy using nuclear reactions. In this work, the current of the magnetic analyzer of a low-current neutron generator used for cross section measurements was calibrated for beam energy by observing the resonance in the $^{11}B(p,\gamma)^{12}C$ reaction.

3.1.2 Experimental procedures

The low-current neutron generator used for activation cross section measurements has a 100-200 kV variable high voltage power supply tube and a radio-frequency (RF) ion source for producing ion beams. The discharge vessel of the RF ion source is made of pyrex glass and the gas is ionized by means of an oscillator operating within a frequency range of 15-100 MHz with a power consumption of 100-400 W. The ions from the plasma are extracted by applying a voltage of about 5 kV inside the discharge balloon. The ions leaving the discharge balloon are introduced into an accelerating and a focusing electric field provided by the ion optical accelerating systems located inside the tube. The accelerated ion beam has an energy equivalent to the potential drop across the high voltage terminal and the ground. A magnetic analyzer operating with a current of about 1.8 A is used to deflect the protons from the mixed

beam while the quadropole lenses are used to focus the magnetically analyzed beam onto the target. The target is a pellet of 19 mm diameter made from amorphous boron powder by an hydraulic pressing machine having a pressure of about 100 bar and was mounted in a target holder at 90° with respect to the beam direction. Direct cooling was applied to the target via a jet of LN_2 supply. The γ-ray emitted at 0° relative to the direction of the beam was detected by a NaI(Tl) scintillation detector which was connected to a compatible computer-based multi channel analyzer. A schematic diagram of the measuring arrangement is shown in Figure 3.1.

3.1.3 Results and discussion

Energy calibration of the NaI(Tl) detector was performed by γ-ray lines from by a set of standard sources. The proton induced resonance was observed by measuring the intensity of the emitted γ-rays at 4441.4 keV as a function of the accelerating voltage. The terminal voltage was controlled by measuring the current through a bank of resistors. The measured data are given in Table 3.1.

A plot of the gamma intensity as a function of terminal voltage is shown in Figure 3.2. In order to reduce the contributions of room background the detector was placed inside a cylindrical lead shield.

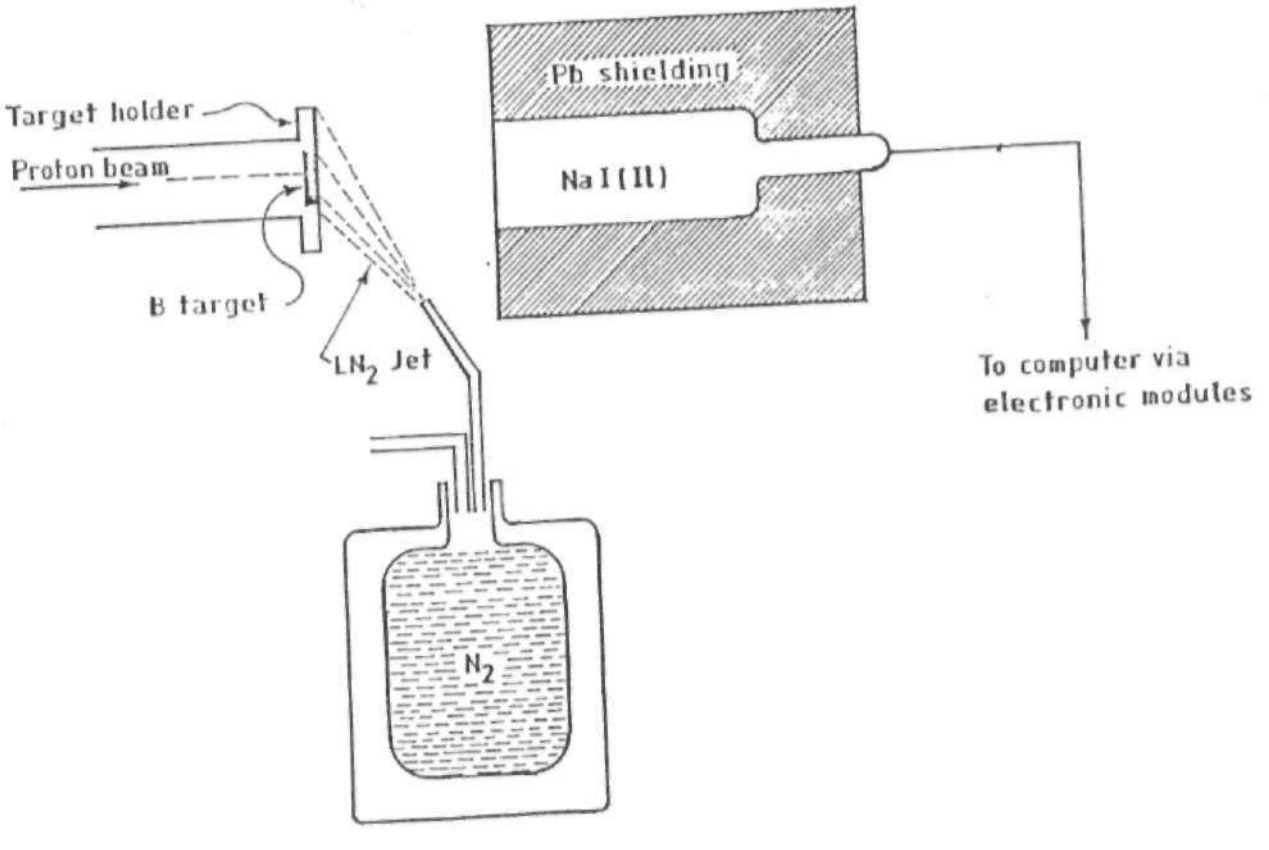


Fig. 3.1 Schematic diagram of the experimental arrangement used for the energy calibration of low-voltage accelerator

Table 3.1 Intensity of proton-induced γ-ray as a function of terminal voltage.

Terminal voltage (kV)	Ion current (μA)	Magnetic current (A)	Intensity (c.p.s.)
130.0	50.0	1.80	0.0
150.0	50.0	1.78	0.0
160.0	50.0	1.78	58.9
165.0	50.0	1.78	140.3
170.0	50.0	1.78	172.7
180.0	50.0	1.78	180.5

The energy spread of the proton beam was determined from the 75% and 25 % points of the high-energy edge of the gamma yield.

Furthermore, the resonance beam energy was deduced from the inflection point of the curve shown in Figure 3.2 after a least square fitting of the measured data. The terminal voltage was calibrated for energy by accepting a value of 163.5 keV at the resonance. The results obtained reveals a width (FWHM) of 5.5 ± 0.4 keV at a resonance of 163.5 keV.

3.2 Angular Energy Distribution of D-T Neutrons Produced by a Neutron Generator

3.2.1 Introduction

The total yield of neutrons emitted in all directions by a neutron generator is proportional to the number of charged particles bombarding the target (*i.e.* the beam

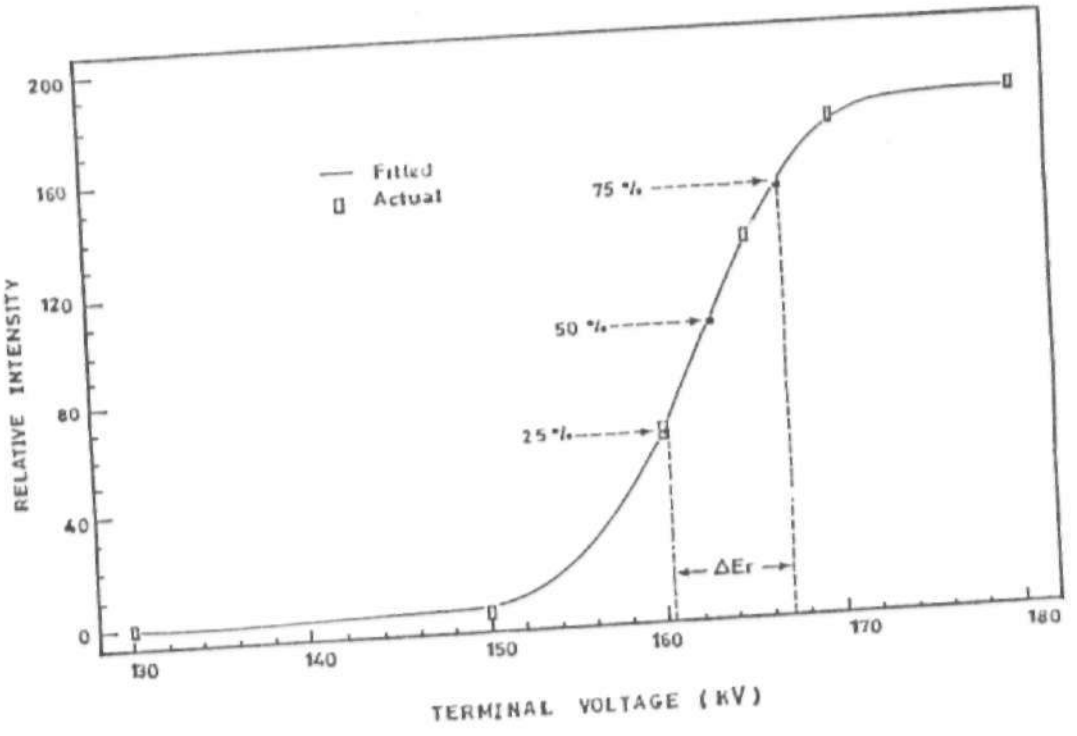


Fig. 3.2 Intensity of proton-induced gamma-ray versus terminal voltage

current). However the energy and relative yield of emitted neutrons depends on the type of nuclear reaction producing the neutrons, the energy of the bombarding particles and the angle of emission of the neutrons relative to the direction of the bombarding beam. Therefore, the angular energy distribution of emitted neutrons must be determined especially for precise measurements of neutron activation cross sections. In this work, irradiations with 13-15 MeV neutrons were performed at a low-current D-T neutron generator. The average neutron energy at a given angle of emission was determined from the measured cross section of $^{90}Zr(n,2n)^{89}Zr$ reaction, while the neutron flux was monitored by the $^{93}Nb(n,2n)^{92m}Nb$ reaction. The experiment is based on the fact that the (n,2n) cross section of zirconium varies rapidly as a function of neutron energy around 14 MeV while the (n,2n) cross section of niobium as function of neutron energy shows negligible variation in the same energy region. The advantage of this method is that the energy monitors (Zr and Nb foils) can be irradiated together with the samples under investigation in a stack. It has been shown that the energy of neutrons as a function of emission angle can be calculated by the following formula (Csikai *et al.*, 1986).

$$E_n(E_d,\theta) = E_o + \sum_{i=1}^{n} E_i \cos^i\theta \qquad 3.1$$

where E_n is the neutron energy in MeV.

E_d is the deuteron energy in keV.

θ is the emission angle.

E_o and E_i are coefficients for different deuteron energies and are summarized in Table 3.2.

Table 3.2 Values of parameters in equation 3.1 for the calculation of angular dependence of neutron energy.

E_d (keV)	D-T Reaction (MeV)		
	E_o	E_1	E_2
50	14.06520	0.42329	0.00682
100	14.07883	0.57613	0.01222
150	14.08942	0.66776	0.01600
200	14.09680	0.72427	0.01908
250	14.10286	0.76661	0.02167
300	14.10803	0.80001	0.02374
325	14.10723	0.79477	0.02347

3.2.2 Experimental procedures

Irradiation: High-purity rectangular-shaped metallic samples of Zr and Nb having dimension of 15 x 10 x 1mm were irradiated with fast neutrons of energies between 13 and 15 MeV produced via the $^{3}H(d,n)^{4}He$ reaction using an analyzed deuteron beam of 190 keV. In order to reduce the number of scattered neutrons from the target holder of the generator, an 0.3 mm thick air-jet cooled aluminum backed titanium-tritium target was used in a scattering-free arrangement shown in Figure 3.3. The Zr samples and the

corresponding Nb flux monitoring foils were fastened back-to-back round an aluminum ring of 20cm diameter with the beam spot of 0.5 cm diameter at the centre. The samples and the corresponding flux monitors were placed at 0°, 40°, 90°,110° and 150° relative to the direction of the deuteron beam. A BF_3 counter was used to monitor the time-variation of the neutron flux during the 5 hours irradiation.

Activity measurements: The gamma-ray activities of irradiated zirconium samples and those of niobium flux monitors were measured by a Ge-Li detector system described in chapter 2. Total error of the full-energy-peak efficiency in the region between 180 keV and 1500 keV has been found to be 1.0%. Activities of each of the zirconium samples were measured via the 909 keV gamma-line after 24 hours cooling time. Immediately after which the activities of each of the niobium foils were also measured via the 934.5 keV gamma-line. The nuclear data used in this measurement are given below in Table 3.3

Table 3.3 Nuclear data of the energy and flux monitor reactions

Radionuclide	E_γ (keV)	Half-life	I_γ (%)	η (%)
^{89}Zr	909.2	3.27 d	99.0	0.87
^{92m}Nb	934.5	10.15 d	99.1	0.85

Nuclear data taken from Reus and Westmeier (1983)

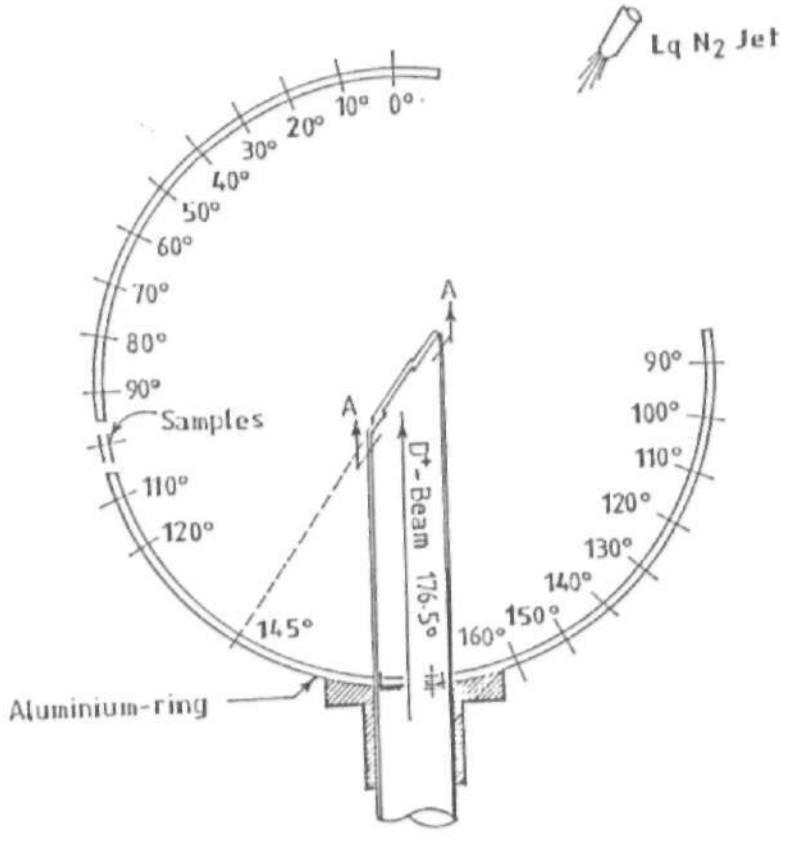


Fig. 3.3 Scattering-free geometry for cross section measurements

The cross section of $^{90}Zr(n,2n)^{89}Zr$ reaction as a function angle was calculated based on equation 2.4.10 using the ASEASY computer code. Similarly, the neutron flux at each sample position was monitored by the $^{93}Nb(n,2n)^{92m}Nb$ reaction for which a value 460 ± 5 mb was accepted as the cross section value taken from Csikai *et al.* (1991). The gamma ray counts were corrected for the effects of variation of neutron flux with time during the irradiation, true coincidence, dead-time, gamma-ray self-absorption and detector efficiency.

3.2.3 Results and discussion

Results of the cross section as a function of angle obtained in this experiment are summarized in Table 3.4. The uncertainties given for the measured cross sections arise mainly from the neutron flux determination. It has been shown by Csikai *et al.*, (1991) that the (n,2n) cross section of zirconium depends on neutron energy in the 14 MeV region and can be well approximated by a second order polynomial given in equation 3.2

$$\sigma(E_n) = \sum_{i=0}^{2} a_i . E_n^i \qquad 3.2$$

where, $a_o = -13244.5$ mb

$a_1 = 1668.16$ mb/MeV

$a_2 = -48.543$ mb/(MeV)^2

Table 3.4 Measured cross sections of $^{90}Zr(n,2n)^{89}Zr$ reaction at different emission angles.

Angle	Neutron Flux (n/sq.cm.s)	Cross-section $\sigma(\theta)$ (mb)	Uncertainty $\Delta\sigma(\theta)$ (mb)
0°	1117000	753.90	± 25.20
40°	1115000	673.60	± 22.60
90°	1056000	567.80	± 18.90
110°	933000	560.30	± 18.70
150°	989000	357.50	± 13.10

From the above expression the neutron energy at each angle of emission was calculated by accepting that the cross section as a function of emission angle equals the cross section as a function of energy (*i.e.* $\sigma(E_n) = \sigma(\theta)$. Results obtained are stated in column 2 of Table 3.5. Column 3 of this Table contains the results obtained based on the empirical formula (equation 3.2). As can be seen, slight deviations exist between the measured and the calculated neutron energies which may be attributed to the target conditions.

Table 3.5 Deduced and calculated mean energy of neutrons as a function emission angle

Angle	Neutron energy (MeV)	
	measured	calculated
0°	14.58 ± 0.25	14.77
40°	14.30 ± 0.24	14.61
90°	13.91 ± 0.23	14.09
110°	13.88 ± 0.23	13.86
150°	13.30 ± 0.22	13.52

3.3 Spectral Distribution of D-D Neutrons Produced by an MGC-20 Cyclotron

3.3.1 Introduction

The compact MGC-20 cyclotron described in chapter 2 is regularly used as a neutron source to produce neutrons via D-D reactions for the investigation activation cross section curves from 5 to 13 MeV. Like all D-D neutron sources where gas cells are used, the neutron spectrum is often contaminated by neutrons from secondary sources. The secondary neutrons are due to the following processes: (1) Break-up of deuterons at $E_d \geq 4.5$ MeV caused by "stripping" when fast moving deuterons strike a target nucleus; (2) Break-up of deuterons in the Coulomb electrostatic fields of construction materials *i.e.* X(d,np)X process; (3) Self-target build up in the beam stop *i.e.* D(d,n) process; (4) Production of neutrons as a result of the interactions of deuterons with the beam stop and the entrance window *i.e.* X(d,xn)Y process and (5) Production of neutrons via D(d,2n)2p process at $E_d \geq 8.9$ MeV. At 0° angle of emission, the contributions due to the first three processes have been shown to be significant (Drosg and Schwerer, 1987). Recently, an improved D_2 gas cell system which eliminates the gas-out runs method of estimating the degree of contamination has been developed (Gallert *et al.*, 1994). However, the contributions of secondary neutrons to the signal-to-background ratio (S/B) at a given neutron source

comes from the break-up processes and must be determined. In this respect, the energy spectra of neutrons produced at the cyclotron by deuteron of energy between 4 and 10 MeV were measured by the PHRS system. For comparison, the activation unfolding technique in combination with the SULSA computer code (Sudar, 1985) were used to determine the neutron spectrum at E_d = 8.0 MeV.

3.3.2 Experimental procedures

Irradiation: Neutrons of average energies ranging from 5 to 13 MeV were produced by the variable-energy MGC-20 cyclotron. The energies of the analyzed deuteron beam which can be determined by the formula expressed in equation 3.3:

$$E_d = K.A.\nu^2/(1 + \frac{K.A.\nu^2}{2.E_o}) \qquad 3.3$$

where, ν is the NMR frequency, and K is a characteristic parameter of the cyclotron, for this cyclotron K = 26.453 ± 0.052 keV/(MHz)^2 (Jozsa *et al.*, 1988).
A and E_o are parameters related to the accelerated ions, for deuterium ions, A = 0.05002482 and E_o = 1.875628 x 10^6 MeV. Some parameters of the beam at the different bombarding energies are summarized in Table 3.6.

A simple polynomial expression (equations 3.4) is given for estimating the energy loss in the window of the gas cell for 3 MeV ≥ E_d ≤ 12 MeV is obtained from the solid line displayed in Figure 3.4.

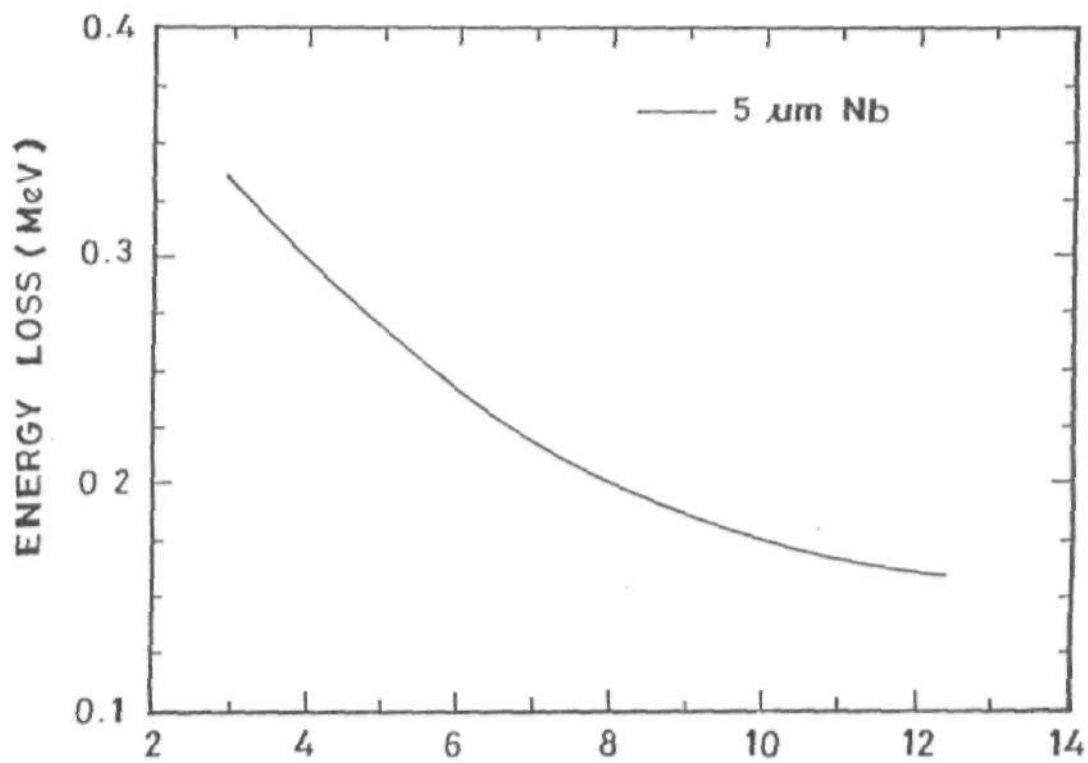


Fig. 3.4 Beam energy loss in the entrance window of a D_2 gas cell as a function of the incident beam energy

$$\Delta E_w = a_o + a_1 . E_d + a_2 . E_d^2 \qquad 3.4$$

where, $a_o = 0.4547$

$a_1 = -0.04705$

$a_2 = 0.00188$

Table 3.6 Energy data of deuteron beam used for the production of neutrons at the cyclotron.

ν_{NMR} (MHz)	E_d(in) (MeV)	E_d(out) (MeV)	Energy loss ΔE (MeV)
17.386	4.00	3.713	0.297
21.000	5.820	5.575	0.245
22.932	6.946	6.729	0.217
23.580	7.343	7.132	0.211
24.910	8.193	7.997	0.196
26.824	9.497	9.319	0.178
27.144	9.724	9.550	0.174

A schematic diagram of the experimental arrangement shown in Figure 3.5. consists of a D_2 gas target, sample holder and the NE 213 detector. The gas target is a 40 mm long cell filled with D_2 gas at 1.8 bar and covered by 5 μm Nb and 8 μm W foils as aperture and beam stop respectively.

The spectra of neutrons produced at the different bombarding energies were measured by the neutron spectrometer kept at 0° with respect to the beam direction. In order to avoid pile-up of pulses in the detector, a low beam current (< 10 nA) was applied for 30 minutes preceding

the irradiation of the foils whose activation cross section are being measured. Thereafter, a beam current of 3 μA was applied for the cross section investigation.

As a check of this method the neutron spectrum at E_d= 8.0 MeV was determined by the activation unfolding technique. In this respect, threshold energy monitor foils were irradiated together with the investigated samples in a stack. Nuclear data of the threshold energy reactions accepted for this purpose are presented in Table 3.7.

Table 3.7 Nuclear data of threshold energy monitors

Reaction	Half-life	E_γ (keV)	E_{thr} (MeV)	I_γ (%)
$^{115}In(n,n')^{115m}In$	4.49 h	336.2	0.8	45.91
$^{27}Al(n,\alpha)^{24}Na$	15.03 h	1368.5	6.5	100.0
$^{56}Fe(n,p)^{56}Mn$	2.58 h	846.8	5.5	98.87
$^{48}Ti(n,p)^{48}Sc$	43.7 h	983.5	7.0	100.0
		1037.5		97.5
		1312.1		100.0
$^{59}Co(n,\alpha)^{56}Mn$	2.58 h	846.8	6.5	98.87
$^{58}Ni(n,p)^{58}Co$	70.78 d	810.8	2.0	99.44
$^{93}Nb(n,2n)^{92m}Nb$	10.15 d	943.5	9.7	100.0
$^{197}Au(n,2n)^{196}Au$	6.18 d	355.7	8.8	87.0

Data evaluation and analysis: The proton spectra measured by the neutron specrometry system are unfolded by a computer code (Olah, 1994) and are stored in binary files.

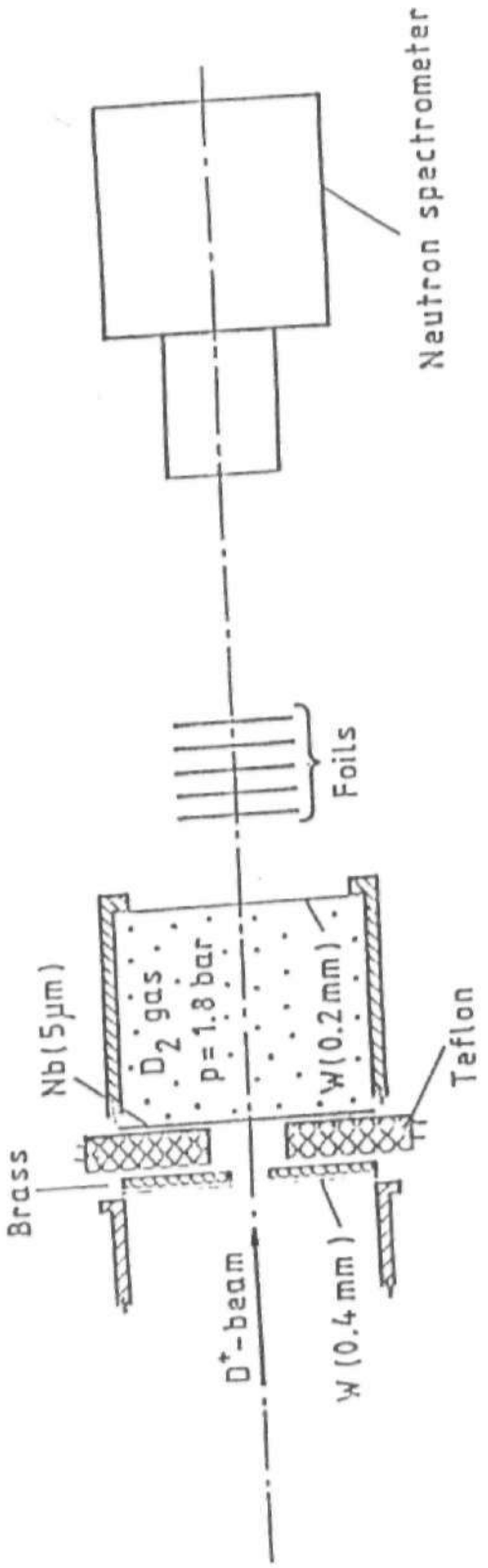


Fig. 3.5 Schematic scheme of the experimental arrangement at the cyclotron

The stored data are converted from binary to ASCII files and are evaluated by the ASEASY computer code to obtain the neutron flux density as a function of neutron energy [ϕ(E)]. The values of ϕ(E) are plotted against the corresponding neutron energy by the PLOT40 computer code. Neutron spectra corresponding to E_d = 3.87 MeV and E_d = 9.39 MeV measured by the PHRS system are displayed in Figure 3.6.

In the case of activation unfolding technique, the neutron spectra were determined from measured specific activities of the irradiated detector foils by the SULSA computer soft-ware. For this reason, the activities of the energy monitor reactions were measured by the Ge-Li detector system described in section 2.3.1 and corrections for the effects of true coincidence, gamma-ray self-absorption, detector efficiency and neutron flux variation with time were made to the calculated sample activities. The specific activities obtained for the monitor reactions together with the uncertainties in percentage which are the input of SULSA code are stated in Table 3.8.

The SULSA code determines the neutron spectrum from an iterative solution of generalized least square method without an input spectrum. The cross section data belonging to the monitor reactions as well as the corresponding covariance matrices used with this code are taken from the IRDF-90 (1990) nuclear data file.

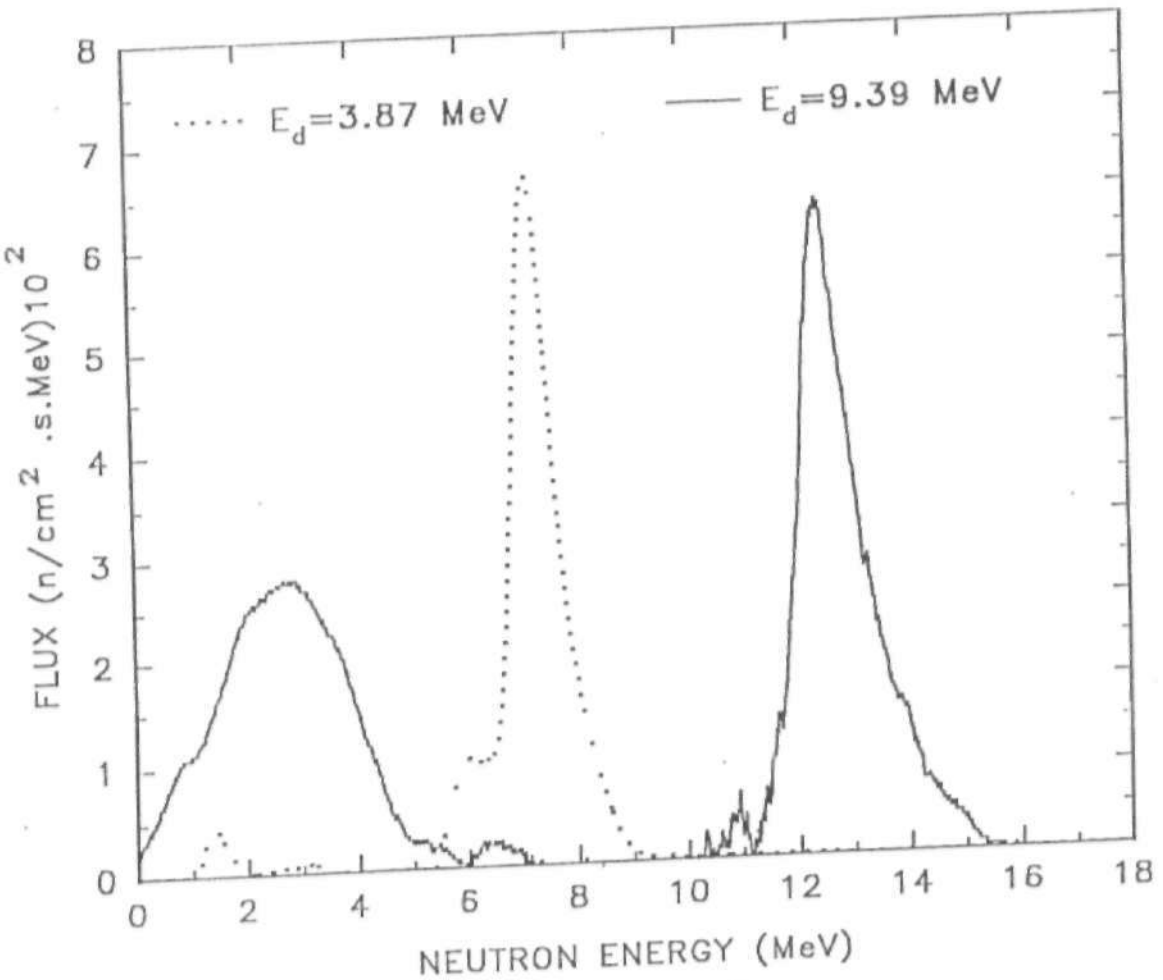


Fig. 3.6 Measured spectra of neutrons produced with deuteron beam of 3.87 and 9.39 MeV energies

Table 3.8 Measured specific activities of the energy monitors

Monitor reaction	Specific activity 10^{-19} (cps)	Uncertainty (%)
$^{48}Ti(n,p)^{48}Sc$	9.630	2.755
$^{56}Fe(n,p)^{56}Mn$	12.245	2.486
$^{59}Co(n,\alpha)^{56}Mn$	2.632	3.240
$^{58}Ni(n,p)^{58}Co$	88.527	2.470
$^{93}Nb(n,2n)^{92m}Nb$	10.675	2.517
$^{115}In(n,n')^{115m}In$	107.257	1.444
$^{197}Au(n,2n)^{197}Au$	142.608	1.511
$^{27}Al(n,\alpha)^{24}Na$	14.132	2.595

Figure 3.7 shows the neutron spectra obtained by this method at E_d = 8.0 MeV together with that obtained by the PHRS at the same deuteron energy.

3.3.3 Results and discussion

The neutron spectra shown in Figure 3.6 obtained at E_d = 3.87 MeV and E_d = 9.39 MeV corresponding to the minimum and maximum neutron energy respectively, indicate that the production of break-up neutrons increases with deuteron energy. The dependence of reaction rates on neutron energy [*i.e.* $R = \sigma(E).\phi(E)$] were determined for $^{58}Ni(n,p)^{58}Co$ and $^{27}Al(n,\alpha)^{24}Na$ reactions in the knowledge of $\phi(E)$ obtained from the measured spectra and $\sigma(E)$ adopted from recent

evaluation (ENDF/B-VI, 1990). The ratios of reaction rates integrated over the group of break-up neutrons to the total (*i.e.* R_B/R_T) and that integrated over the group of monoenergetic neutrons to the total (*i.e.* R_M/R_T) are presented in Table 3.9.

Table 3.9 Ratios of reaction rates integrated over the groups of breakup and monoenergetic neutrons to the total at different incident neutron energies for $^{58}Ni(n,p)$ and $^{27}Al(n,\alpha)$ reactions.

E_d (MeV)	E_n (MeV)	$^{58}Ni(n,p)^{58}Co^{m,g}$		$^{27}Al(n,\alpha)^{24}Na$	
		R_B/R_T	R_M/R_T	R_B/R_T	R_M/R_T
4.00	7.12	0.0028	0.9972	0.000	1.000
5.82	8.92	0.0580	0.9420	0.000	1.000
6.95	9.60	0.0668	0.9332	0.000	1.000
7.34	10.30	0.2350	0.7750	0.002	0.998
8.20	11.13	0.2550	0.7450	0.003	0.997
9.73	12.20	0.4740	0.5260	0.011	0.989

The contributions of break-up neutrons to the total activation for the two reactions at different incident neutron energies can be taken into account. As can be seen in Table 3.9 the maximum contributions of low energy neutrons to the total activation of $^{27}Al(n,\alpha)^{24}Na$ and $^{58}Ni(n,p)^{58}Co^{m,g}$ reactions are 1.1 % and 47.4 % respectively. This can be attributed to the large spread observed in the cross section data of $^{58}Ni(n,p)^{58}Co^{m,g}$

reaction in the region between 9 and 13 MeV for which no other practical monoenergetic neutron source is available. Furthermore, the flux density spectra of neutrons determined by the activation unfolding and PHRS techniques are compared in Figure 3.7. However the activation unfolding technique gives a lower average energy and higher energy spread than the PHRS technique while the high threshold of the PHRS system prevents the detection of neutrons with energies below 1.5 MeV. In order to check the effect of self-buildup of deuterium in the beam stop, the spectral distributions of neutrons were measured using a fresh and used W beam stops. The spectra shown in Figure 3.8 indicate the contribution is negligible after about 50 hours irradiation time.

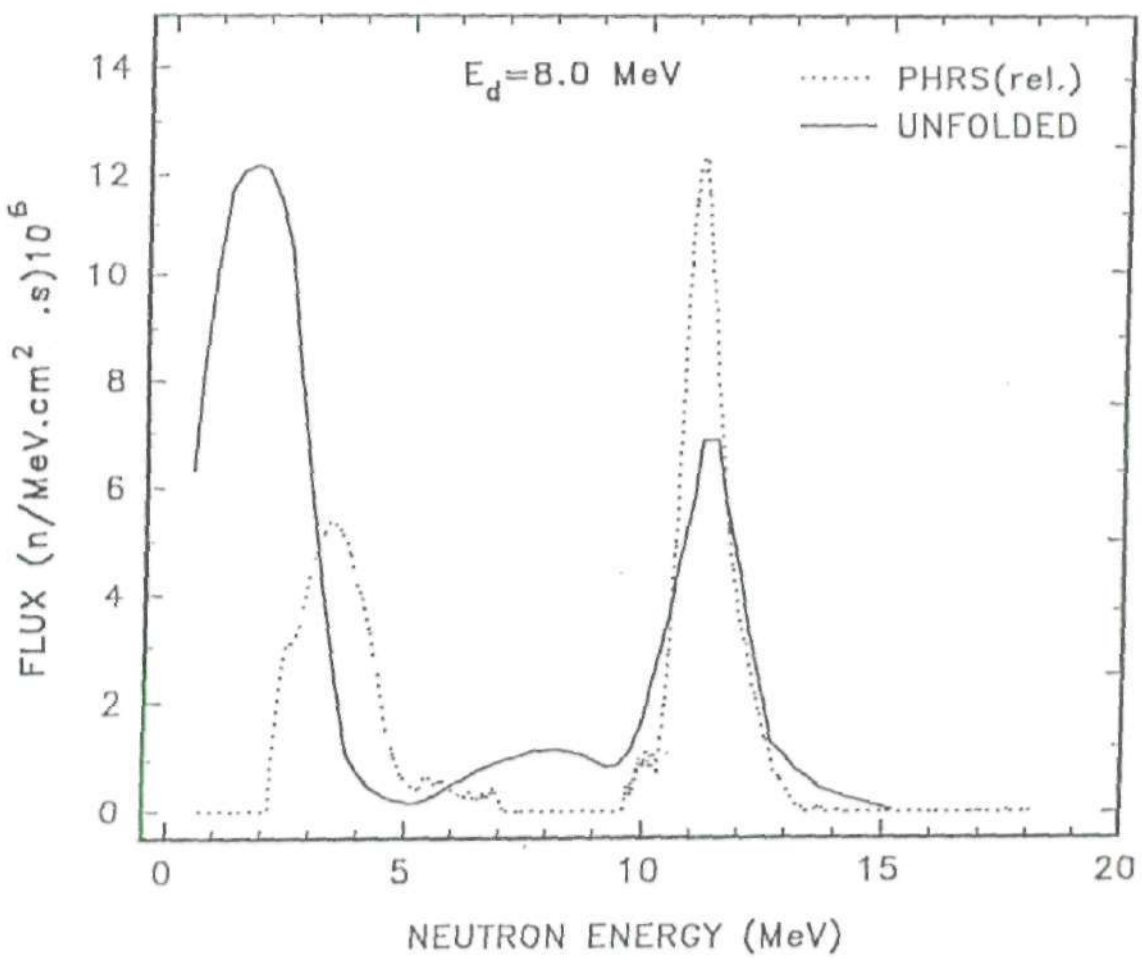


Fig. 3.7 A comparison of neutron spectra measured by PHRS and activation unfolding techniques

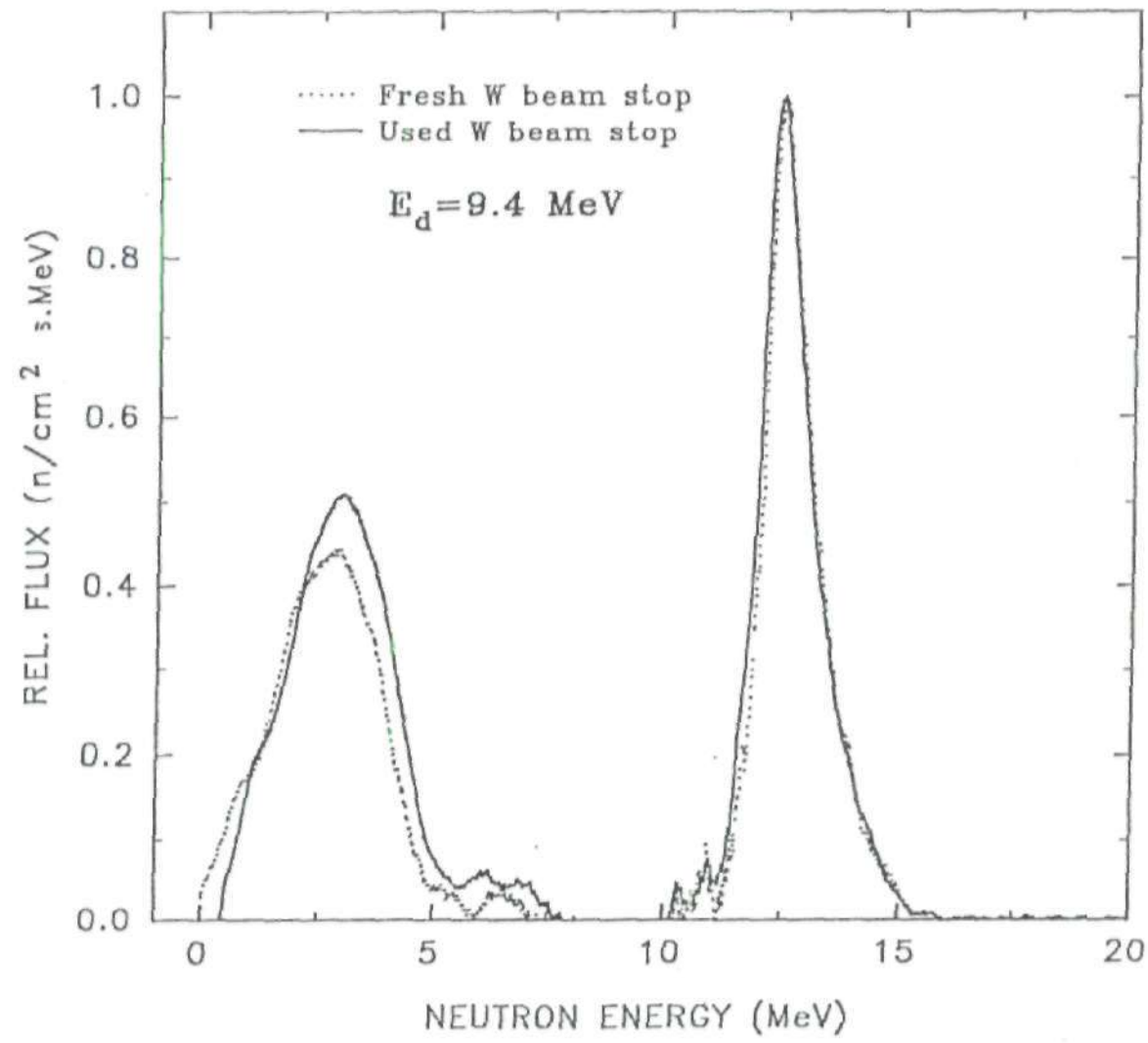


Fig. 3.8 A comparison of spectra distributions of neutrons produced with fresh and used W beam stop in the gas cell

CHAPTER FOUR

4.0 EXCITATION FUNCTIONS AND ISOMERIC CROSS SECTION RATIOS

4.1 Introduction

In general, the studies of excitation functions of neutron threshold reactions are of considerable importance for testing nuclear reaction models and various other applications especially in neutron dosimetry and spectral measurements. Furthermore, the investigation of energy dependence of isomeric cross section ratios are of fundamental interest for studying the role of spin values in the formation of isomeric states. A survey of the available literature (McLane *et al.*, 1988; CINDA-94, 1994) shows that both the cross section data (σ_{act}) and the isomeric cross section ratios (σ^m/σ^g) for many neutron induced reactions are rather scanty and discrepant.

Nickel is an important structural material used in fission and fusion reactor technologies therefore useful information on hydrogen-gas production can be derived from measured cross section data of $^{58}Ni(n,p)^{58}Co^{m,g}$ reaction. Since this reaction is also a dosimetry reaction used for flux and spectral measurements, it appeared worthwhile to investigate it. The cross section curves of the

$^{58}Ni(n,p)^{58}Co^{m,g}$ reaction measured by a number of investigators show a large spread in the 8-12 MeV range (Meadows and Whalen, 1963; Smith and Meadows, 1973; Raics *et al.*, 1981; Peiguo *et al.*, 1985; and Pavlik *et al.*, 1985). As a result of the spread, the evaluated data are also discrepant (Zhao *et al.*, 1989 and ENDF/B-VI, 1990). However of greater interest is the isomeric cross section ratio for which there are no published data in the 5-13 MeV range (McLane *et al.*, 1988 CINDA-94, 1994). This may be attributed to the unfavourable decay scheme of $^{58}Co^{m}$ and the difficulties in determining precisely the characteristics of the incident neutrons.

In this chapter, experimental studies in the neutron energy range of between 5 and 15 MeV were performed on the $^{58}Ni(n,p)^{58}Co^{m,g}$ reaction to determine the σ_{act} and the σ^{m}/σ^{g} ratio. The measured data are compared with evaluated data and calculational results using different nuclear reaction models.

4.2 Principles of Cross section Measurements

Being uncharged, neutrons can penetrate deeply to interact with the atomic nuclei of a sample giving rise to several nuclear reactions. A quantitative measure of the probability of occurrence of a given nuclear reaction induced by neutrons is referred to as the cross section. Consider a particular neutron interaction in which a mass containing N target nuclei is exposed to a flux of neutron

ϕ ($cm^{-2}s^{-1}$). The number of interactions X_i occurring in 1 second given by the expression below, is directly proportional to the number of target nuclei N, and the flux of neutrons:

$$X_i = \sigma_i . N . \Phi \qquad 4.1$$

where, σ_i is the cross section of the given interaction (in cm^2). For practical purposes the accepted unit is the millibarn (mb) and 1 barn = 10^{-24} cm^2. Equation 4.1 is similar to the basic equation of activation analysis (*i.e.* equation 2.43). Since the other parameters are well known, then the cross section of a given reaction can be calculated by the formula below.

$$\sigma_{act} = \frac{A.\lambda}{\phi.n.f.I_\gamma.\varepsilon_d.\varepsilon_a.\varepsilon_c.\varepsilon_f.\eta.[1-\exp(-\lambda t_i)].\exp(-\lambda t_c).[1-\exp(-\lambda t_m)]} \qquad 4.2$$

where,

A = peak area.

λ = decay constant (s^{-1}).

ϕ = neutron flux ($n.cm^{-2}.s^{-1}$) measured by foil monitor.

f = isotopic abundance of the target nuclei.

I_γ = absolute emission probability of the gamma line.

ε_d = dead-time correction.

ε_a = self-absorption correction.

ε_f = correction due to time-variation in flux.

ε_c = cascade coincidence correction.

η = full-energy-peak efficiency of the detector.

t_i = irradiation time.

t_c = cooling time.

t_m = measuring time.

$n = \frac{m.N_a}{M}$ is the number of target nuclei

m = mass of sample.

M = atomic mass.

N_a = Avogadro's number.

The uncertainty in the determination of the cross section is estimated by summing the errors of individual quantities in a quadrature.

4.3 Experimental Procedures

4.3.1 Irradiation

Pure samples of metallic nickel 19 mm in diameter and of thickness 1 mm were irradiated for between 3-10 hours depending on the neutron flux values at the irradiation positions. Irradiations in the 13.5-14.8 MeV neutron energy range were carried out with a low-current neutron generator in which monoenergetic neutrons are produced via the $^3H(d,n)^4He$ reaction by a 190 keV analyzed deuteron beam incident on a titanium-tritium target. In order to avoid the absorption of neutrons and decrease their energy spread, a thin target was used in a scattering-free arrangement described in section 3.2. The samples and the

corresponding flux monitor foils (same size as sample) were fastened back-to-back on an aluminum ring-shaped support of 20 cm diameter. The energy of the bombarding neutrons were varied through its angle dependence by placing the samples and the corresponding niobium flux monitoring foils at angles 0°,30°,60°, and 90° relative to the direction of the deuteron beam. The angular energy dependence of this source has been determined experimentally in section 3.2.

In the 5-13 MeV neutron energy range, irradiations were performed with quasi-monoenergetic neutrons produced via $^{2}H(d,n)^{3}He$ reaction at the variable-energy MGC-20 cyclotron. The neutron flux at each sample positions were determined by aluminum foils via the $^{27}Al(n,\alpha)^{24}Na$ reaction. Characteristics of the neutrons produced by this source have been determined experimentally in section 3.3. In all irradiations conducted, the variation of the neutron flux with time was monitored continuously by a long-counter system. Nuclear data of sample and flux monitor adopted in this experiment are given in Table 4.1.

4.3.2 Activity measurements

The (n,p) reaction on ^{58}Ni produces a metastable state radionuclide $^{58}Co^{m}$ and a ground state radionuclide $^{58}Co^{g}$. As shown in the decay scheme (Figure 4.1), the $^{58}Co^{m}$ decays by the emission of a low-energy γ-ray (*i.e.* E_{γ} = 24.9) with 3 % abundance hence the cross section for the production of metastable state can be determined either through the

contributions of the metastable to the ground state or through the analysis of Co X-rays. Since the half-life of the metastable state is much shorter than that of the ground state, the contributions of metastable state formation to that of the ground state can be determined by measuring the activity under 810 keV line continuously as function of time for 90 hours starting immediately after the irradiation.

Thus the isomeric cross section ratio can be deduced from the evaluation of a saturation decay curve measured by the NaI(Tl) detector system described in section 2.4.1. For the determination of σ_{act} the induced activity of Ni foils was measured via the 810 keV line after the complete decay of $^{58}Co^{m}$. Corresponding neutron flux values were determined via the radioactivity of the respective monitor foils. The Ge-Li detector system was used to carry out the activity of samples and monitor foils.

Table 4.1 Nuclear data accepted for the determination of the cross section curves.

	Radionuclide	E_{γ} (keV)	Half-life	I_{γ} (%)
Sample	^{58m}Co	24.9	9.15 h	0.032
	^{58}Co	810.6	70.78 d	99.44
Monitor				
5-13 MeV	^{27}Al	1368.5	15.03 h	100.0
13-15 MeV	^{92m}Nb	934.5	10.15 d	100.0

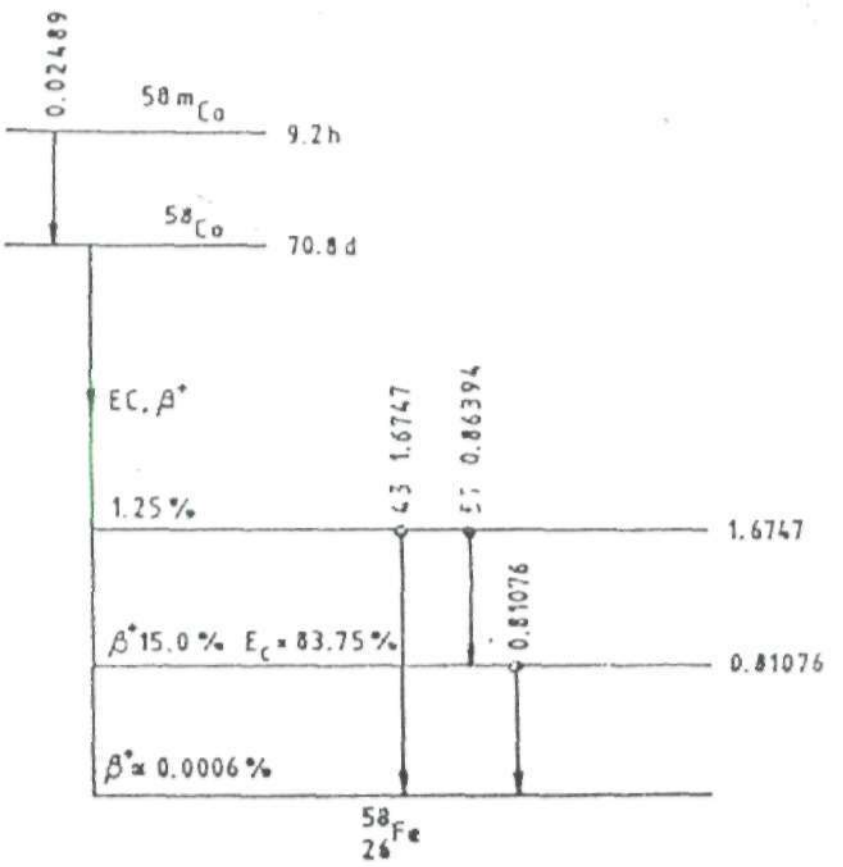


Fig. 4.1 The decay scheme of ^{58}Co radionuclide

4.4 Data Evaluation and Correction

The measured peak areas were corrected for the following effects: dead-time, controlled by the analyzer; cascade coincidence calculated from the knowledge of the measured total efficiency of the detector for the gamma line used and the decay scheme of the residual radionuclide taken from the Lederer and Virginia (1978); time-variation of neutron flux, calculated from the BF_3 monitor counts; and the self-absorption calculated using data taken from Storn and Israel (1970). In addition to these corrections, the contribution of the annihilation peak to the decay of the daughter radionuclide was also taken into consideration in the cascade coincidence correction. Cross sections data of the monitor reactions were taken from the dosimetry file (IRDF-90, 1990). The total cross-section (σ_{act}) for each of the Ni sample and the corresponding neutron flux value were calculated by the well known activation equation expressed in equation 4.2. The major source of error comes mainly from the contribution of break-up neutrons especially between 8 and 13 MeV which is about 47 % at 12.2 MeV. Other sources of error include the uncertainty in averaging the neutron flux (< 3 %) ; error in the efficiency of detector incorporating the error in counting geometry 2 %; uncertainties in the determination of peak areas < 1 % and uncertainty in the determination of true coincidence

correction. The isomeric cross section ratios were determined from the formula given in equation 4.3 which expresses the number of ground state atoms (N_g) as function of cooling time (t_c).

i.e.

$$N_g = \phi.n.\left(\left(\frac{\sigma^m.\beta + \sigma^g}{\lambda_g} + \frac{\sigma^m.\beta}{\lambda_m - \lambda_g}\right).[1 - \exp(-\lambda_g t_i)].\exp(-\lambda_g t_c)\right.$$

$$\left. - \frac{\sigma^m.\beta}{\lambda_m - \lambda_g}[1 - \exp(-\lambda_m t_i)].\exp(-\lambda_m t_c)\right) \qquad 4.3$$

where, m and g indicate the isomeric state and the ground state quantities respectively.

β is the branching ratio in the decay of the metastable state ($\beta = 1$ in this case).

The proof of equation 4.3 is given in the appendix. The intensity $I(t_c)$ obtained experimentally is proportional to $N_g(t_c)$ and can be approximated by the sum of two exponential functions given below in equation 4.4.

$$I(t_c) = \phi.n.[A.\exp(-\lambda_g.t_c) + B.\exp(-\lambda_m.t_c)] \qquad 4.4$$

where, A and B are the fitting parameters which are expressed below as:

$$A = \frac{\sigma^m + \sigma^g}{\lambda_g} + \frac{\sigma^m}{\lambda_m - \lambda_g}.[1 - \exp(-\lambda_g.t_i)] \qquad 4.5$$

and

$$B = -\frac{\sigma^m}{\lambda_m - \lambda_g}.[1 - \exp(\lambda_m.t_i)] \qquad 4.6$$

From equations 4.5 and 4.6 it is evident that σ^m/σ^g

can be expressed as:

$$\sigma^m/\sigma^g = \frac{\lambda_g - \lambda_m}{\lambda_m[1 + (\lambda_g/\lambda_m).(S_m/S_g).(A/B)]} \qquad 4.7$$

where, $S_m = [(1 - \exp(-\lambda_m.t_i)]$ and $S_g = [(1 - \exp(-\lambda_g.t_i)]$
The unknown parameters A and B are the coefficients of an exponential fit of the measured data performed with the PLOT40 code. Thus the isomeric cross section ratios were calculated at different bombarding energies.

Furthermore, the cross section data for the production of the isomeric state (*i.e.* σ^m) were deduced using the formula given in equation 4.8.
i.e.

$$\sigma^m = \frac{\sigma_{act}}{1/R + [\lambda_m/(\lambda_m - \lambda_g)]} \qquad 4.8$$

4.5 Results and Discussion

As can be seen in decay curve shown in Figure 4.2 which was fitted by the least square method, a good fit was obtained for the measured data. This shows that equation 4.3 adopted gives a good approximation by which the contributions of the metastable state can be taken into account. The measured activation cross section data and the isomeric cross section ratios together with the uncertainties are stated in Table 4.2. Similarly column 4 contains the cross section data for the formation of

metastable state deduced in the knowledge of σ_{act} data and σ^m/σ^g ratios. Over the energy range between 5 and 13 MeV the isomeric cross section ratio data presented have been measured for the first time.

Table 4.2 A summary of measured total cross section, metasatable state cross section and isomeric cross section ratio data for $^{58}Ni(n,p)^{58}Co^{m,g}$ reaction

Neutron energy (MeV)	Measured σ_{act} (mb)	Measured σ^m/σ^g	Deduced σ^m (mb)
5.38	538±27	0.54±0.01	168±12
5.89	576±29	0.55±0.01	210±12
6.39	617±31	0.52±0.01	220±14
6.80	657±33	0.61±0.02	254±18
8.02	681±34	0.62±0.02	259±18
8.43	683±34	0.62±0.02	261±18
8.92	667±33	0.64±0.02	247±17
9.60	668±33	0.79±0.02	294±20
10.95	631±32	-	-
11.13	613±32	0.77±0.02	266±18
12.20	559±28	0.71±0.02	231±16
12.38	526±26	-	-
13.52	401±12	-	-
14.10	340±10	-	-
14.46	319±16	-	-
14.74	288±14	-	-
14.84	281±14	1.08±0.03	145±10

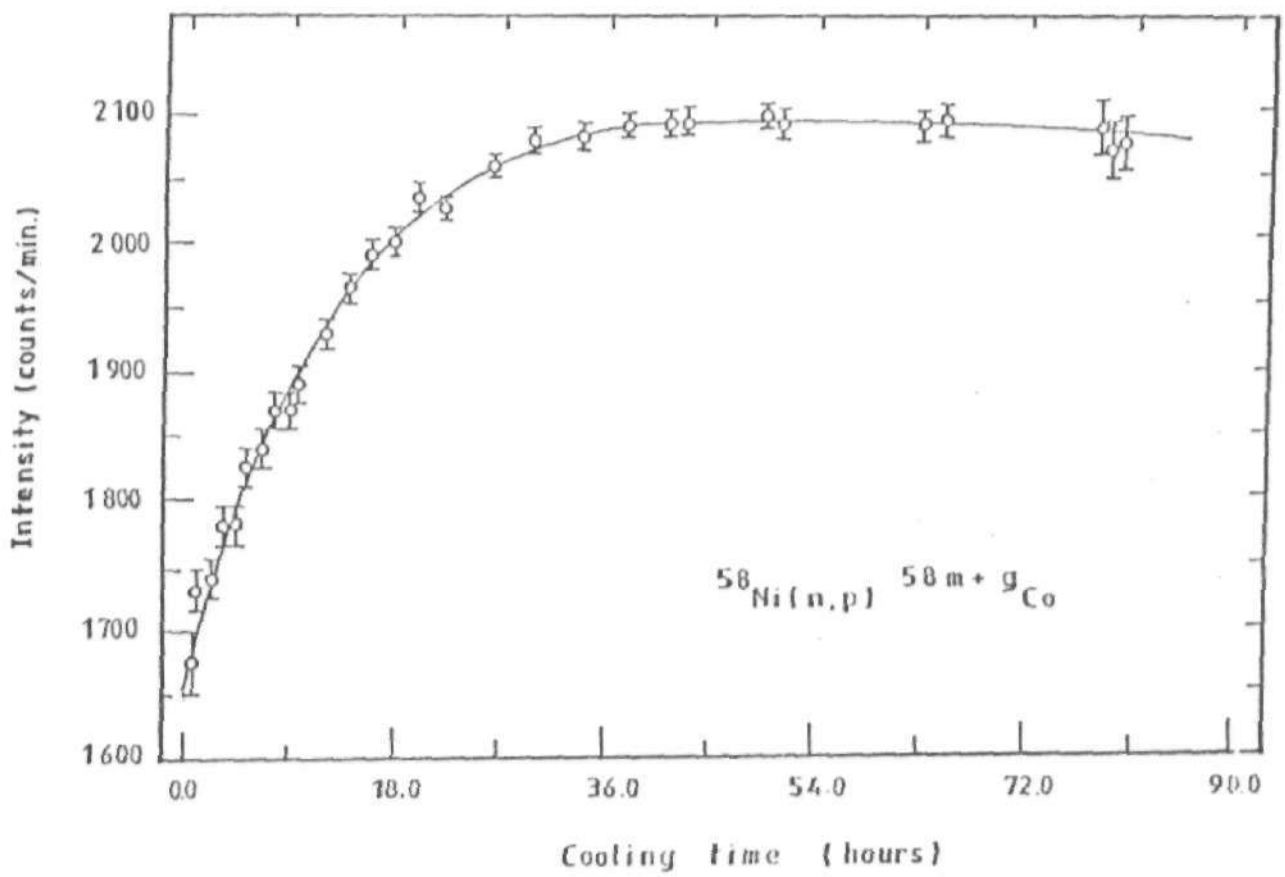


Fig. 4.2 Typical intensity vs. cooling time decay-curve of $^{58}Co^{m,g}$ radionuclide

In Figure 4.3 σ_{act} data measured in this work are compared with evaluated data (Zhao *et al.*, 1989 and ENDF/B-VI, 1990) and data obtained using nuclear models (Sudar, 1994; Zelenetsky, 1994; and Avrigeanu *et al.*, 1994). As can be seen, over the whole energy range the measured data agree well with the Zelenetsky's calculation in which the "super fluid" level density model was adopted in the STAPRE code. Similarly the calculational results of Sudar in which the "back shifted" level density model was used give an acceptable agreement with the present measurements. In Avrigeanu's calculation the code STAPRE-H was used in which the "geometry-dependent hybrid model" was adopted for pre-equilibrium estimation. The model gives 10-15 % lower values than the measured data in the 5-10 MeV energy range. The evaluation of Zhao *et.al.*(1989) deviate from the recommended data (ENDF/B-VI, 1990) especially at around 11 MeV in agreement with the measured data. As a comparison, the excitation function of $^{58}Ni(n,p)^{58}Co^{m,g}$ reaction measured in this work and the data measured by other investigators are presented in Figure 4.4 alongside the evaluated and calculated excitation functions.

The discrepancies observed in the 8-12 MeV neutron energy region could be attributed to the unfavourable decay scheme of ^{58}Co residual radionuclide and the diffulties in determining accurately the spectral distributions as well as the mean energies of incident neutrons.

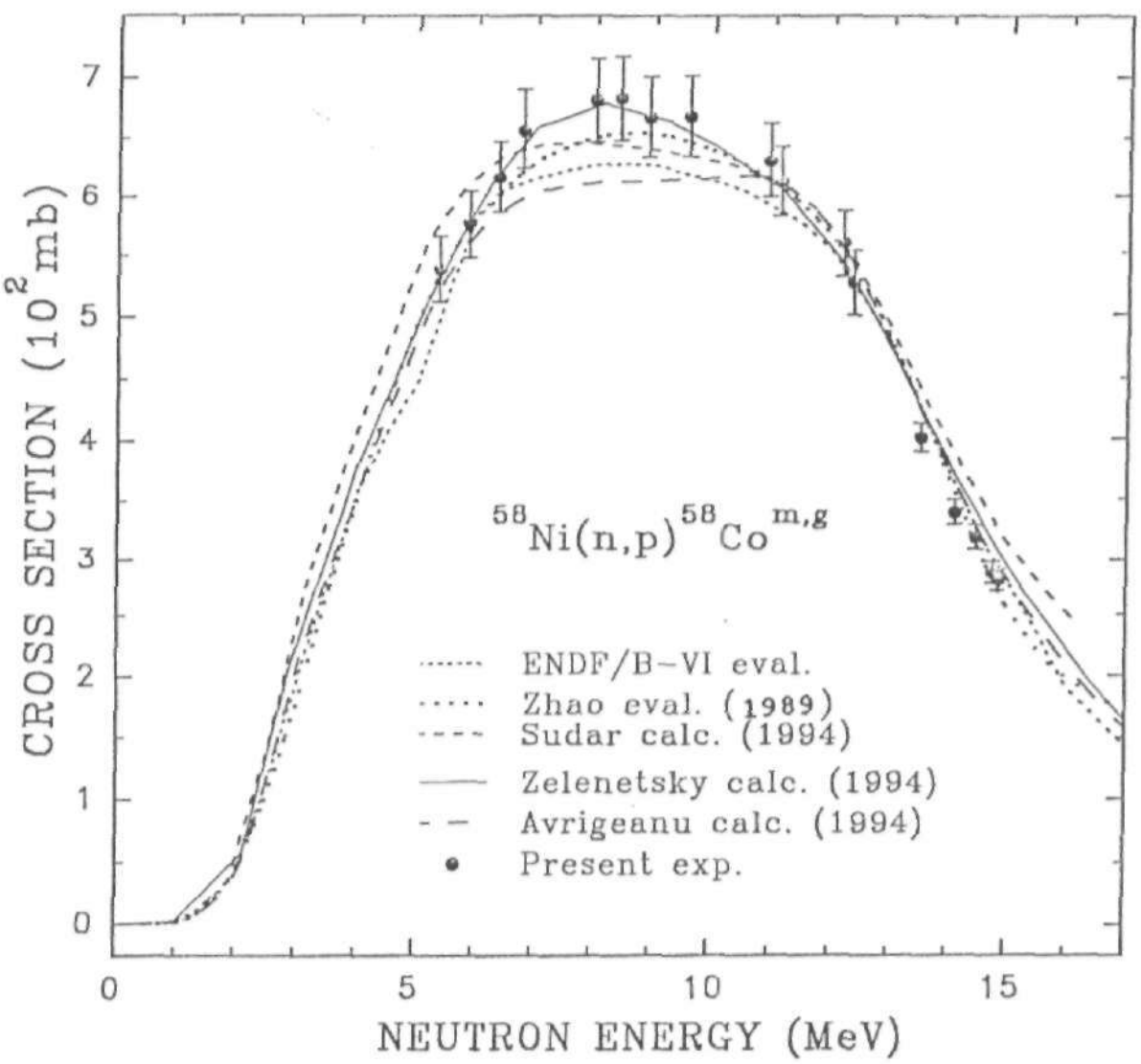


Fig. 4.3 Measured, calculated and evaluated excitation functions of $^{58}Ni(n,p)^{58}Co^{m,g}$ reaction

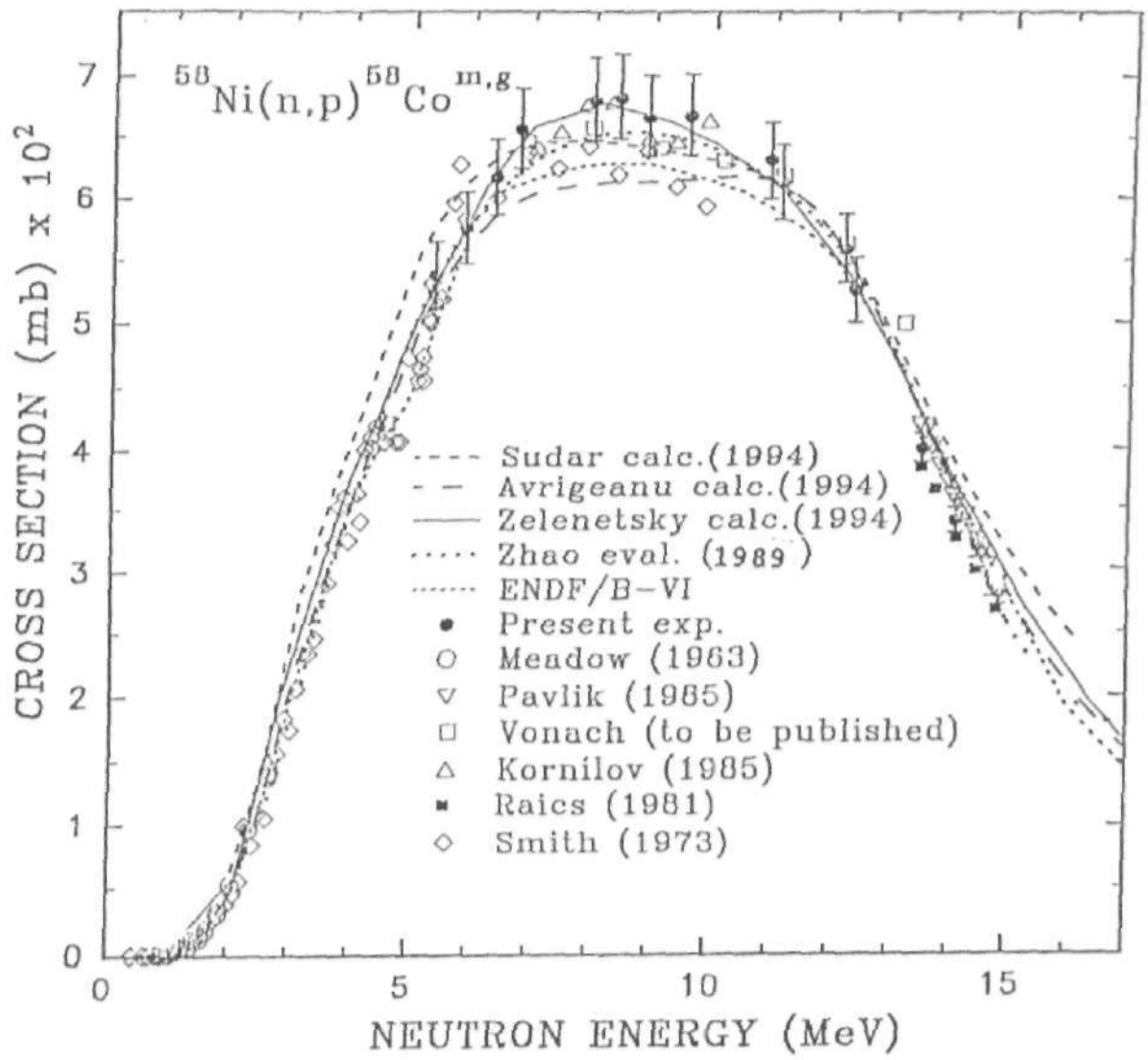


Fig. 4.4 A comparison of measured, calculated and evalutated excitation functions of $^{58}Ni9n,p)^{58}Co^{m,g}$ reaction

The isomeric cross section ratios determined in the current measurement and those available in the literature are displayed along side the calculated data in Figure 4.5. The model calculations of Sudar can be seen to produce the isomeric cross section ratio fairly well which indicates the possible use of the adopted model. At around 14 MeV the two independent calculations give lower values than the experimental results which are themselves discrepant. However, it can be seen that both the measured and calculated σ^m/σ^g data as a function of projectile energy show a definite increase indicating that the high spin (5^+) isomeric state is preferentially populated at higher energies.

In Figure 4.6 cross section data (σ^m) for the production of isomeric state deduced in this work and the measured data available in the literature (Cross *et al.*, 1963; Levkovskij *et.al.*, 1969; Hudson *et al.*, 1978; Bahal *et al.*, 1984; Ribansky *et al.*, 1985; Viennot *et al.*, 1991; and Sudar *et al.*, 1992;) are presented together with the evaluated and calculated data. As can be seen the values deduced in this work agree well with the literature data as well as the Sudar's calculations but deviate significantly from the Zelenetsky's calculations and the recommended data (ENDL/A, 1978).

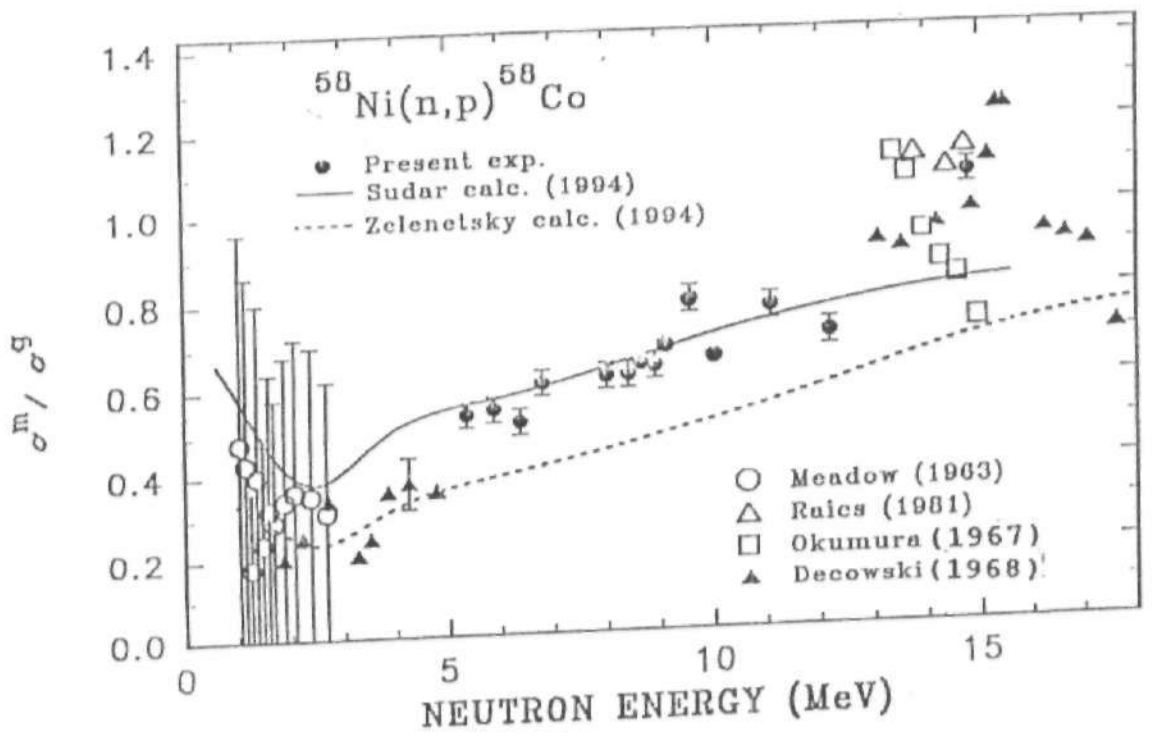


Fig. 4.5 Isomeric cross section ratio of $^{58}Ni(n,p)^{58}Co^{m,g}$ reaction as a function of neutron energy

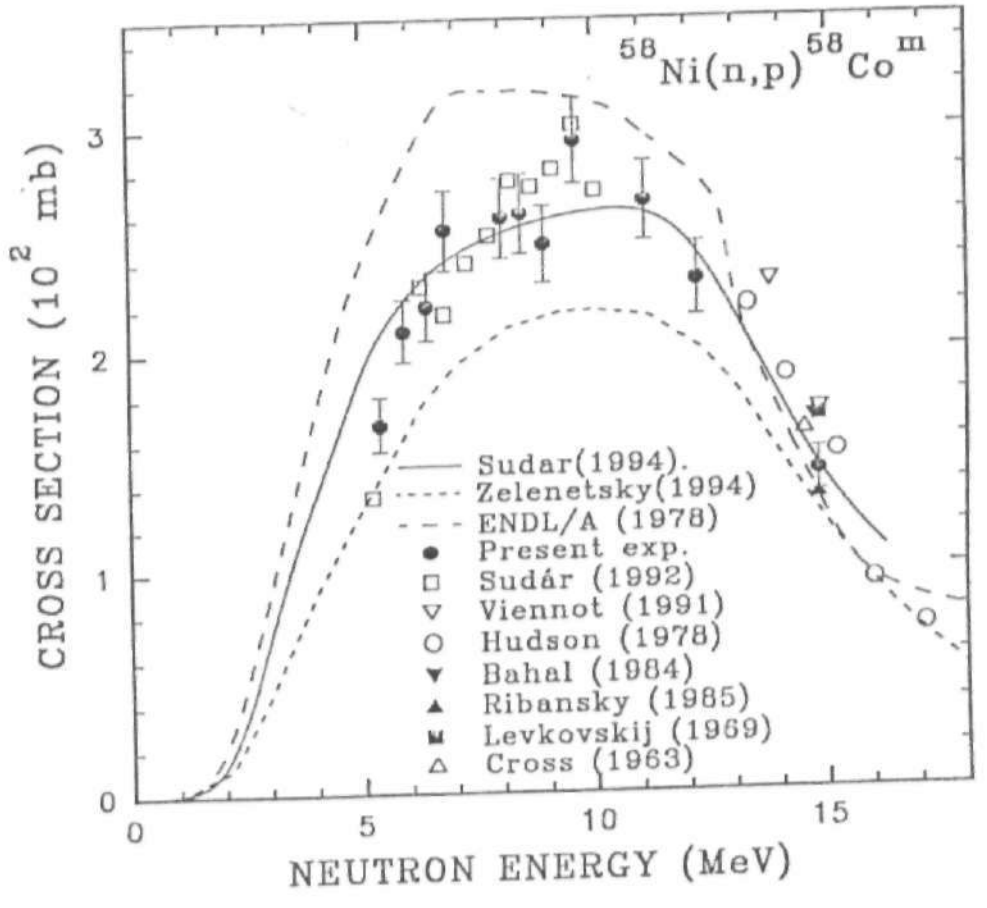


Fig. 4.6 A comparison of measured, calculated and evaluated excitation functions of $^{58}Ni(n,p)^{58}Co^{m,g}$ reaction

CHAPTER FIVE

5.0 CHARACTERISTIC DATA OF NEUTRON INTERACTIONS USED IN THE ANALYSIS OF BULK SAMPLES

5.1 Introduction

Prompt gamma-rays are produced via thermal neutron capture (n,γ), inelastic scattering (n,n'γ) and fast neutron induced (n,x,γ) processes by both thermal and fast neutron interactions. These reactions are widely used in the elemental analysis of geological samples especially for the on-line analysis of minerals based on 14 MeV sealed-tube neutron generator (IAEA, 1993). The (n,γ) and (n,x,γ) reactions are quite complimentary to each other. For example the (n,γ) reaction cross section is low for Li, Be, B, C, N, O, Na, Mg, and Al while the yield and the specificity of the gamma-rays from (n,xγ) reaction for these elements are very high. Consequently, the prompt gamma-rays used in the elemental analysis of bulk media are produced by both the thermal and the fast neutron interactions.

It has been shown that the thermal neutron flux distributions needed for the analysis of coal strongly depends on the source-sample configurations and the elemental composition of coal (Clayton *et al.*, 1983). The

analytical sensitivities of the principal gamma-ray lines used in the thermal neutron capture gamma-ray spectroscopy have been investigated and compiled for most elements (Duffey *et al.*, 1970 and Senftle *et al.*, 1971). The effect of sample thickness and the shadow shield length on the determination of carbon via the $^{12}C(n,n'\gamma)$ reaction have been investigated (Watterson, 1993). The possible use of pulsed fast/thermal neutron technique for the on-line analysis of bulk coal have been suggested (Vourvopolous and Womble, 1989; Vourvopoulos and Shultz, 1993; Vourvopolous, 1993 and Vourvopoulos and Humphrey, 1994). Based on these investigations, it can be seen that an optimum geometrical arrangement exists to obtain the best analytical conditions for the analysis of coal. In this regard, the knowledge of thermal and fast neutron flux distributions in bulk samples is indispensable to the design and construction of an on-line analyzer based on the detection of prompt gamma-rays.

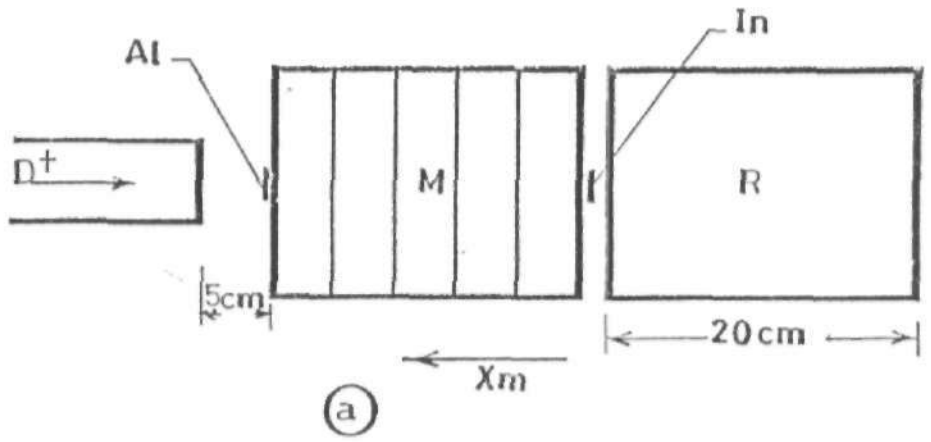
The main objective in this study is to develop a moderator-sample-reflector configuration in which an optimum values of thermal and fast neutrons can be achieved for the field and on-line analysis of coal and other minerals. Therefore as an initial step, the thermal and fast neutron flux distributions in different assemblies of bulk samples consisting of graphite, water and coal were investigated. Similarly, the flux density spectra of ^{252}Cf and ^{239}Pu-Be neutrons traversing different thicknesses of

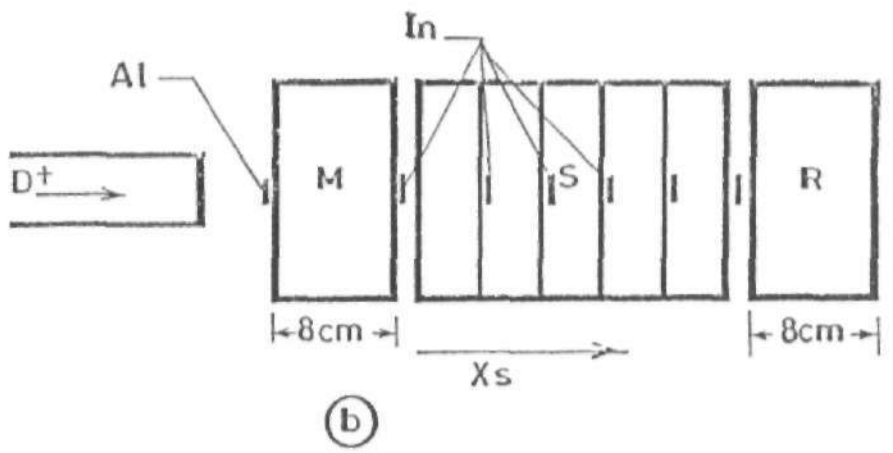
coal as well as the macroscopic removal cross sections of primary 14 MeV neutrons in water, graphite and coal were determined. Based on these measurements, an experimental data base is given for checking the results of different model calculations.

5.2 Thermal and Fast Neutron Flux Distributions in Bulk Samples

5.2.1 Experimental procedures

Different experimental setups shown in Figures 5.1a, 5.1b and 5.1c were used to study the distributions of thermal and fast neutron flux along the centre line of different assemblies of water, graphite and coal as moderator (M),sample (S), and reflector (R). Samples of 30 cm square panels of varying thickness were placed in front of point source 14.7 MeV neutrons. An intense 14 MeV neutron generator was used to produce fast neutrons via the $^{3}H(d,n)^{4}He$ reaction. The flux of primary fast neutrons was measured by disc-shaped high-purity aluminum foils of 19 mm diameter and 1 mm in thickness via the $^{27}Al(n,\alpha)^{24}Na$ reaction placed at 5 cm from the target. For the determination of thermal neutron flux distributions in the different moderator-sample-reflector geometries, the activities of disc-shaped indium foils of 19 mm diameter and 0.5 mm in thickness were measured via the $^{115}In(n,\gamma)^{116m}In$ reaction. Irradiation time of between 30 and 90 minutes were used depending on the flux values.





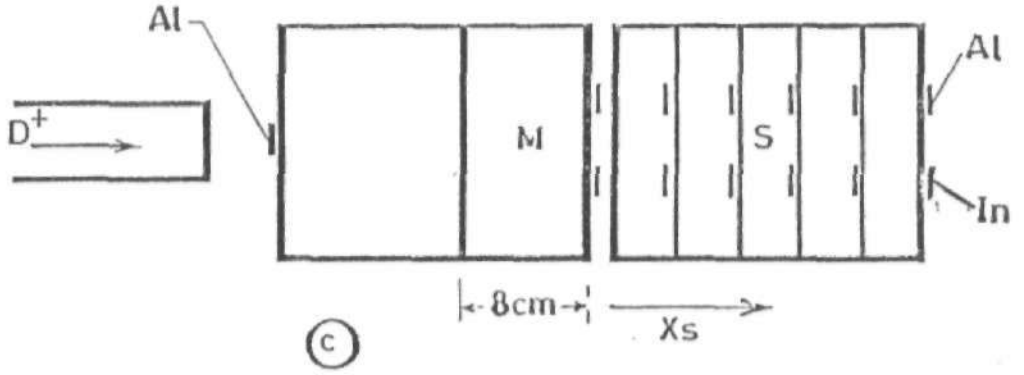


Fig. 5.1 Setup geometries used for the determination of fast and thermal neutron flux densities distributions in bulk samples

The decay characteristics of the residual nuclei used in the measurement are listed in Table 5.1.

Table 5.1 Nuclear data of the neutron flux monitor reactions

Reaction	Half-life	E_γ (keV)	I_γ (%)	σ(mb)
$^{27}Al(n,\alpha)^{24}Na$	15.02 h	1368.5	99.10	115.6
$^{115}In(n,\gamma)^{116}In^{m}$	54.12 min	416.86	29.20	1.62×10^{5}
		1097.30	56.20	
		1293.54	84.40	

5.2.2 Data measurement and evaluation

Radioactivities of the monitor foils were measured by the Ge-Li detector system described in section 2.4.1. The peak area analysis of gamma-ray spectra was performed by the ACCUSPEC code while the calculation of the flux was carried out by the ASEASYAS computer code based on the activation analysis equation (Equation 2.43). The measured data corresponding to each of the experimental arrangements are stated below.

Neutron flux density at moderator-reflector interface as a function of moderator thickness: The experimental set-up shown in Figure 5.1a was used to determine the thermal and fast neutron flux distribution at moderator-reflector interface as a function of moderator thickness. Al and In monitor foils were placed at the interface and the thickness of water moderator was varied from 0 to 20 cm for slabs of water, graphite and coal as reflectors. Values of

the thermal neutron flux obtained for water, graphite and coal as reflectors are stated in Table 5.2.

Table 5.2 Measured thermal neutron flux density $\phi_{th}(X)$ at the moderator-reflector interface as a function of moderator thickness with water, graphite and coal as reflectors using the setup shown in Figure 5.1a

Moderator thickness (cm)	$\phi_{th}(X).10^5$ (n/cm^2.s)		
	Water	Graphite	coal
0	1.515	0.074	0.622
4	10.277	4.988	9.396
8	13.351	7.502	10.006
12	14.215	7.981	11.332
16	12.993	7.447	11.667
20	12.951	6.383	9.662

Thermal neutron flux distributions in assemblies of water, graphite and coal samples: The thermal neutron flux value at different positions in the assemblies of water, graphite and coal were determined using the set-up in Figure 5.1b. The effects of moderator and reflector on the thermal neutron flux distributions were studied by determining the flux values using the following configurations:

1) The thermal neutron flux distributions in bare samples consisting of water, graphite and coal which corresponds to having no moderator and reflector (*i.e.* $X_M = X_R = 0$)

2) The thermal neutron flux distributions in water, graphite and coal samples in the presence of 8 cm thickness of water as moderator and reflector (*i.e.* $X_M = X_R = 8$ cm)

3) The thermal neutron flux distributions in coal sample in the presence of only 8 cm thickness of water as reflector (*i.e.* X_M = 0, X_R = 8 cm, and r = 13 cm). The measured data belonging to each of the above experimental conditions are presented in Tables 5.3, 5.4 and 5.5 respectively.

Table 5.3 Measured thermal neutron flux density in bare samples consisting of water, graphite and coal using the setup shown in Figure 5.1b

Position in sample (cm)	$\phi_{th}(X).10^5$ (n/cm^2.s)			
	Water	Graphite	Coal	
			Polish	Hungarian
0	3.828	0.000	0.986	0.936
4	20.492	-	4.951	4.521
5	-	0.480	-	-
8	22.102	-	5.568	5.044
12	16.549	-	4.389	4.374
14	-	0.483	-	-
16	9.501	-	3.265	2.750
20	0.993	0.000	0.479	0.486

Thermal and fast neutron flux distributions in water, graphite and coal samples in the presence of 8 cm thickness of water as moderator: Thermal and fast neutron flux distributions in the samples $\phi(x)$ were measured using the set-up shown in Figure 5.1c in which an 8 cm thickness of water was used as the moderator. As shown in the diagram the thermal and fast neutron flux distributions were measured by indium and aluminum foils respectively. The data obtained for fast and thermal neutrons are presented in Tables 5.6. and 5.7 respectively.

Table 5.4 Measured thermal neutron flux in water, graphite and coal samples sandwiched between 8 cm thick water moderator and reflector (setup geometry Figure 5.1b)

Position in sample (cm)	$\phi_{th}(X).10^{6}$ (n/cm^2.s)		
	Water	Graphite	Coal
0	4.892	0.865	3.655
4	3.221	-	2.428
5	-	0.398	-
8	2.121	-	1.614
12	1.396	-	1.121
14	-	0.165	-
16	0.993	-	0.808
20	0.665	0.158	0.569

Table 5.5 Measured thermal neutron flux in coal sample with and without a reflector (setup geometry Figure 5.1b)

Position in coal (cm)	$\phi_{th}(X).10^{5}$ (n/cm^2.s)	
	with R	without R
0	1.685	0.986
4	7.643	4.951
8	8.456	5.568
12	9.082	4.389
16	8.773	3.265
20	7.839	0.479

Table 5.6 Measured fast neutron flux at different positions in samples using the setup shown in Figure 5.1c.

Position in sample (cm)	$\phi_f(X).10^6$ (n/cm^2.s)		
	Water	Graphite	Coal
0	0.780	0.859	0.837
4	0.436	0.636	0.597
8	0.311	0.370	0.361
12	0.180	-	0.254
16	0.108	0.197	0.200
20	0.080	0.135	0.142

Table 5.7 Measured thermal neutron flux at different positiions in samples using the setup shown in Figure 5.1c

Position in sample (cm)	$\phi_{th}(X).10^5$ (n/cm^2.s)		
	Water	Graphite	Coal
0	16.617	9.471	10.200
4	11.487	-	6.690
5	-	5.071	-
8	8.087	-	4.754
12	5.197	-	3.187
14	-	1.268	-
16	2.937	-	1.584
20	0.382	0.297	0.341

Data corrections: In addition to the corrections due to dead time and cascade coincidence effects considered in the determination of both the fast and thermal neutron flux values the following corrections were taken into account in

the determination of thermal neutron flux distributions.

1) The contribution of epithermal neutrons to the activation of indium monitor. This contribution was taken into account by the cadmium difference (Cd-difference) method. In this respect, the activity induced by thermal neutrons in a bare indium foil (A_{tot}) was measured and repeated with the indium foil encapsulated in 1 mm thick cadmium box (A_{epi}).

$$A_{th}/A_{tot} = 1 - A_{epi}/A_{tot} = 1 - \frac{975}{12315} = 0.92 \qquad 5.1$$

where, A_{th} is the activity induced by thermal neutrons in the sample. It can be seen that the contributions of epithermal neutrons to the activation of indium foils is 8 %.

2) The effect of flux depression and self-shielding factor (F_{SD}); The correction factor due to the effect of flux depression and self shielding factor was determined by experiment. Indium foils of different thicknesses were exposed to a benchmark field of thermal neutrons provided by a 0.5 Ci Pu-Be source embedded in a cylindrical-shaped paraffin moderator. The activity induced in each of the foil irradiated for 30 minutes are given in Table 5.8. From the plot of activity, A, versus foil thickness, x, shown in Figure 5.2, the correction factor F_{SD} was obtained thus:

$$F_{SD} = A_o/A_1 \qquad 5.2$$

where, A_o is the activity induced in an indium foil of 0.0 cm^2/g thickness obtained by the extrapolation of measured data to zero.

A_1 is the activity induced in an indium foil 0.5 cm^2/g in thickness which is the same as the thickness of the indium foils used. From Figure 5.2 and equation 5.2, $F_{SD} = 2.687$

Table 5.8 Specific activity induced in indium foils of different thickness

Foil thickness (mg/cm^2)	7.30	21.90	38.37	199.52	373.99	574.08	749.62
Specific activity ($cps/mg.cm^{-2}$)	86.70	82.60	78.50	48.70	32.90	27.10	24.00

Absolute fast and thermal neutron flux values given in the tables above were normalized to a 14 MeV neutron source strength of 10^{10} n/s and also corrected for the effect of room scattered neutrons.

5.2.3 Results and discussion

In the first experiment, the thermal flux distribution function $\phi_{th}(x)$ plotted in Figure 5.3 shows that irrespective of the reflector material a moderator thickness of 8-10 cm is sufficient to achieve saturation in the $\phi_{th}(x)$ function.

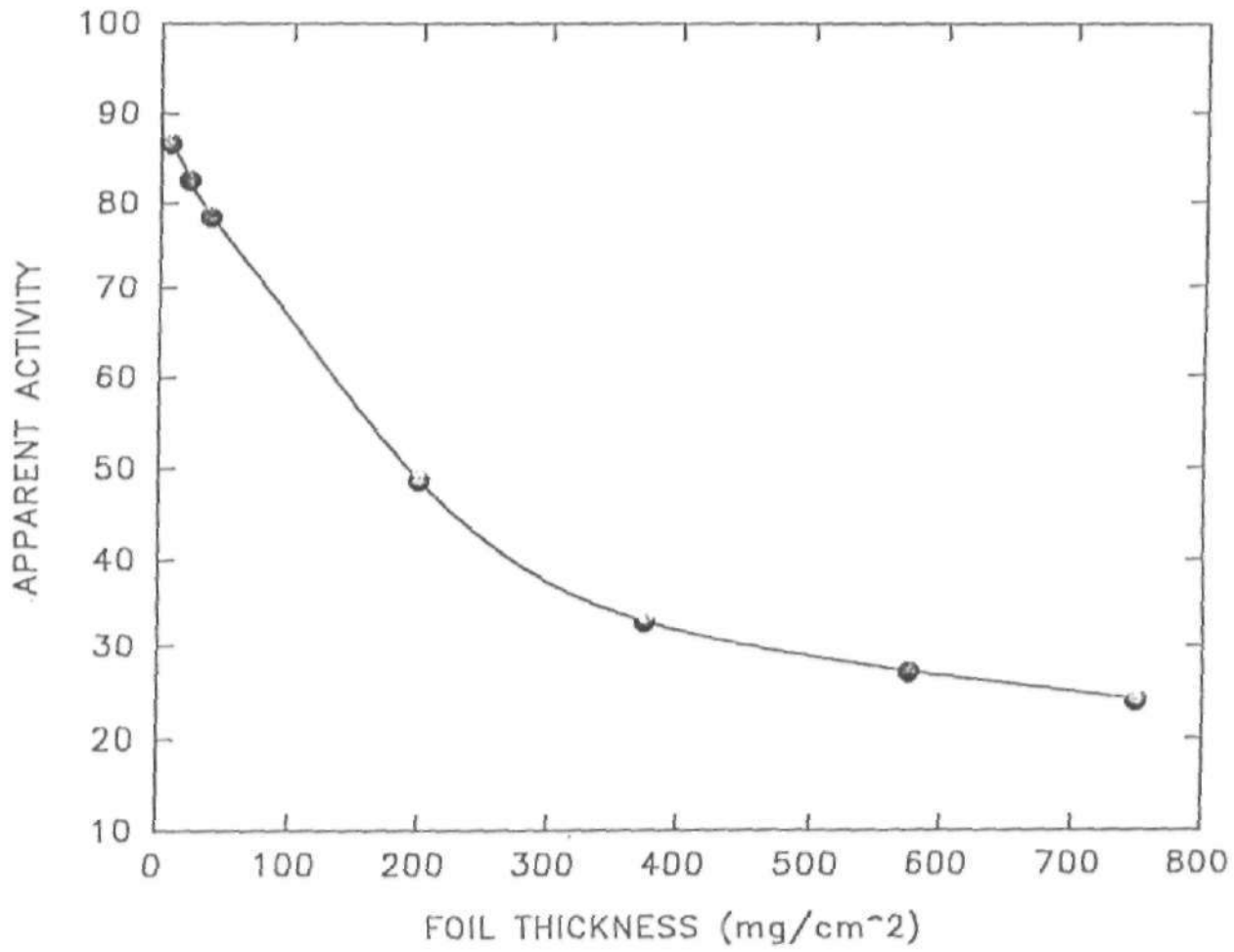


Fig. 5.2 Variation of activity with thickness of indium foil exposed to the same flux of thermal neutrons

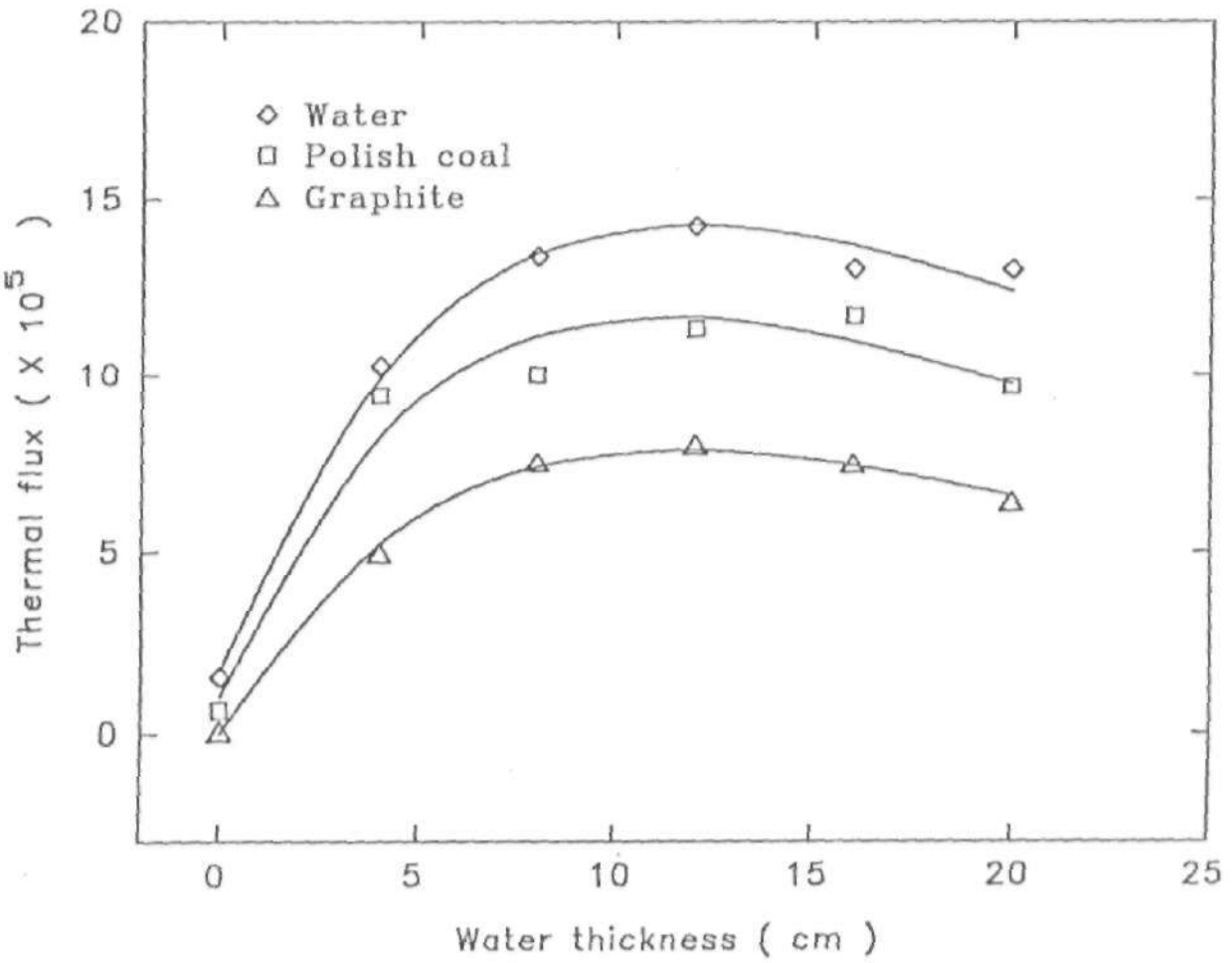


Fig. 5.3 Dependence of absolute thermal neutron flux density at moderator-reflector interface versus moderator thickness

The shapes and magnitudes of the $\phi_{th}(x)$ function depends on the hydrogen content of the reflector therefore the hydrogen content in coal must be between that in water and graphite. The solid line in the figure is obtained by fitting the measured thermal neutron flux values to the expression given below.

$$\phi_{th}(X) = a\,(1 - e^{-b.X})\,e^{-\Sigma_R} + R \qquad 5.3$$

where, the first, second and third terms are related to the slowing-down and diffusion of neutrons, the attenuation of primary fast neutrons in water and the effect of the reflector at X = 0, respectively. Values of a, b and R parameters summarized in Table 5.9 make it possible to calculate the absolute thermal flux densities at the interface for any given thickness of water moderator provided the yield of primary 14.7 MeV neutrons is known.

In the second set of experiments, the measured data as a function of sample thickness are displayed in Figures 5.4, 5.5 and 5.6 respectively. As can be seen in Figure 5.4 which corresponds to having just the bare sample, the thermal neutron flux distributions exhibit maxima at about X = 8 cm and can be fitted by the following expression.

$$\phi(X) = \frac{a\,(1 - b\,e^{-c.X})}{r + X}\cos\frac{\pi}{2}\,\frac{X}{X_o} \qquad 5.4$$

where, X_o = 20 cm (*i.e.* total thickness of sample) and r = 13 cm (*i.e.* distance between the sample and the source).

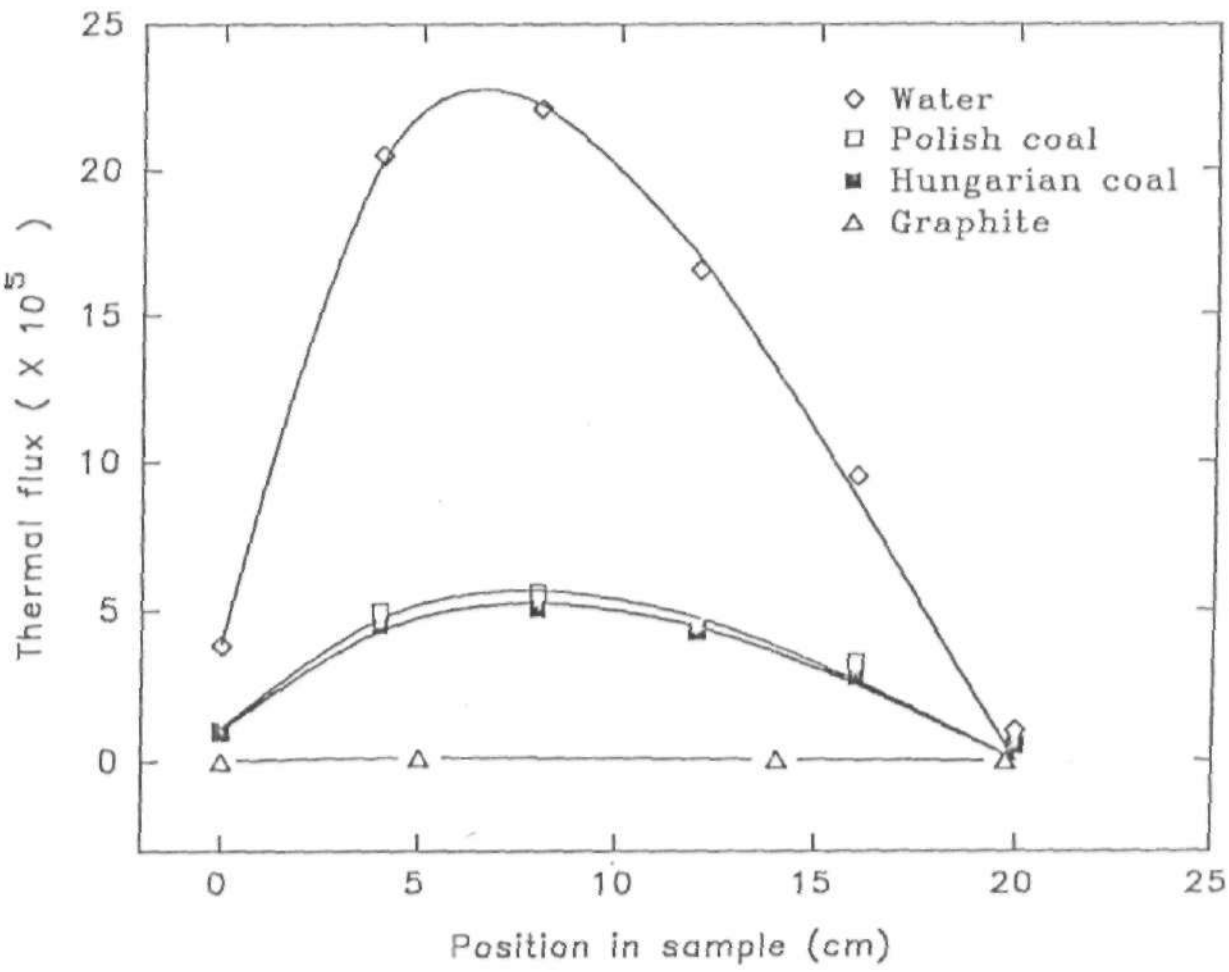


Fig. 5.4 Flux density distributions of thermal neutrons in the bare samples

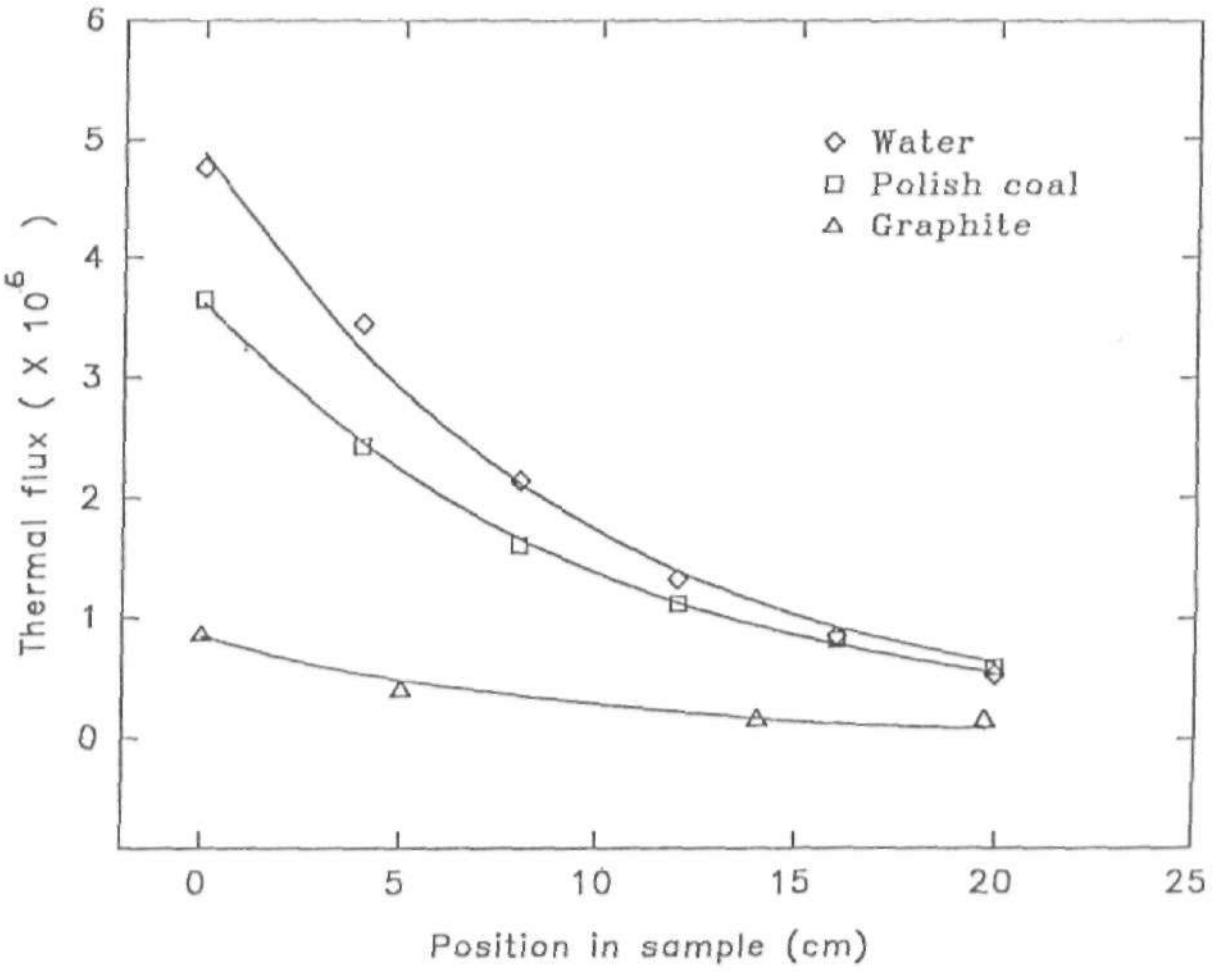


Fig. 5.5 Flux density distributions of thermal neutrons in samples sandwiched between water moderator and reflector

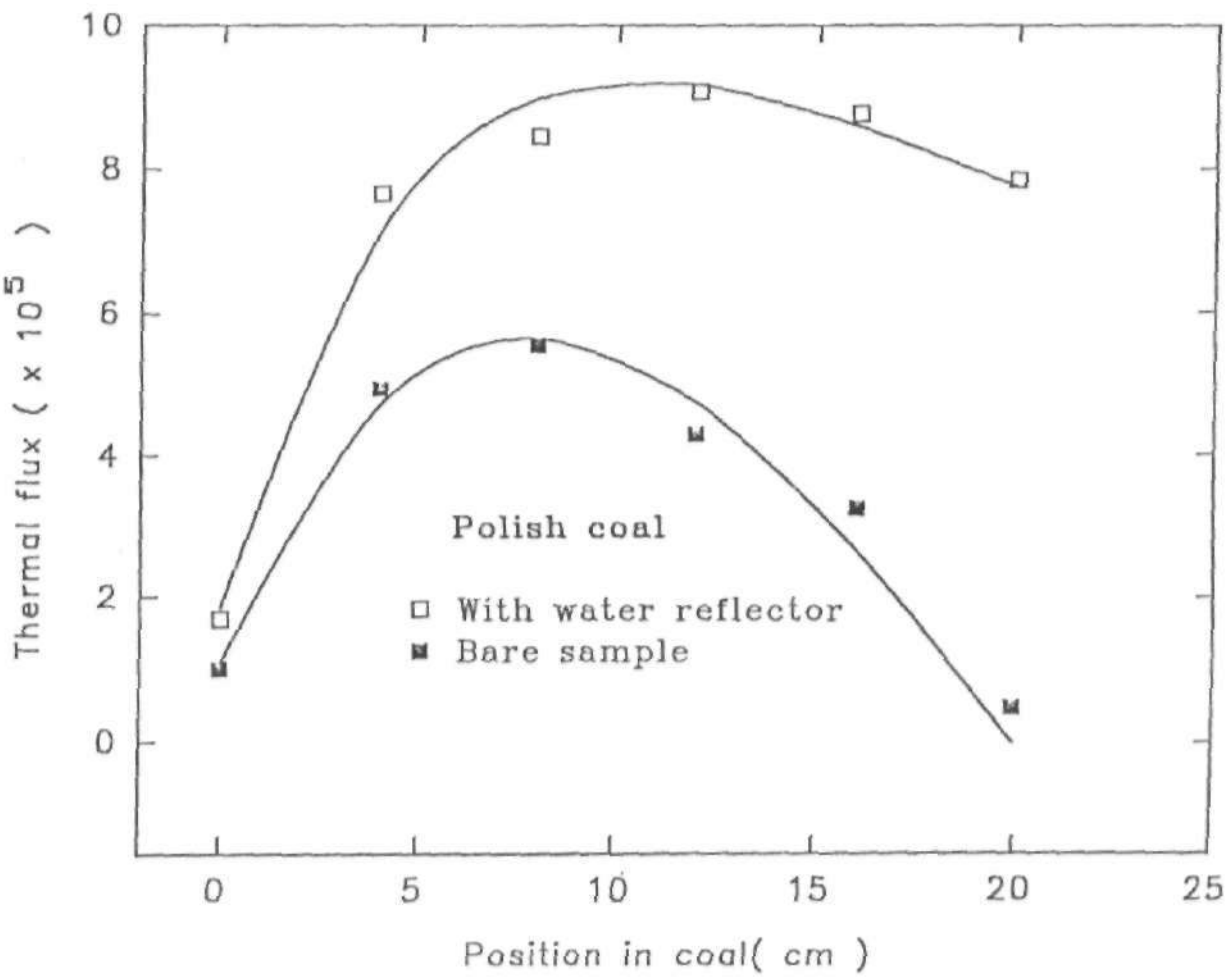


Fig. 5.6 Flux density distributions of thermal neutrons in coal samples with and without reflector

Table 5.9 Parameters for characterization of neutron fields in bulk samples. Data are normalized to 10^{10} n/s of 14.7 MeV neutrons

Parameter	Sample		
	water	graphite	coal
Eq.(5.3): a	5.929×10^{7}	1.993×10^{7}	1.8573×10^{7}
b	0.00486	0.00927	0.01392
R	1.691×10^{5}	2.1×10^{-5}	97733.0
Eq.(5.4) a	1.04×10^{8}	-	6.195×10^{7}
b	0.0949	-	0.03098
c	0.9516	-	0.9778
($X_M = X_R = 0$, r = 13 cm)			
Eq.(5.5): a	4.8915×10	7.298×10^{5}	3.4534×10^{6}
b	0.1045	0.2077	0.11055
R	0.0037	1.366×10^{5}	2.0192×10^{5}
($X_M = X_R = 8$ cm, r = 13 cm)			
Eq.(5.6): a	-	-	2.115×10^{6}
b	-	-	0.09361
R	-	-	1.847×10^{5}
($X_M = 0$, $X_R = 8$ cm r = 13 cm)			
Eq.(5.7): ϕ_o	1.701×10^{7}	9.567×10^{5}	1.0416×10^{6}
c	0.1052	0.1378	0.1077
(r = 25 cm, X = 8 cm)			
ϕ_{th}/ϕ_f, measured (r = 25 cm, X = 8 cm)	2.141	1.111	1.227

The expression given in equation 5.4 contains the build up, absorption and leakage of thermal neutrons while the values of a, b and c fitting parameters are given in Table 5.9. In Figure 5.5 in which the sample is sandwiched between water moderator and reflector, the values of $\phi_{th}(X)$ are considerably higher in the whole volume of sample as compared to the bare arrangement. The measured data in this configuration can be described by the following equation.

$$\phi_{th}(x) = a\, e^{-b.x} + R \qquad 5.5$$

where, R is the effect of the water reflector. The values of a, b and R fitting parameters are given in Table 5.9. As can be seen in the figure only a sample layer of about 15 cm contributes significantly to the sensitivity of the neutron capture gamma-ray analysis in the M-S-R geometry. The effect of a water reflector on the sample described in configuration 3 is demonstrated in Figure 5.6. It can be seen that the values of thermal neutron in the presence of a reflector can be increased and homogenized for a large volume. The thermal flux distribution measured for coal sample in the presence of a reflector can be described by the following relation.

$$\phi_{th}(X) = a\,(1 - e^{-bX})\, e^{-\Sigma_{R,C} X} + R \qquad 5.6$$

where, $\Sigma_{R,C}$ is the removal cross section of coal. The a, b and R fitting parameters are summarized in Table 5.9.

In equation 5.6, the first and second terms represent the buildup and attenuation of fast neutrons while the third term stands for the reflection of thermal neutrons.

The Thermal and fast neutron flux distributions in slabs of water, graphite and coal samples for the set-up shown in Figure 5.1c (*i.e.* r= 25 cm and X_M = 8 cm) are displayed in Figures 5.7 and 5.8 respectively. It can be seen in Figure 5.7 that the thermal neutron flux values decreases exponentially as a function of distance from the surface of moderator. This implies that the water layer can be considered as a plane source of thermal neutrons for which the following relation holds.

$$\phi_{th}(X) = \phi_{\circ}\, e^{-cX} \qquad 5.7$$

where, c is related to the diffusion length of thermal neutrons in the sample. The values of $\phi_{\circ}$ and c fitting parameters are given in Table 5.9. The measured thermal neutron flux values at the surface of samples can be seen to deviate from the fitted curve due to the effects of flux depression and angular distribution of neutrons at the surface of hydrogenous material. However results obtained indicate that most of the prompt gamma-rays used in the analysis of bulk samples are produced between 10 and 15 cm layer of the sample. The flux distribution of primary fast neutrons in the coal samples as a function of distance from the interface was approximated by the following expression.

$$\phi_f = \frac{Y}{4\pi(r + X_S)^2} e^{-\Sigma_{R,M} X_M} \; e^{-\Sigma_{eff,S} X_S} \qquad 5.8$$

where, X_M, X_S, $\Sigma_{R,M}$ and $\Sigma_{eff,S}$ are the thicknesses and macroscopic removal cross sections of moderator and sample respectively.

Considering the measuring geometry (Figure 5.1c) the macroscopic removal cross sections for the samples presented in Table 5.9 can be taken as the effective values. At the interface which can be regarded as the surface of a conveyor belt, the ratios of measured thermal neutron flux to the primary fast neutron flux are also given. The fast neutron flux distribution increases with sample thickness and carbon content from about 7 % at the interface to 100 % at the free surface. This effect indicates that in addition to the differences in attenuation coefficients, the contribution of inelastically scattered neutrons on ^{12}C in both backward and forward directions to the activation of Al monitors is higher than those emitted in the $^{16}O(n,n'\gamma)$ reaction.

From the results discussed above, it can concluded that the best analytical conditions for the on-line analysis of bulk samples based on the detection of prompt gamma-rays via the (n,γ), $(n,n'\gamma)$ and $(n,x\gamma)$ reactions can be achieved in a set-up shown in Figure 5.1b if the neutron source and the gamma-ray detector are placed close to the sample.

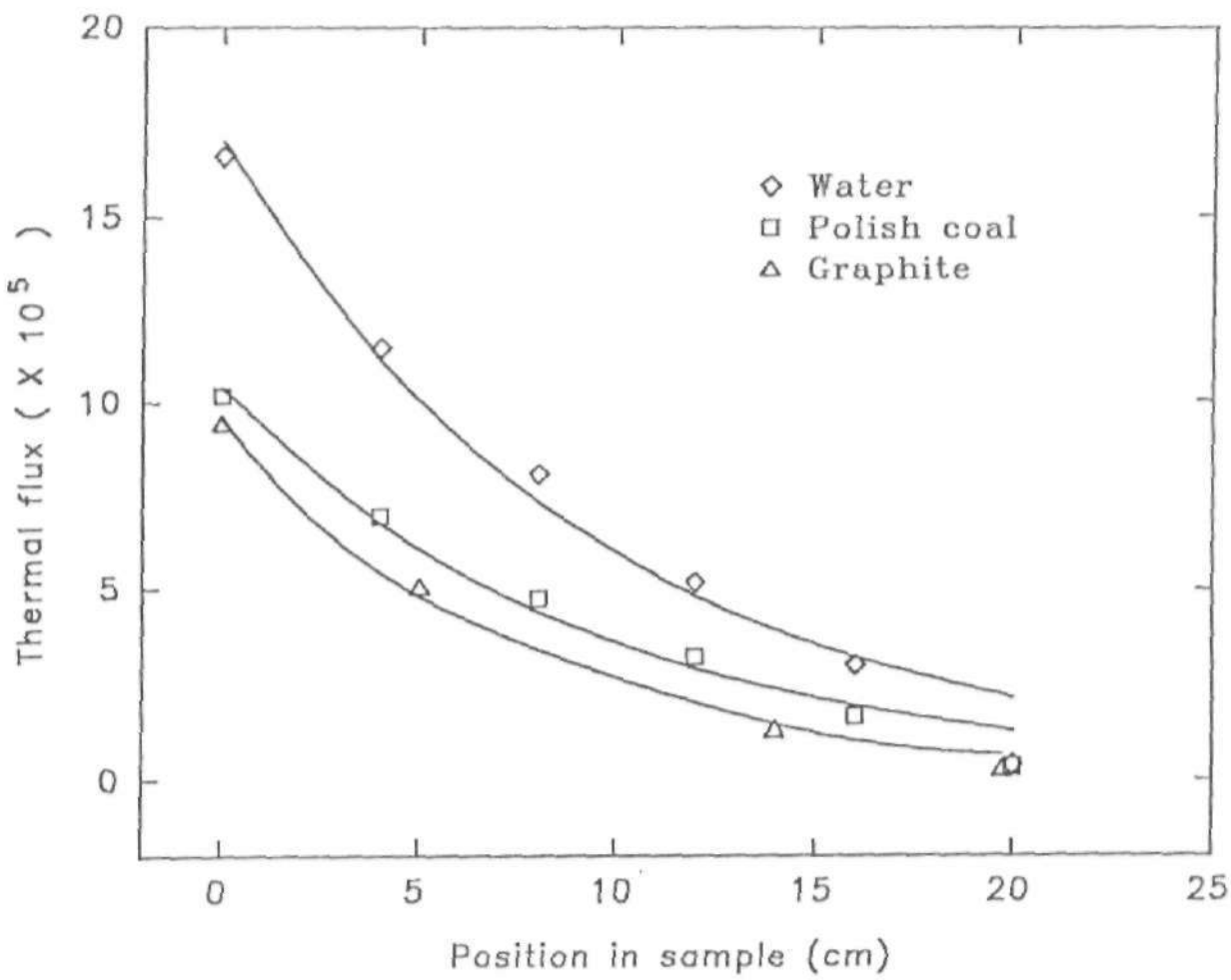


Fig. 5.7 Flux density distributions of thermal neutrons in the samples at different positions in the presence of 8 cm thick water moderator

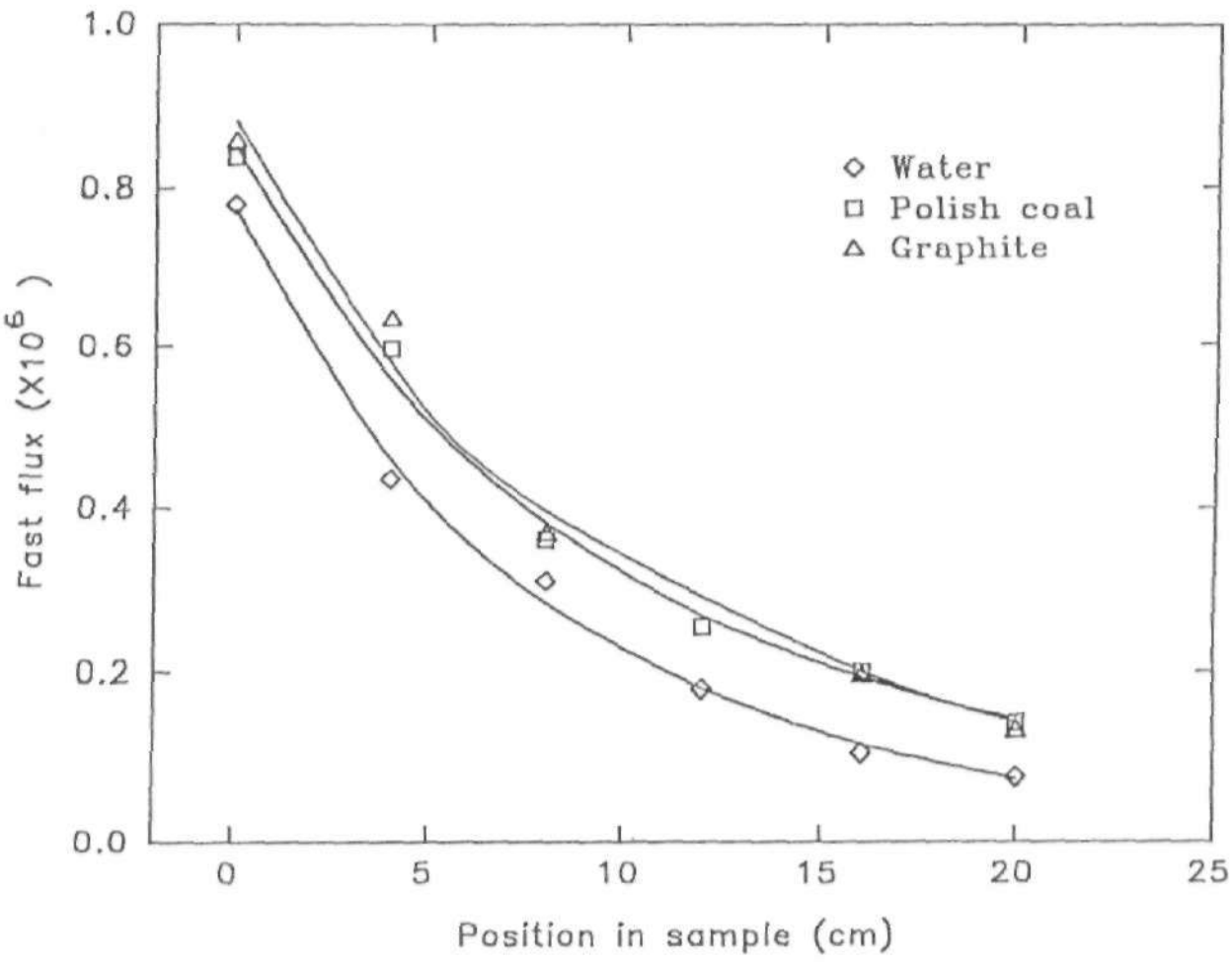


Fig. 5.8 Flux density distributions of fast neutrons in the samples at different positions in the presence of 8 cm thick water moderator

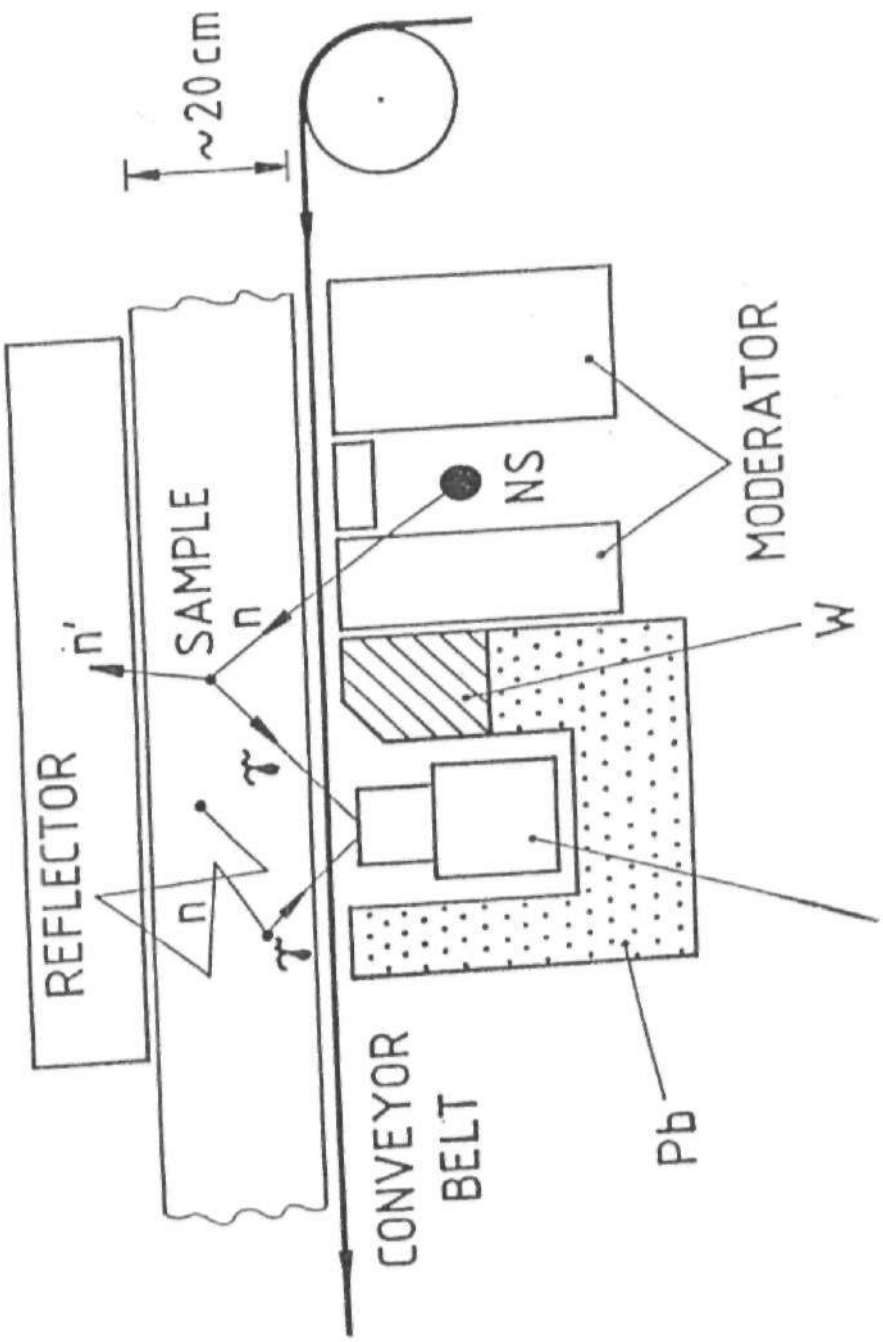


Fig. 5.9 The sheme of geometrical setup for on-line analysis of bulk samples

Consequently an M-S-R configuration with 20 cm as the maximum sample thickness shown in Figure 5.9 is proposed as an on-line analyzer of bulk samples.

5.3 Attenuation Characteristics of ^{252}Cf, Pu-Be and 14 MeV Neutrons Traversing Different Thicknesses of Bulk Samples

5.3.1 Experimental proceduers

The experimental arrangement shown in Figure 5.10 was used to determine the microscopic removal cross sections of 14 MeV neutrons in water, graphite and two types of coal samples. Similarly spectra of ^{252}Cf, ^{239}Pu-Be and 14 MeV neutrons traversing the different thicknesses of coal samples were measured using the same set-up. The PHRS system was used for spectra measurements while the data analysis was carried out with the ASEASYAS code. For these measurements the yields of ^{252}Cf and Pu-Be sources were 7×10^{6} n/s and 1.1×10^{7} n/s respectively while that of 14 MeV neutrons was monitored by an associated alpha particle detector (APM). The APM system consists of a surface barrier detector fed from a power supply and connected to computer-based multichannel analyzer via a pre-amplifier and a linear amplifier. As a result, the macroscopic removal cross sections (Σ_R) of 14 MeV neutrons in water, graphite and coal samples could be determined from the measured flux density (ϕ_f) using the following relation:

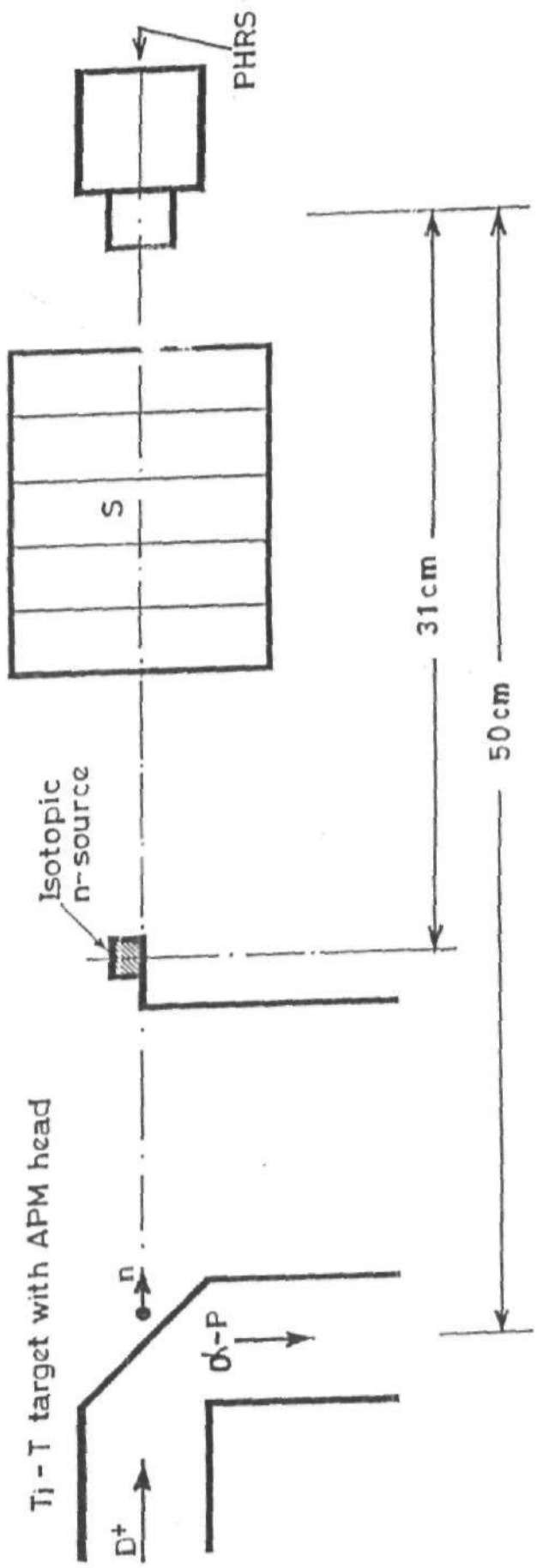


Fig. 5.10 The setup geometry for investigating the attenuation characteristics of ^{252}Cf, Pu-Be and D-T neutrons in different samples

$$\phi_f(r) = \frac{Y}{4\pi r^2} \; e^{-\Sigma_R (r - r_o)} \qquad 5.9$$

where, Y is source strength and $(r-r_o)$ is sample thickness.

5.3.2 Results and discussion

Results obtained using both relative net areas of the unfolded spectra and the pulse height distributions as a function of linear thickness are presented in Table 5.10. A semi-log plot of the relative flux density as a function of sample thickness is displayed in Figure 5.11. The macroscopic removal cross section values obtained for water, graphite and coal samples using 14 MeV neutrons are also given in Table 5.10. Uncertainties in the determination of Σ_R were found to be less than 10 % and were estimated mainly from the peak area determination as well as from the error in the bulk density of sample.

In Figures 5.12, 5.13 and 5.14 the spectral distributions of ^{252}Cf, Pu-Be and 14 MeV neutrons transmitted through slabs of coal determined by the PHRS system for thicknesses increasing in 4 cm steps form 0 to 20 cm are displayed respectively. As can be seen in the figures there are significant changes in the initial spectral shapes with increasing sample thickness due to high carbon content in the sample.

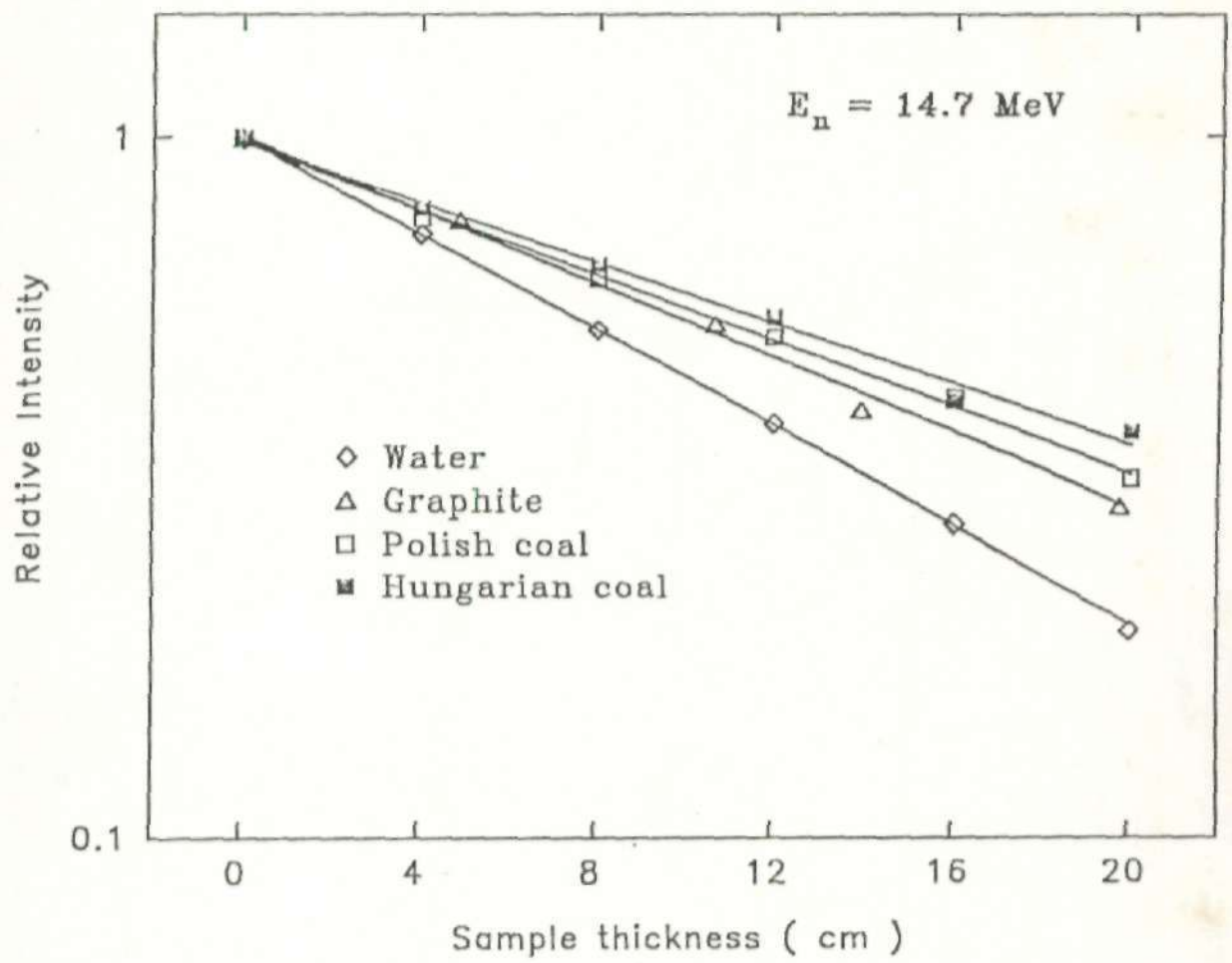


Fig. 5.11 A semi-log plot of relative peak areas of transmitted neutrons versus thickness for different bulk samples

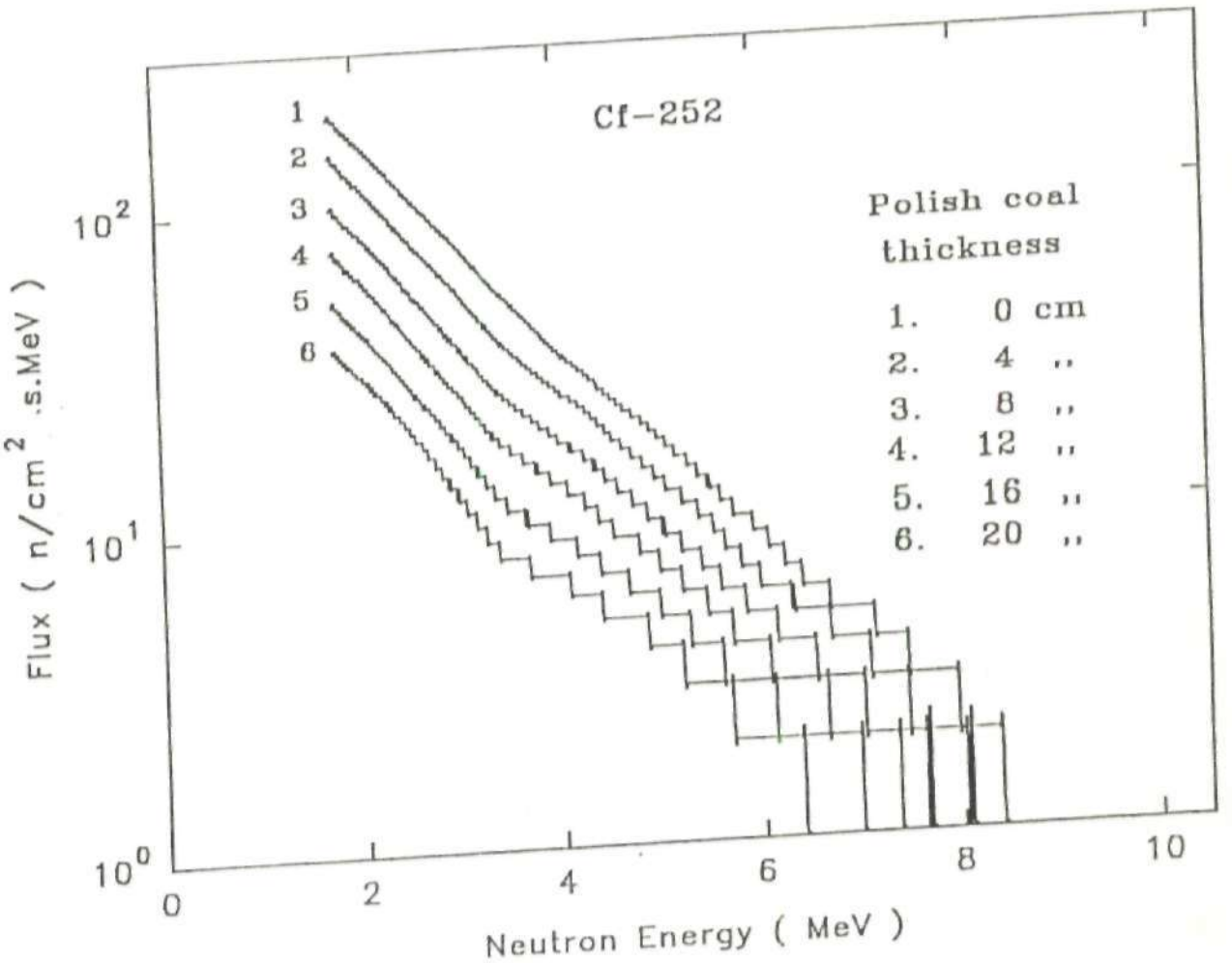


Fig. 5.12 Transmission spectra of ^{252}Cf neutrons for polish coal

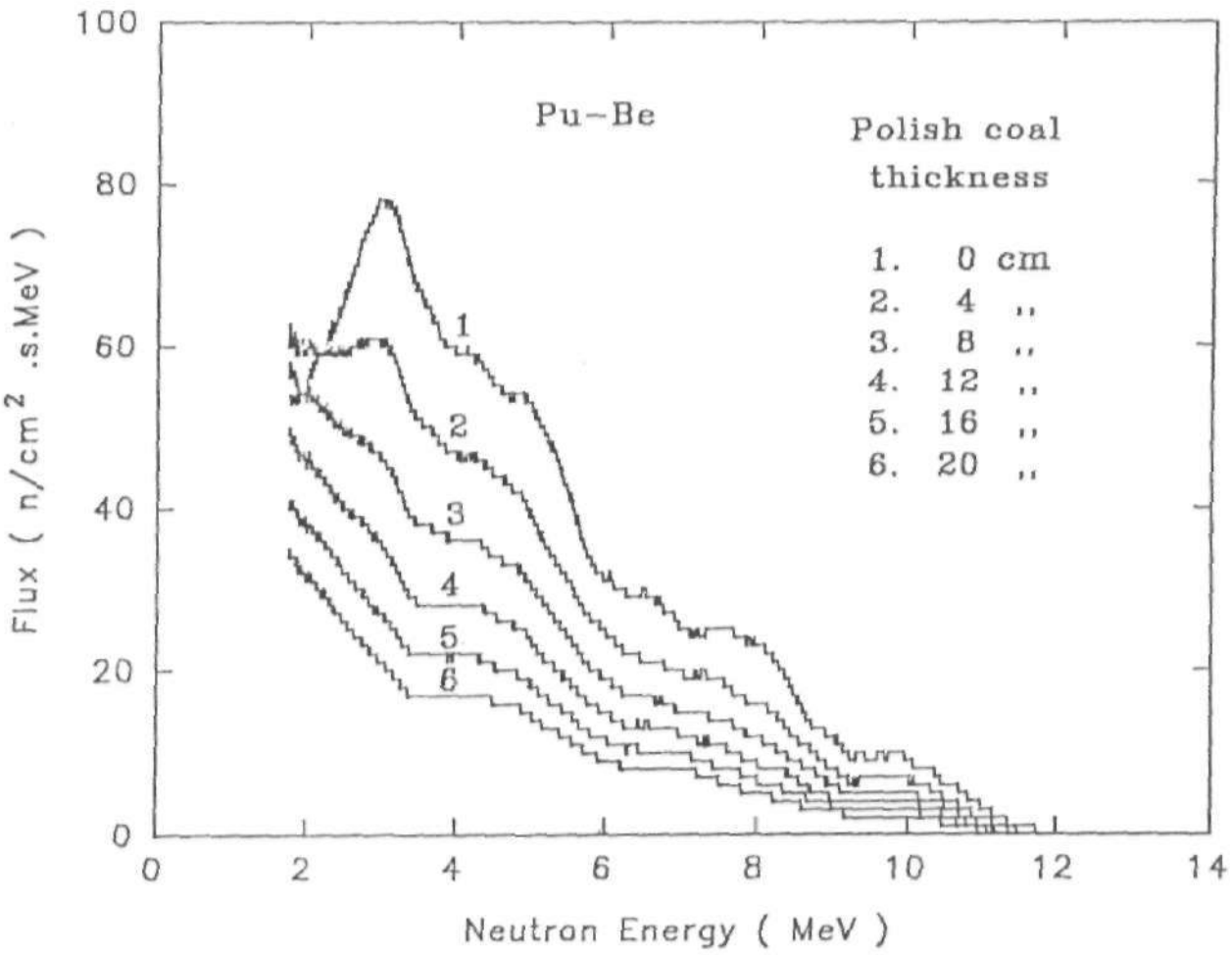


Fig. 5.13 Transmission spectra of Pu-Be neutrons for Polish coal

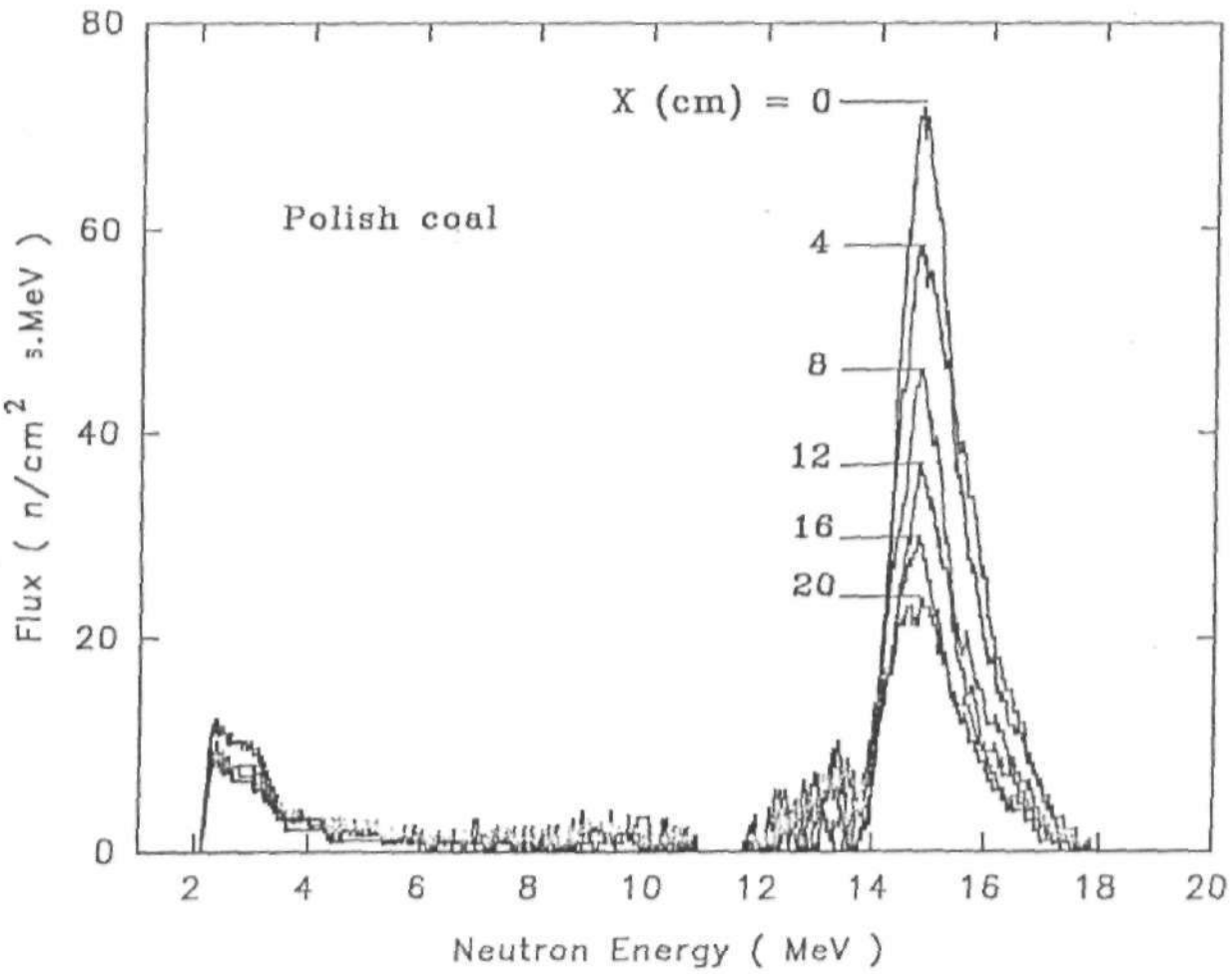


Fig. 5.14 Transmission spectra of D-T neutrons for Polish coal

Table 5.10 Measured relative peak areas of 14 MeV neutrons traversing different samples and deduced macroscopic removal cross sections for the samples

Sample thickness (cm)	Relative peak area			
	Polish coal	Hungarian coal	Water	Graphite
0	1.000	1.000	1.000	1.000
4	0.769	0.796	0.729	-
5	-	-	-	0.763
8	0.627	0.659	0.527	-
12	0.513	0.551	0.383	0.401
14	-	-	-	-
16	0.417	0.413	0.279	-
20	0.321	0.374	0.197	0.295
$\Sigma_R (cm^{-1})$	0.0556	0.0512	0.0802	0.0622
$\Delta\Sigma_R (cm^{-1})$	0.0043	0.0034	0.0078	0.0043

For the 14 MeV neutrons (Figure 5.14) the peak position remains unchanged but the values of the full width at half maximum (FWHM) increased with sample thickness. The structure in the total cross section of carbon (maxima at 3.5 and 7.75 MeV, minimum at 7 MeV) can be observed very well for Pu-Be neutrons (Figure 5.13). The flux density spectra of ^{252}Cf and Pu-Be sources for coal averaged over energy intervals of 0.2, 0.3 and 0.4 MeV in the (1.6 - 4.0), (4 - 7.9) and (7.9 - E_{max}) MeV ranges respectively rendered possible the determinations of fractions of neutron flux densities as functions of sample thicknesses

[*i.e.* $\bar{\phi}(X_i,E_i)$]. The data are normalized to that of the spectrum measured at zero sample thickness for ^{252}Cf and Pu-Be neutrons using the relation given below.

$$\bar{I}(X_i,E_i) = \bar{\phi}(X_i,E_i)\ \Delta E_i \Big/ \sum_{E_d}^{E_{max}} \bar{\phi}(E_i)\ \Delta E_i \qquad 5.10$$

where, $\bar{\phi}(X_i,E_i)$ and $\bar{\phi}(E_i)$ are the flux densities for $0 < X_i < X_o$ and $X_i = 0$ respectively while E_d refer to the detector threshold.

The normalized flux fractions of ^{252}Cf and Pu-Be neutrons traversing different thicknesses of coal sample are given in Tables 5.11 and 5.12. The relative integrated flux values for different threshold energies can be calculated from the equation given below.

$$\bar{I}(X,E_{ti})_{E_{ti}} = \sum^{E_{max}} \bar{\phi}(E_{ti})\ \Delta E_i \Big/ \sum_{E_d}^{E_{max}} \bar{\phi}(E_i)\ \Delta E_i \qquad 5.11$$

where, E_{ti} is the threshold energy of the i^{th} reaction while E_d is the detector threshold. The integrated flux densities above the (n,n'γ) reaction thresholds for ^{28}Si ^{12}C and ^{16}O (*i.e.* 1.78, 4.4 and 6.13 MeV) are shown in Figures 5.15 and 5.16 for ^{252}Cf and Pu-Be neutrons respectively. According to the figures the $\bar{I}(X,E_{ti})$ functions decreases exponentially with sample thickness and can be described by the following equation.

Table 5.11 Flux fraction of Cf-252 neutrons traversing different thicknesses of Polish coal

Energy range (MeV)	FRACTION					
	x=0cm	x=4cm	x=8cm	x=12cm	x=16cm	x=20cm
1.51 - 1.70	0.0452	0.0399	0.0271	0.0187	0.0133	0.0102
1.71 - 1.90	0.1324	0.0997	0.0694	0.0500	0.0347	0.0249
1.91 - 2.10	0.1160	0.0857	0.0598	0.0432	0.0300	0.0216
2.11 - 2.30	0.0996	0.0732	0.0508	0.0367	0.0255	0.0184
2.31 - 2.50	0.0852	0.0619	0.0428	0.0308	0.0214	0.0154
2.51 - 2.70	0.0725	0.0521	0.0360	0.0258	0.0177	0.0127
2.71 - 2.90	0.0620	0.0443	0.0304	0.0214	0.0147	0.0105
2.91 - 3.10	0.0529	0.0378	0.0257	0.0180	0.0123	0.0087
3.11 - 3.30	0.0446	0.0318	0.0215	0.0149	0.0101	0.0072
3.31 - 3.50	0.0380	0.0270	0.0182	0.0127	0.0086	0.0060
3.51 - 3.70	0.0328	0.0234	0.0159	0.0113	0.0077	0.0057
3.71 - 3.90	0.0281	0.0204	0.0141	0.0103	0.0071	0.0050
3.91 - 4.10	0.0242	0.0180	0.0125	0.0092	0.0065	0.0050
4.11 - 4.40	0.0323	0.0243	0.0172	0.0128	0.0092	0.0067
4.41 - 4.70	0.0249	0.0187	0.0137	0.0101	0.0074	0.0054
4.71 - 5.00	0.0206	0.0154	0.0115	0.0088	0.0064	0.0049
5.01 - 5.30	0.0168	0.0128	0.0094	0.0072	0.0053	0.0039
5.31 - 5.60	0.0139	0.0108	0.0079	0.0059	0.0043	0.0032
5.61 - 5.90	0.0112	0.0084	0.0062	0.0047	0.0032	0.0025
5.91 - 6.20	0.0093	0.0068	0.0052	0.0038	0.0029	0.0022
6.21 - 6.50	0.0073	0.0057	0.0043	0.0032	0.0022	0.0017
6.51 - 6.80	0.0060	0.0049	0.0033	0.0026	0.0022	0.0011
6.81 - 7.10	0.0054	0.0042	0.0029	0.0022	0.0017	0.0011
7.11 - 7.40	0.0044	0.0032	0.0022	0.0020	0.0011	0.0011
7.41 - 7.70	0.0034	0.0023	0.0019	0.0011	0.0011	0.0003
7.71 - 8.00	0.0031	0.0022	0.0011	0.0011	0.0003	0.0000
8.01 - 8.40	0.0028	0.0016	0.0014	0.0010	0.0000	0.0000
8.41 - 8.80	0.0014	0.0014	0.0014	0.0000	0.0000	0.0000
8.81 - 9.20	0.0014	0.0014	0.0004	0.0000	0.0000	0.0000
9.21 - 9.60	0.0014	0.0009	0.0000	0.0000	0.0000	0.0000
9.61 - 10.00	0.0011	0.0000	0.0000	0.0000	0.0000	0.0000
10.01 - 10.40	0.0000	0.0000	0.0000	0.0000	0.0000	0.0000
Sum =	1.0000	0.7403	0.5144	0.3694	0.2569	0.1852

Table 5.12 Flux fraction of Pu-Be neutrons traversing different thicknesses of Polish coal.

Energy range (MeV)	FRACTION					
	x=0cm	x=4cm	x=8cm	x=12cm	x=16cm	x=20cm
1.60 - 1.80	0.0181	0.0238	0.0214	0.0190	0.0165	0.0137
1.80 - 2.00	0.0322	0.0357	0.0327	0.0280	0.0231	0.0195
2.01 - 2.20	0.0346	0.0358	0.0318	0.0268	0.0220	0.0183
2.21 - 2.40	0.0370	0.0355	0.0306	0.0253	0.0206	0.0169
2.41 - 2.60	0.0397	0.0355	0.0296	0.0239	0.0190	0.0154
2.61 - 2.80	0.0431	0.0360	0.0289	0.0230	0.0178	0.0142
2.81 - 3.00	0.0458	0.0363	0.0280	0.0218	0.0164	0.0130
3.01 - 3.20	0.0457	0.0353	0.0266	0.0201	0.0152	0.0119
3.21 - 3.40	0.0425	0.0323	0.0242	0.0181	0.0137	0.0107
3.41 - 3.60	0.0396	0.0303	0.0227	0.0169	0.0131	0.0101
3.61 - 3.80	0.0374	0.0292	0.0222	0.0167	0.0131	0.0101
3.81 - 4.00	0.0357	0.0281	0.0216	0.0167	0.0130	0.0101
4.01 - 4.30	0.0526	0.0415	0.0322	0.0250	0.0196	0.0152
4.31 - 4.60	0.0499	0.0399	0.0307	0.0240	0.0185	0.0148
4.61 - 4.90	0.0481	0.0378	0.0292	0.0228	0.0175	0.0141
4.91 - 5.20	0.0457	0.0336	0.0264	0.0203	0.0159	0.0126
5.21 - 5.50	0.0402	0.0292	0.0229	0.0178	0.0139	0.0112
5.51 - 5.80	0.0327	0.0251	0.0195	0.0153	0.0119	0.0096
5.81 - 6.10	0.0282	0.0223	0.0172	0.0135	0.0104	0.0083
6.11 - 6.40	0.0263	0.0200	0.0155	0.0120	0.0098	0.0074
6.41 - 6.70	0.0260	0.0189	0.0150	0.0119	0.0090	0.0071
6.71 - 7.00	0.0238	0.0181	0.0141	0.0115	0.0089	0.0071
7.01 - 7.30	0.0219	0.0173	0.0134	0.0105	0.0084	0.0068
7.31 - 7.60	0.0223	0.0169	0.0127	0.0099	0.0074	0.0059
7.61 - 7.90	0.0216	0.0152	0.0117	0.0086	0.0067	0.0050
7.91 - 8.30	0.0264	0.0184	0.0134	0.0098	0.0074	0.0057
8.31 - 8.70	0.0201	0.0143	0.0106	0.0081	0.0058	0.0044
8.71 - 9.10	0.0146	0.0102	0.0079	0.0055	0.0043	0.0036
9.11 - 9.50	0.0114	0.0080	0.0060	0.0048	0.0036	0.0025
9.51 - 9.90	0.0116	0.0083	0.0060	0.0048	0.0036	0.0024
9.91 - 10.30	0.0101	0.0075	0.0055	0.0043	0.0032	0.0024
10.31 - 10.70	0.0077	0.0052	0.0041	0.0029	0.0022	0.0016
10.71 - 11.10	0.0047	0.0029	0.0019	0.0015	0.0011	0.0008
11.11 - 11.50	0.0021	0.0013	0.0008	0.0002	0.0000	0.0000
11.51 - 11.90	0.0007	0.0000	0.0000	0.0000	0.0000	0.0000
11.91 - 12.30	0.0000	0.0000	0.0000	0.0000	0.0000	0.0000
Sum =	1.0000	0.8054	0.6367	0.5011	0.3926	0.3126

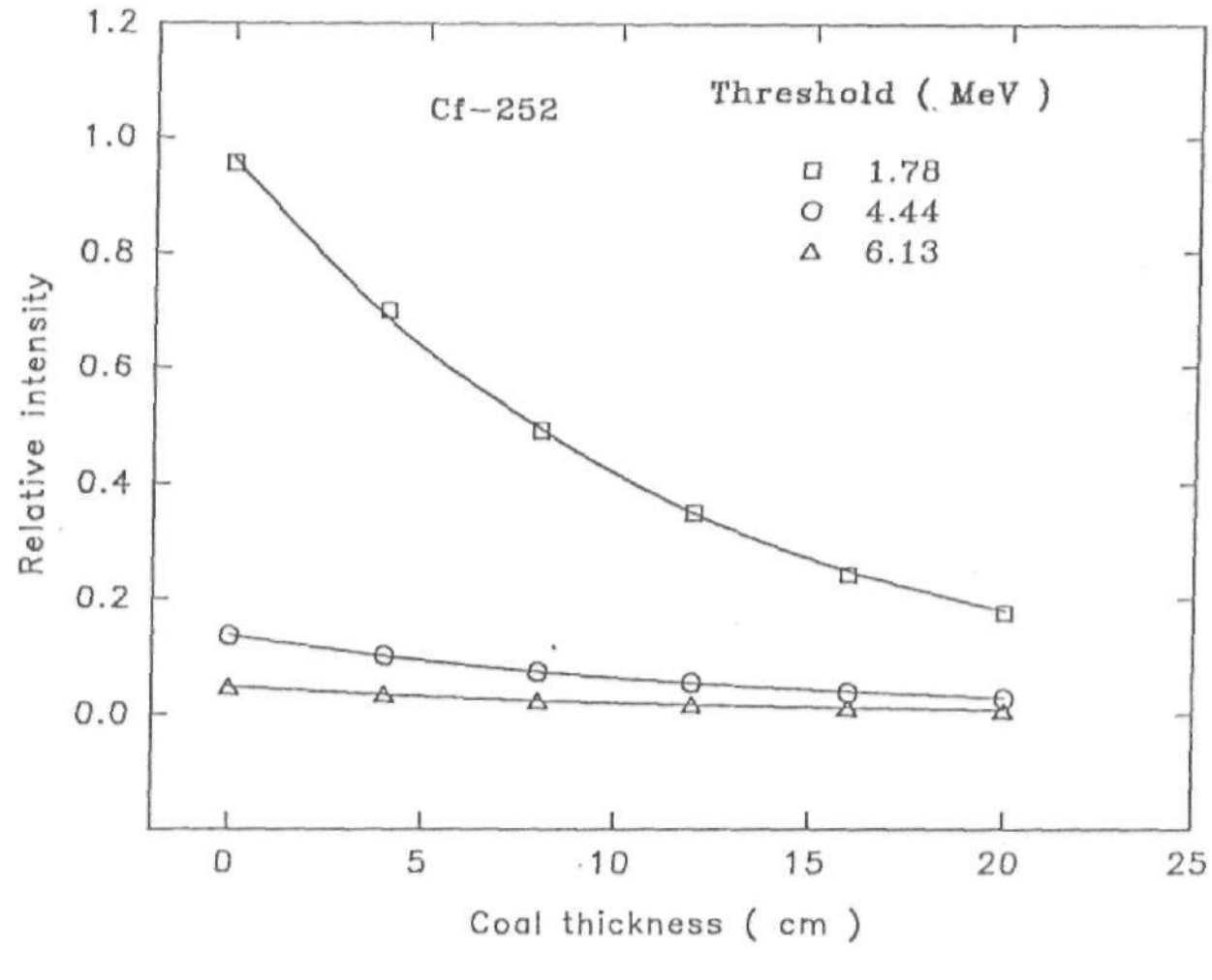


Fig. 5.15 Spectrum averaged flux densities of ^{252}Cf neutrons as a function of coal thickness

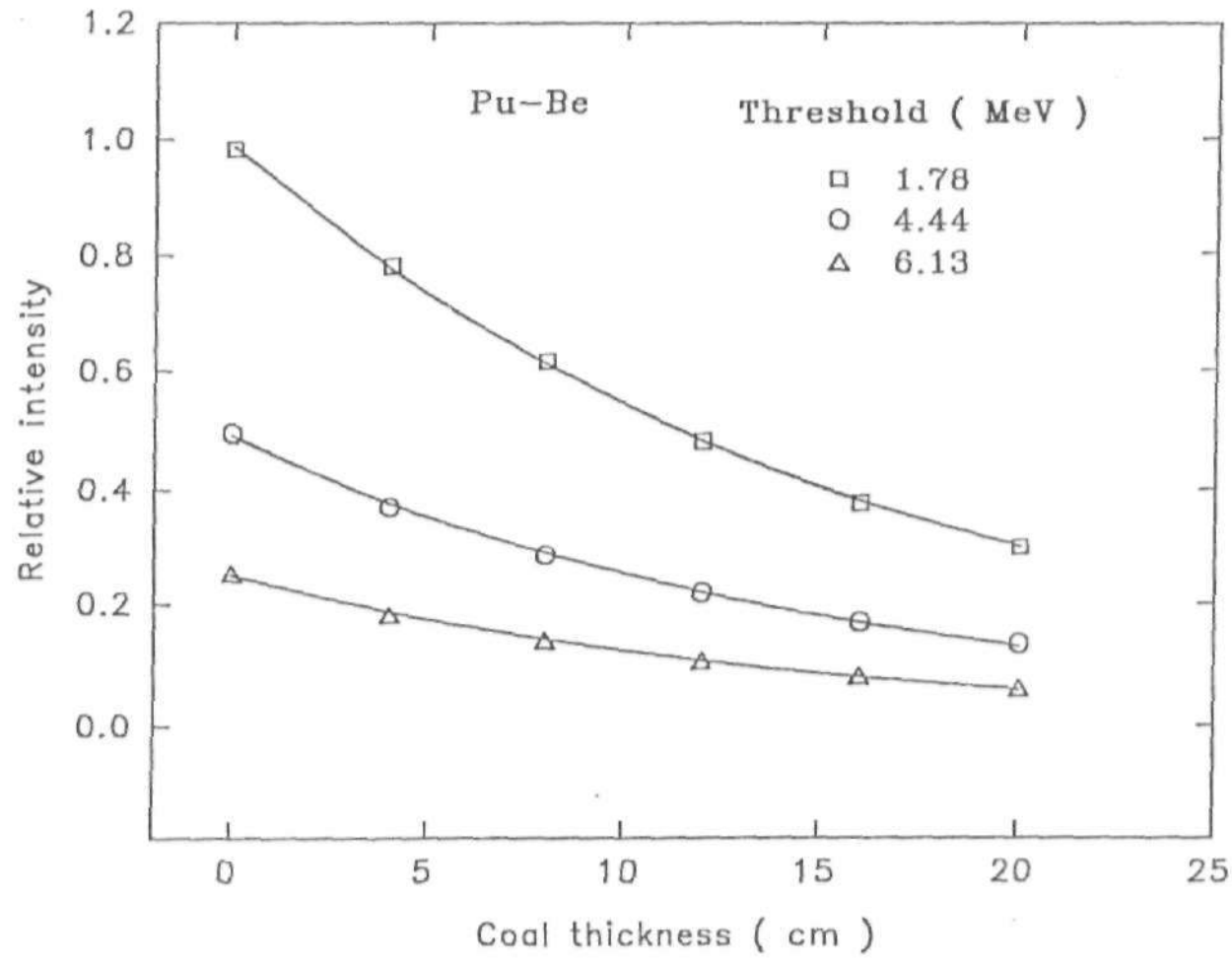


Fig. 5.16 Spectrum averaged flux densities of Pu-Be neutrons as a function thickness for coal

$$\bar{I}(X,E_{ti}) = \bar{I}(E_i)\, e^{-\Sigma_{R(ti)}X} \qquad 5.12$$

where, $\bar{I}(E_{ti})$ is the normalized integrated flux density value at zero thickness of sample and $\Sigma_{R(ti)}$ is attenuation parameter deduced from the spectrum averaged flux densities for different $(n,n'\gamma)$ reaction thresholds. The values of $\Sigma_{R(ti)}$ obtained from a semi-log plot of $\bar{I}(X,E_{ti})$ as a function of sample thickness together with the $\bar{I}(E_{ti})$ are ^{252}Cf and Pu-Be neutrons are given in Table 5.13. As can be seen in Figure 5.15 the ^{252}Cf neutrons are suitable for the detection of Si only by the (n,n',γ) reaction.

Table 5.13 Attenuation parameter $[\Sigma_R(E_{ti})]$ values deduced from the spectrum averaged flux densities for different $(n,n'\gamma)$ reaction thresholds as a function of coal thickness using ^{252}Cf and Pu-Be neutron sources

Threshold energy (MeV)	1.78	4.44	6.13
Eq.(5.12): Pu-Be $\Sigma_R(E_{ti})$	0.595±1%	0.0670±2%	0.0709±3%
Eq.(5.12):^{252}Cf $\Sigma_R(E_{ti})$	0.084±1%	0.0779±2%	0.0869±2%
Eq.(5.12): Pu-Be $\bar{I}(E_{ti})$	0.986	0.491	0.248
Eq.(5.12):^{252}Cf $\bar{I}(E_{ti})$	0.962	0.135	0.048

The ϕ(E) data given in Tables 5.11 and 5.12 can be used to determine the reaction rates [*i.e.* R(E) = σ(E).ϕ(e)] provided the cross section curve of the given reaction is well known. Consequently the total gamma yield for a given reaction and sample thickness can be deduced.

CHAPTER SIX

6.0 TOTAL HYDROGEN CONTENT AND THE CARBON/HYDROGEN ATOMIC RATIO IN OIL SAMPLES BY THE THERMAL NEUTRON REFLECTION TECHNIQUE

6.1 Introduction

The knowledge of total hydrogen content and O+C/H ratio in hydrocarbons is a very important means of establishing their structure and purity. Since oil is built primarily from carbon and hydrogen, the quality of crude oils and some of their by-products can also be determined from the knowledge of these quantities. The usual chemical methods of determining hydrogen contents in oil samples entail long hours of analyses as well as heating of up to 1000°C. Consequently the use of a nuclear analytical technique which is fast and non-destructive for this purpose is indispensable. The thermal neutron reflection technique developed by Buczko *et al.*, (1975) for the on-line determination of bitumen content in asphalt concrete have been adapted by several investigators for related investigations (Al-jobori *et al.*, 1978; Csikai *et al.*, 1982; Szegedi *et al.*, 1982; Szegedi *et al.*, 1990 and Chimoye 1991). In those investigations, the geometrical setup designed for a road construction company was used for the analysis of different bulk materials.

However in this chapter, an improved experimental arrangement for which a better count rate response was achieved has been developed. In addition to this, a reproducibility of 0.15 w % was obtained with the present setup in comparison with a value of 0.3 W % achieved using the previous arrangement. The total hydrogen content and O+C/H ratio in some household and motor oil samples as well as crude oil samples from Nigeria and Hungary were determined. The basic principles of the thermal neutron reflection method as well as the modified geometrical arrangement adopted for the present investigation have been described in chapter 2.

6.2 Experimental Procedures

In the improved experimental arrangement shown in Figure 2.10, neutrons of energies above the thermal region are produced by a Pu-Be neutron source of yield 10^6 n/s embedded in a cylindrical polyamide moderator. The sensitive length of the BF_3 detector placed on the surface of the moderator is comparable with the diameter of sample holder. The signal-to-background ratio was enhanced by covering the detector with 0.9 mm thick Cd sheet on the side facing the moderator. With this arrangement, it was ensured that the thermal neutrons reaching the detector are produced mainly by the sample in a holder of volume 500 cm^3 or less. The relative excess count rate normalized to the sample density, ρ, depends on the hydrogen content and is

given by the expression given in equation 2.60.

Hydrocarbons in liquid form and graphite powder containing well known hydrogen and carbon contents are used as standards to determine the calibration lines shown in Figures 6.1 and 6.2. The measured η values belonging to the standards using 300 cm^3 sample holder are presented in Table 6.1.

Table 6.1 Parameters of standard samples used for the determination of the calibration curves

Standard	ρ (g/cm^3)	η	H (w %)	O+C/H
C + 0 w% H_2O	0.883	0.264	0.000	-
C + 5 w% H_2O	0.770	0.370	0.550	178.000
C + 10 w% H_2O	0.690	0.490	1.100	89.000
C + 15 w% H_2O	0.696	0.600	1.660	58.000
C + 20 w%$_2$H O	0.773	0.690	2.220	43.000
C_7H_8O	1.050	1.547	7.410	12.500
C_6H_6	0.879	1.663	7.692	12.000
C_7H_8	0.867	1.784	8.696	10.500
C_8H_{10}	0.866	1.899	9.434	9.600
H_2O	1.000	2.142	11.110	8.000
$C_4H_{10}O$	0.789	2.661	13.514	6.400
C_7H_{16}	0.684	3.040	16.000	5.250

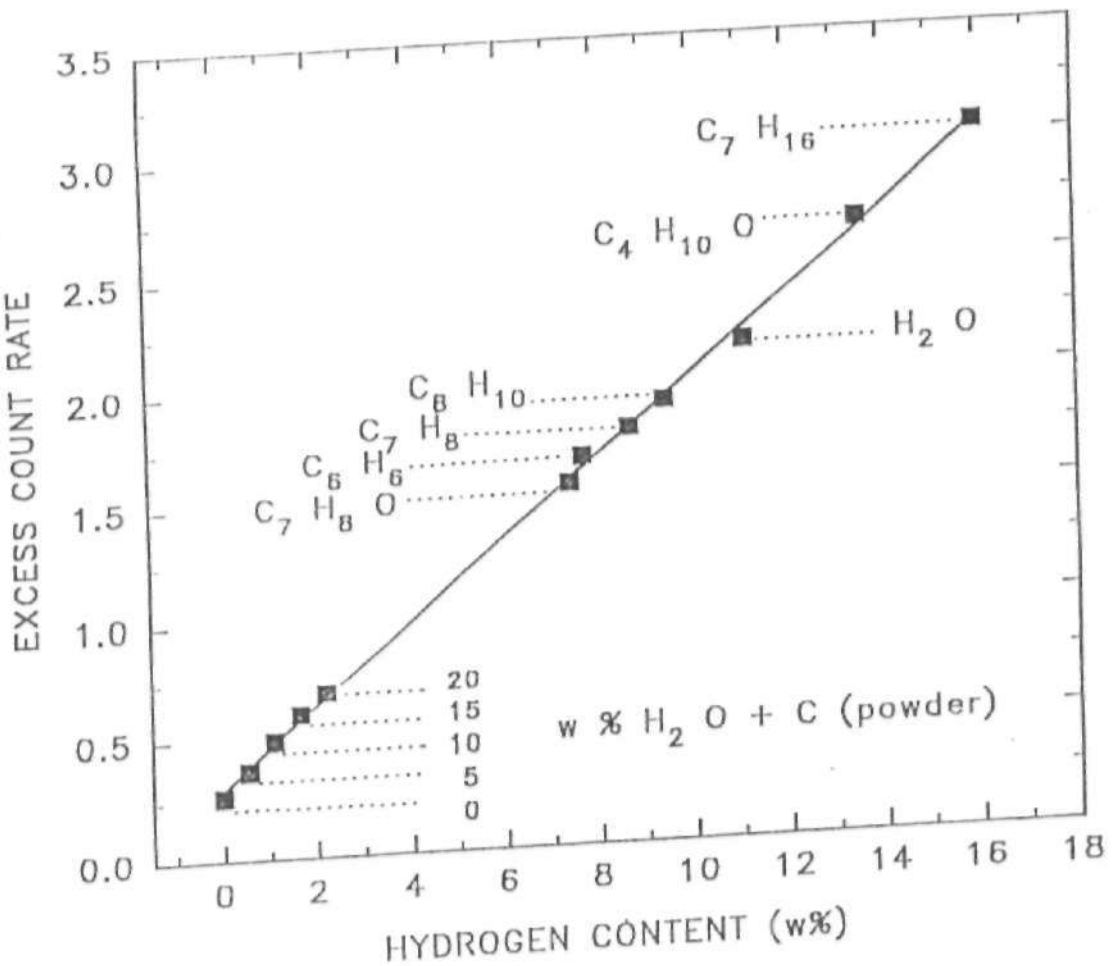


Fig. 6.1 Calibration line used for the determination of total hydrogen content in oil samples

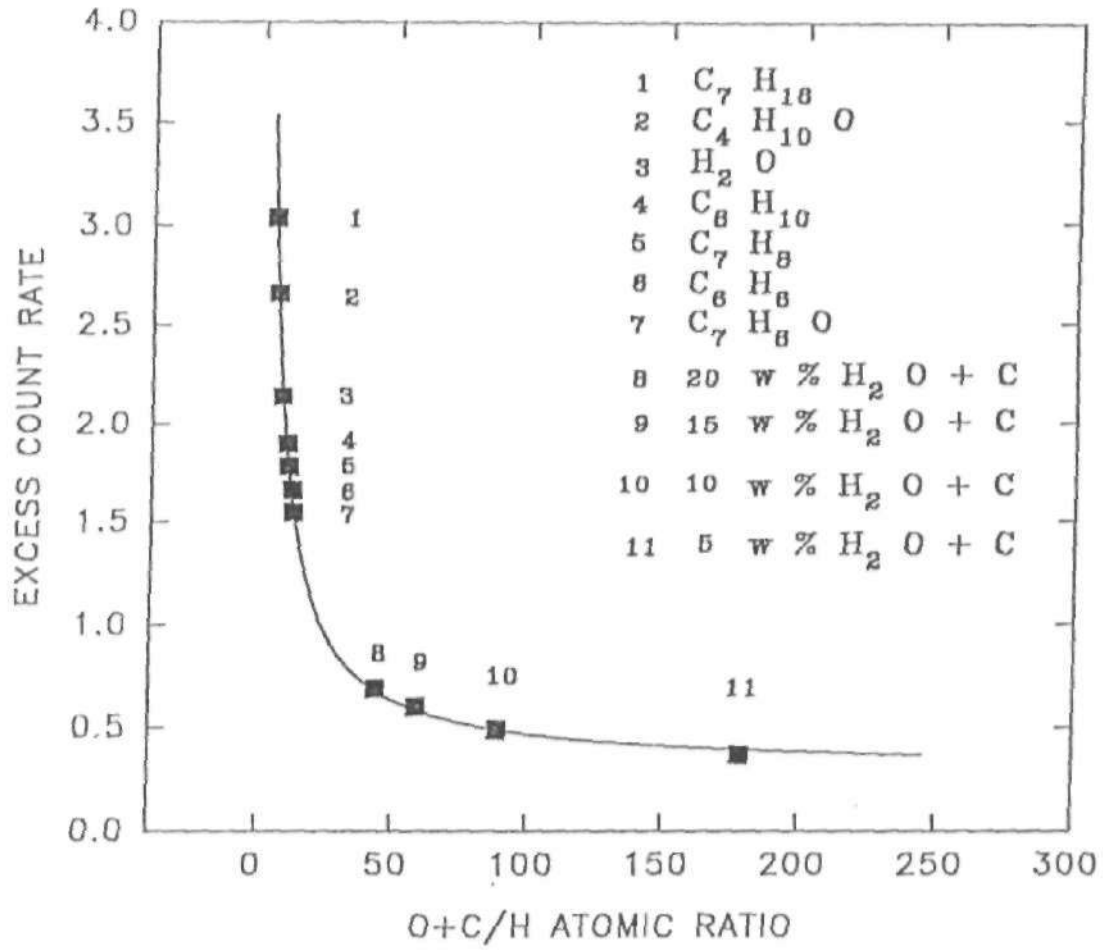


Fig. 6.2 Calibration line used for the determination of O+C/H ratio in oil samples

6.3 Results and Discussion

The solid lines in Figures 6.1 and 6.2 for the determination of total H content and O+C/H atomicratio were fitted by equations 6.1 and 6.2 respectively.

$$\eta = \eta_o + m.H \ (w\%) \qquad 6.1$$

$$\eta = A_o + A_1.X^{-1} + A_2.X^{-2} \qquad 6.2$$

where, η_o = 0.286349 representing the matrix effect and

$m = 0.172 \pm 0.012$ is the slope of the calibration line for H determination.

In equation 6.2,

X represents the O+C/H atomic ratio while for A_o, A_1 and A_2 fitting parameters, the following values, 0.3005, 16.7441 and -12.2251 were obtained for the determination of O+C/H atomic ratio in the given measuring setup.

Measured excess count rates together with the deduced total H content and O+C/H ratio in the samples are given in Table 6.2. Results show that the average H content in crude oil samples from Hungarian sources is slightly higher than in crude oil samples of Nigerian origin. The determination of C/H ratio to a large extent depends on the presence O in the sample because of the closeness in the mass numbers of C and O. An independent method via the $^{16}O(n,p)^{16}N$ reaction is therefore recommended for the determination of O_2 especially in crude oils. A standard error in the

determination of total H content and the O+C/H atomic ratio was found to be ± 1% .

Table 6.2 Measured data and the deduced H and O+C/H in samples

Sample	ρ (g/cm^3)	η	H w %	O+C/H ratio
Motor Oil:				
Petrol	0.730	2.635	13.62	6.35
Lubricant 1	0.846	2.685	13.91	6.19
Lubricant 2	0.856	2.572	13.26	6.55
Lubricant 3	0.856	2.559	13.18	6.59
Lubricant 4	0.856	2.544	13.10	6.64
Lubricant 5	0.856	2.562	13.20	6.58
Crude oil:				
RDC1 (NIG.)	0.830	2.560	13.19	6.59
RDC2 ,,	0.885	2.420	12.37	7.09
RDC3 ,,	0.840	2.590	13.36	6.49
RDC4 ,,	0.864	2.510	12.89	6.76
RDC5 ,,	0.851	2.560	13.19	6.59
RDC6 ,,	0.863	2.550	13.13	6.62
RDC7 ,,	0.895	2.450	12.55	6.97
Dony (HUN.)	0.860	2.490	12.78	6.83
Kaba D-II ,,	0.826	2.651	13.71	6.30
Household oil:				
Castor-oil	0.930	2.276	11.54	7.69
Olive-oil	0.876	2.430	12.43	7.05
Maize-oil	0.896	2.333	11.87	7.43
Sunflower oil	0.890	2.297	11.66	7.58
Cooking-oil (commercial)	0.896	2.325	11.82	7.46
Paraffin-oil	0.830	2.700	13.99	6.13

CHAPTER SEVEN

7.0 SUMMARY, CONCLUSION AND RECOMMENDATION

7.1 Summary and Conclusion

Neutrons produced by isotopic and accelerator-based neutron sources were used to carry out experimental investigations in the fields of neutron data measurements and bulk sample analysis. In the first part of the work which was devoted to neutron data measurements, excitation function and isomeric cross section ratio of $^{58}Ni(n,p)^{58}Co^{m,g}$ reaction were determined from 5 to 15 MeV neutron energy. The investigation was carried out as a result of the discrepancies observed in the cross section curves and isomeric cross section ratio data especially in the 5-13 MeV energy region. In the second part, characteristics data of neutron interactions with bulk samples were investigated with the following aims: 1) to develop an on-line analytical geometry for the analysis of bulk minerals based on the thermal and fast neutron flux density distributions; 2) to improve the experimental setup based on the thermal neutron reflection technique so as to achieve a lower limit of detection for the determination of H_2 in oil samples.

7.1.1 Excitation function and cross section ratio of $^{58}Ni(n,p)^{58}Co^{m,g}$ reaction from 5 to 15 MeV

Irradiations were performed with neutrons produced via the D-T and D-D reactions by a neutron generator and a cyclotron respectively. Spectral distribution of incident neutrons of energies between 5 and 13 MeV were measured by the PHRS and validated by the activation unfolding technique in order to minimize total measurement error. Similarly, the angular energy distribution of incident neutrons around 14 MeV energy region were determined by the activation of threshold energy monitors. Results of the isomeric cross section ratio as a function of energy measured for the first time made it possible to determine the cross section curve for the formation of metastable state. In addition to this, the good agreement between the present measurement and calculated cross section curves render possible the selection of the most probable data especially in the 5-13 MeV neutron energy region where the literature data are discrepant and scanty.

7.1.2 Characteristics data of neutron interactions

Thermal and fast neutron flux distributions in slabs of bulk materials together with the attenuation characteristics of ^{252}Cf, Pu-Be and D-T neutrons traversing different thicknesses of coal, water and graphite samples were investigated. Based on the results of these

measurements, an experimental setup for the on-line elemental analysis of minerals as well as a data base for checking different models were obtained. Furthermore, the sensitivity of the experimental setup based on the thermal neutron reflection technique was improved from 0.3 w % to 0.12 w % following a modification of the setup. The improved setup was used to measure total hydrogen content and the O+C/H atomic ratio in household and motor oils as well as crude oil samples from Hungary and Nigeria.

7.2 Recommendation

Results of the cross section data presented in this work in comparison with the calculational results justifies the need to determine the characteristics of incident neutrons employed in cross section measurements. However, more measurements are needed to ascertain the cross section curves at around 2 MeV neutron energy region where the isomeric cross section ratio as function of neutron energy was seen to exhibit a minimum.

Similarly, further investigations are required to test the analytical setup recommended for use as an on-line analyzer of bulk minerals. The possible use of the analyzer for non-destructive testing of cargoes for explosives and hidden drugs also need to be established. The adaptation of the neutron reflection method for checking the adulteration of petroleum products and related materials is recommended bearing further investigations.

REFERENCES

Al-Jobori, S.M., Szegedi, S., and Buczko, Cs.M., (1978). Determination of hydrogen content in crude oil by the neutron reflection method. *Radiochem. Radioanal. Lett.* 33, pp. 133.

Avrigeanu, V., Hodgson, P.E. and Avrigeanu, M. (1994). Global optical potential for emitted alpha particles. *Phys. Rev. C* 49, pp. 2136.

Bahal, B.M. and Pepelnik, R. (1984). Cross section measurements of Cr, Mn, Fe, Co, and Ni for an accurate determination of these elements in natural and synthetic samples using a 14 MeV neutron generator. *REPORT*, GKSS-84-E.

Barschall, H.H. (1983). 14 MeV D-T sources. *In:* Cierjacks, S. (Ed.) *Neutron Sources for Basic Physics and Applications.* An OECD/NEA REPORT Pergamon Press Ltd. Oxford Vol. 2, pp. 57.

Berkurts, K.H. and Wirtz, K. (1964). *Neutron Physics.* Springer-Verlag, New York, pp. 23.

Buczko, M., Dezso, Z. and Csikai, J. (1975). Determination of bitumen content in asphalt concrete using a neutron reflection technique. *J. Radioanal. Chem.* 25, pp. 179.

Burcham, W.E. (1963) *An Introduction to Nuclear Physics.* Longmans London, pp. 157.

Cabral, S., Borker, B., Klein, H. and Mannhart, W. (1990). Neutron production from deuteron breakup reaction on deuterium, *Nucl. Sci. and Engr.*, 106, pp. 308.

Chimoye, T. (1991) Determination of water in zeolites by a neutron reflection method, *Nucl. Chem. Lett.*, 154, pp. 393.

Cierjacks, S. (Ed.) (1983) *Neutron Sources for Basic Physics and Applications.* an OECD/NEA REPORT, Pergamon Press Ltd., Oxford Vol. 2, pp. 3.

CINDA-94 (1988-1994). *The Index to Literature and Computer Files on Microscopic Data.* (IAEA, Vienna) 1994.

Clayton, C.G. and Wormald, M.R. (1983). Coal analysis by nuclear methods, *Int. J. Appl. Radioact. Isot.*, 34, pp. 3.

Cross, W.G., Clarce, R.L., Morin, K., Slinn, G., Ahmad, N.M. and Beg, K. (1963). Activation cross sections of Fe and Ni isotopes for 14.5 MeV neutrons, *EANDC (CAN)-16*, pp.1.

Csikai, J. (1987). *Handbook of Fast Neutron Generators Vol. I.* CRC Press Inc. Florida. Inc. Florida. pp.18.

Csikai, J. (1989). Utilization of intense neutron generators in science and technology. *Nucl. Instr. Meth., A* 280, pp. 233.

Csikai, J. Al-Jobori, S.M., Buczko, Cs.M. and Szegedi, S. (1982). Determination of major and trace elements in crude oils by neutron activation and reflection methods. *J. Radioanal. Chem* 71 pp. 215

Csikai, J., Lantos, Zs. and Buczko, Cs.M. (1986). Advisory Group Meeting on properties of D-D and D-T neutron sources. *REPORT* IAEA-TECDOC-400 Leningrad, USSR June 9-13, 1986, pp. 296, IAEA, Vienna.

Csikai, J., Buczko, Cs.M., Pepelnik, R. and Agrawal, H.M. (1991). Activation cross sections related to nuclear heating of high T superconductors. *Ann. Nucl. Energy* 18, pp. 1.

Curtiss, L.F. (1959). *Introduction to Neutron physics*. D. Van Nostand Company, Inc. Princeton, New Jersey, pp 2.

Daroczy, S. and Raics, P. (1982). Measurement of the yield of short-lived fission products by direct Ge(Li) method. *In:* Laboratory manual of IAEA training course on utilization of neutron generators, Debrecen, Hungary. pp. 69.

Day, N. (Ed.), (1981) WRENDA 81/82, INDC(SEC)-78/URSF, IAEA, Vienna.

Decowski, P., Grochulski, W., Marcinkowski, A., Siwek, K., Sledzinsta,I. and Wilhelmi, Z. (1968). Isomeric Cross section ratios and total cross sections for the $^{59}Co(n,2n)^{58g,m}Co$, $^{58}Ni(n,p)^{58g,m}Co$ and $^{59}Co(n,\gamma)^{58g,m}Co$ reactions. *Nucl. Phys. A* 112, pp. 513.

Derbertin, K., and Helmer, R. G. (1988). *Gamma and X-ray Spectometry with Semi conductor Detectors.* North-Holland-Elsevier, New York. pp. 205.

Drosg, M. and Schewerer, O. (1987). Production of monoenergetic neutrons between 0.1 and 23 MeV neutron energies and cross sections. *In:* Handbook on Nuclear Activation Data. An *IAEA TECHNICAl REPORT SERIES* 273, pp. 83.

Duffey, D., EL-Kady, A., and Senfle, F.E., (1970). Analytical sensitivities and energies of thermal-neutron capture gamma rays, *Nucl. Instr.and Meth.* 80, pp. 149.

ENDF/B-V1 (1990). Lemmel H.D. (Ed.). *REPORT IAEA-NDS-100*, Rev. 3 IAEA, Vienna.3 IAEA.

ENDL/A (1978). Lawrence Livermore National Laboratory *REPORT UCRL 50400*, Vol. pp.18, 17 Oct. 1978.

Freye, T., Lorentz-Wirzba, H., Cleff, B., Tranvetter, H.P. and Rolfs, G. (1977) Voltage calibration of low-energy accelerators, *Z. Phys. A* 281, pp. 211.

Gallert, A., Csikai, J., Qaim, S.M. and Kneiper, J. (1993). Recommended target materials for D-D neutrons. *Nucl. Instr. and Meth. A*334, pp. 154.

Gallert, A., Csikai, J. and Qaim, S.M. (1994). Improved gas-cell D-D neutron sources. *Nucl. Instr. and Meth. A* 337, pp. 615.

Gordon, C.M. and Peters, C.W. (1988). Instrumental assay of kerogen in shale using fast neutrons, *Nucl. Geophysics* 2, pp. 123.

Gozani, T. (1988). Advances in bulk elemental analysis using neutron interactions. *IAEA-TECDOC-464*, pp. 123.

Hevesey, G. and Levi, H. (1936). *Math-Fys.*, 14, pp. 3. Institute Theoretical Physics University of Copenhagen.

Hudson, C.G., Alford, W.L. and Ghorai, S.K. (1978). Neutron excitation functions for ^{45}SC, ^{93}Nb, and ^{58}Ni in the energy range 13-19 MeV. *J. Ann. of Nucl. Energy* 5, pp. 589.

IAEA, (1993). Handbook on Nuclear Data for Borehole Logging and Mineral Analysis *TECHNICAL REPORT SERIES* No. 357 Vienna.

IRDF-90 (1990). International Radiation Dosimetry Files. Assembled by Korchrov, N.P. and Mclaughin, P.K. *IAEA-NDS-141*, August, 1990.

Jozsa, M., Mate, Z., Vress, Z. and Zolnai, L. (1988). Calibration of the analyzing magnet of the MGC cyclotron. (An unpublished report at the Institute of Nuclear Research, Debrecen, Hungary).

Knoll, G.F., (1979). *Radiation Detection and Measurements.* John Wiley & Sons, Inc., New York. Inc., New York.

Kornilov, N.V., Baryba, V., Balickij, A.V., Rudenko, A.C., *Daroczy, S., Raics, P. and Nagy, S.* (1985). Cross sections of $^{58}Ni(n,p)$ in the 7-10 MeV neutron energy range. *Atom. Ener.*, 58, pp. 128.

Kormany, Z., Mahunka, I and Valek, A. (1989). Applications and development at the MGC cyclotron. 26-th European Cyclotron Progress Meeting 23 November. Lovain-la-Neuve, Belgium.

Lederer, C.M. and Virginia S.S., (Eds.) (1978) *Table of Isotopes* (seventh edition). John Wiley & Sons Inc., New York.

Levkovskij, V.N., Vinitskaja, G.P., Kovel'skaja, G.E. and Stepanov, V.M. (1969). Cross sections of reactions (n,p) and (n.α) at 14.8 MeV neutron energy. *J. YF.* 10, pp. 44.

Mannhart, W. (1987) The neutron spectrum of spontaneous fission of californium-252. *In:* Handbook on Nuclear Activation Data. IAEA TECHNICAL REPORT SERIES 273, pp. 163.

Marion, J.B. (1966). Accelerator calibration energies, *Rev. Mod. Phys.* 38, pp. 660.

Marion, J.B. and Fowler,(Eds.) J.L. (1960). *Fast Neutron Physics Part I.* John Wiley & Sons New York.

McLane, V.F., Dunford, C.L. and Rose, P. (1988). Neutron Cross Sections VOL. 2 Academic Press, New York.

Meadows, J.W. and Whalen, J.F. (1963). $Ni^{58}(n,p)Co^{58m,g}$ cross section and isomer ratio from 1.04 to 2.67 MeV. *Phys. Rev.* 130, pp. 2022.

Muir D.W.(Ed.), (1979) WRENDA 79/80, INDC(SEC)-73/URSF, IAEA, Vienna.

Okumura, S. (1967) Isomer pair cross sections by 13.4-15.0 MeV neutrons. *Nucl. Phys. A* 93, 74. *Phys. A* 93, pp. 74.

Olah, L., (1994) Neutron spectrometer with NE 213 organic scintillator (unpublished report at the Institute of Experimental Physics, Debrecen, Hungary).

Pavlik, A., Winkler, G., and Uhl, M., (1985). Neutron induced reactions on ^{58}Ni, *Nucl. Sci. and Engr.* 90, pp. 186.

Peiguo, F., Zhao, W., Teng Dan, and Lu Hanlin (1985). Measurements of cross sections for some reactions induced by 8.62 MeV neutrons, *Chinese J. Nucl. Phys.* 7, pp. 242.

Piksakin V., (Ed.), (1983) WRENDA 83/84, INDC(SEC)-88/URSF, IAEA, Vienna.

Raics, P., Paszti, F., Daroczy, S. and Nagy, S. (1981). Measurement of the cross sections for $^{58}Ni(n,2n)$, $^{58}Ni(n,p)$, $^{58}Ni(n,d)$, and $^{58}Y(n,2n)$ reactions around 14 MeV. *ATOMKI kozl.* 23, pp. 45.

Rakovic, M., (1970). *Activation Analysis.* ILIFFE Books Ltd., London.

Reus, U., and Westmeier, W. (1983). *Nuclear Data Tables.* Academic Press, New York.

Ribansky, I., Kristiak, J., Stoeva, L. and Pateleev, C. (1985). Neutron activation cross section for Ni isotopes at 14.8 MeV. *REPORT INDC(CSR)-7.*

Senfle, F.E., Moore, H.D., Leep, D.B., El-Kady, A. and Duffey, D. (1971). Analytical sensitivities and energies of thermal neutron capture gamma rays II. *Nucl. Instr. and Meth.* 93 , pp. 425.

Smith, D.L. and Meadows, J.W. (1973). Measurement of $^{58}Ni(n,p)^{58}Co$ reaction cross sections for E_n = 0.44-5.87 MeV using activation methods. *ANL-7989, Argonne III.*

Storn, E., and Israel, H.I. (1970). *Nuclear Data Tables, Sect. A.*, Vol. 7, pp. 565.

Sudar, S. (1989) A solution for the neutron spectrum unfolding problem without using input spectrum, *INDC(HUN)-026/L IAEA,* Vienna.

Sudar, S., Csikai, J., Qaim, S.M. and Stocklin, G. (1992). Neutron cross sections for $^{60}Ni(n,p)^{60m}Co$, $^{60}Ni(n,p)^{60m+g}Co$ and $^{58}Ni(n,p)^{58m}Co$ reactions in the 5-12 MeV energy range.
In: Qaim S.M. (Ed.), *Nuclear Data for Science and Technology.* (Springer-Verlag, Berlin) pp. 291.
Proceedings of an International Conference held in Julich, Germany.

Sudar, S. (1994) Statistical model calculations of $^{58}Ni(n,p)$ reaction from 0 to 15 MeV (Report, Institute of Experimental Physics, Kossuth University, Debrecen, Hungary).

Szegedi, S., and Dezso, Z., (1982). Determination of chlorine content in chlorinated polyethylene using neutron physical method. *Radiochem. Radioanal. Lett.* 52, pp. 343.

Szegedi, S., Varadi, M., Buczko, Cs.M., Varnagy, M and Sztaricskai, T. (1990). Determination of boron in glass by neutron transmission method. *J. Radioanal. Nucl. Chem. Lett.* 146, pp. 177.

Viennot, M., Haddo, A.A., Chiadli, A. and Paic, G (1991). Cross section measurements for some reactions of (n,p) and (n,np+pn+d) reactions for some Ti, Cr, Co, Ni and Zn isotopes around 14 MeV. *J. Nucl. Sci. and Engr.* 108, pp. 289.

Vonach, H., Wagner, M. and Haight, R.C. (1990). NEANDC Specialists' Meeting on Neutron Activation Cross sections for Fission and Fusion Applications. Argonne 13-15 Sept. 1989. *NEANDC-259 U*, pp. 165.

Vourvopolous, G.(1993). Multi-parameter on-line coal bulk analysis. *Journal of Coal Quality* 12, pp. 96.

Vourvopolous, G.and Womble, P.C. (1989). On-line sulphur determination in coal with prompt gamma neutron activation. *Nucl. Instr. and Meth. B* 36, pp. 200.

Vourvopolous, G.and Shultz, F.J. (1993). A pulsed fast-thermal neutron system for the determination of hidden explosives. *Nucl. Instr. and Meth. B* 79, pp. 585.

Vourvopolous, G. and Humphrey, D.L. (1994). Multi-parameter on-line coal bulk analysis. In: Proceedings of the Tenth Annual Coal Preparation, Utilization and Environmental Control Contractors Conference 13-21 July.Pittsburgh, Pennsylvania, 1, 41.

Watterson, J.I.W. (1993). Optimization of geometrical and spectral factors for the determination of carbon in coal by neutron induced prompt gamma-ray analysis. *Nucl. Geophysics* 7, pp. 87.

Weisskopf, V.F. and Erwing, D.H. (1940). On the yield of nuclear reactions with heavy elements. *Phys. Rev.* 57, pp. 472.

Zelenetsky, A.V. (1994). Statistical model calculations of $^{58}Ni(n,p)$, $^{63}Cu(n,\alpha)$ and $^{65}Cu(n,\alpha)$ reactions from the thresholds to 20 MeV. (private communication with the Institute of Experimental Physics, Debrecen).

Zhao, W, Hanlin, Y., Weixiang, Y., and Xialin, Y., (1989). Compilation of Measurements and Evaluations of Nuclear Activation Cross sections for Nuclear Data Applications. *IAEA, INDC(CPR)-16.*

APPENDIX

THE CONTRIBUTION OF METASTABLE STATE TO GROUND STATE

The production rate of ground state atoms in which an isomeric state radionuclide is also produced is given as:

$$\frac{dN_g(t)}{dt} = n\,\sigma^g\phi - \lambda_g N_g(t) + \lambda_g N_m(t) \qquad (1)$$

where N_g is the number of ground state atoms produced duringirradiation,

n is the number of atoms in the sample,

σ^g is the activation cross section for the production of ground state atoms,

ϕ is the neutron flux reaching the sample,

λ_g is the decay constant of the ground state,

and N_m is the number of metastable atoms produced during irradiation.

The rate of production of metastable state is given as;

$$\frac{dN_m(t)}{dt} = n\,\sigma^m\,\phi - \lambda_m N_m(t) \qquad (2)$$

Given that the number of metastable state before irradiation is zero,

i.e. $N_m(0) = 0$ at $t = 0$, then the solution of equation 2 is:-

$$N_m(t) = \frac{n\,\sigma^m\phi}{\lambda_m}(1 - e^{-\lambda_m t}) \qquad (3)$$

At $t = t_i$ equation (3) becomes

$$N_m(t_i) = \frac{n\,\sigma^m\phi}{\lambda_m}(1 - e^{-\lambda_m t}) \qquad (4)$$

Equation 4 gives the number of metastable state atoms produced at the end of irradiation. Substituting for $N_m(t)$ in equation (1), then it becomes;

$$\frac{dN_g(t)}{dt} = n\,\sigma^g\,\phi - \lambda_g\,N_g(t) + n\,\sigma^m\,\phi\,(1 - e^{-\lambda_m t}) \qquad (5)$$

If equation 5 is re-arranged, it becomes;

$$\frac{dN_g(t)}{dt} + \lambda_g\,N_g(t) = n\,\sigma^g\,\phi + n\,\sigma^m\,\phi\,(1 - e^{-\lambda_m t}) \qquad (6)$$

Or,

$$\frac{d}{dt}\left[N_g(t)\,e^{\lambda_g t}\right] = [n\,\sigma^g\phi + n\,\sigma^m\phi\,(1 - e^{-\lambda_m t})]e^{-\lambda_g t}$$

$$= n\,\phi\,(\sigma^g + \sigma^m)\,e^{\lambda_g t} - n\,\phi\,\sigma^m\,e^{(\lambda_g - \lambda_m)t} \qquad (7)$$

The integration of equation 7 gives;

$$\rightarrow \left[N_g(t)\, e^{\lambda_g t} \right]_0^{t_{irr}} = \int_0^{t_{irr}} n(\sigma^g + \sigma^m)\, \phi\, e^{\lambda_g t}\, dt - \int_0^{t_{irr}} n\, \sigma^m \phi\, e^{(\lambda_g - \lambda_m)t}\, dt$$

$$= \frac{n\,\phi\,(\sigma^g + \sigma^m)}{\lambda_g} e^{\lambda_g t} \Big|_0^t - \frac{n\,\phi\,\sigma^m}{\lambda_g - \lambda_m} e^{(\lambda_g - \lambda_m)t} \Big|_0^{t_i}$$

$$= \frac{n(\sigma^g + \sigma^m)\phi}{\lambda_g}(e^{\lambda_g t_i} - 1) + \frac{n\sigma^m\phi}{\lambda_g - \lambda_m}\left[1 - e^{(\lambda_g - \lambda_m)t_i}\right] \qquad (8)$$

At the beginning of irradiation $t = 0$, $N_g(0) = 0$; and at the end of irradiation $t = t_i, N_g(t) = N_g(t_i)$, hence equation (8) becomes;

$$N_g(t_{irr}) = \frac{n(\sigma^g + \sigma^m)\,\phi}{\lambda_g}(1 - e^{-\lambda_g t_i} + \frac{n\sigma^m\phi}{\lambda_g - \lambda_m}(e^{-\lambda_g t_i} - e^{-\lambda_m t_i}) \qquad (9)$$

Therefore the number of ground state atoms produced during irradiation that lasted for a given time (t_i) including the contributions of the metastable state atoms is given by equation 9.

The rate of decay rate of ground state after irradiation is:

$$\frac{dN_g(t)}{dt} = -\lambda_g N_g(t) + \lambda_m N_m(t) \qquad (10)$$

Similarly the rate of decay of metastable state to the ground state can be written as:

$$\frac{dN_m(t)}{dt} = -\lambda_m N_m(t) \qquad (11)$$

The solution of equation 11 is:

$$N_m(t) = N_m(t_i)\ e^{-\lambda_m t} \qquad (12)$$

where $N_m(t_i)$ is the number of metastable state nuclei at the end of irradiation. By substituting for $N_m(t)$ in equation 10 using the expression given in equation 12, we obtain;

$$\frac{dN_g(t)}{dt} = -\lambda_g N_g(t) + \lambda_m N_m(t_i)\ e^{-\lambda_m t} \qquad (13)$$

Integrating the above equation and taking the limits of integration from $t = t_i$ to $t = t_c$ (*i.e.* the cooling time after irradiation) leads to:

$$N_g(t).e^{\lambda_g.t}\Big|_{t_i}^{t_c} = \int_0^{t_c} \lambda_m N_m(t_i)\, e^{(\lambda_g - \lambda_m)t}\, dt$$

$$= \frac{\lambda_m}{\lambda_g - \lambda_m} N_m(t_i)\, e^{(\lambda_g - \lambda_m)t}\Big|_{t_i}^{t_c} \qquad (14)$$

i.e.,

$$N_g(t_c)\, e^{\lambda_g t_c} - N_g(t_i) = \frac{\lambda_m}{\lambda_g - \lambda_m} N_m(t_i) \left[e^{(\lambda_g - \lambda_m)t_c} - 1 \right]$$

Or

$$N_g(t_c) = N_g(t_i)\, e^{-\lambda_g t_c} + \frac{\lambda_m}{\lambda_g - \lambda_m} N_m(t_i) \left[e^{-\lambda_m t_c} - e^{-\lambda_g t_c} \right] \qquad (15)$$

$N_g(t_i)$ is the number of ground state nuclei at the end of irradiation as expressed in equation (9). Similarly $N_m(t_i)$ expressed in equation (4). Therefore, equation (15) gives the number of ground state atoms and the contribution of the decay of metastable state to the ground state at time $t = t_c$ (*i.e.* the cooling time after irradiation). If we substitute for $N_g(t_i)$ and $N_m(t_i)$ in equation (15), then the equation after simplification becomes;

$$N_g(t_c) = n\phi \{ [\frac{(\sigma^g - \sigma^m)}{\lambda_g} - \frac{\sigma^m}{\lambda_g - \lambda_m}](1 - e^{-\lambda_g t_i}) e^{-\lambda_g t_c}$$

$$- \frac{\sigma^{m}}{\lambda_m - \lambda_g} (1 - e^{-\lambda_m t_i}) e^{-\lambda_m t_c} \} \qquad (16)$$

This equation expresses the number of ground state atoms obtained at a certain time ($t = t_c$) after irradiation including the number of metastable state atoms decaying to the ground state.